UNIVERSITAT DE BARCELONA

Targeting non-canonical p38 MAPK signalling: discovery and characterization of novel allosteric p38α inhibitors

Lorena González Velasco

UNIVERSITAT DE BARCELONA

Facultat de Farmàcia i Ciències de l'Alimentació

Programa de Doctorado en Biomedicina

Targeting non-canonical p38 MAPK signalling: discovery and characterization of novel allosteric p38α inhibitors

Memoria presentada por Lorena González Velasco para optar al título de doctor por la Universitat de Barcelona

Esta tesis se ha realizado en el Institut de Recerca Biomèdica de Barcelona (IRB Barcelona)

DIRECTOR	DOCTORANDA	TUTORA
Dr. Angel Rodríguez Nebreda	Lorena González Velasco	Dra. Neus Agell Jané

A mis padres,

Yo quiero construir. Pero no soy sino una parte insignificante pero importante de un todo del que todavía no tengo conciencia

Frida Kahlo

Todo tiene su final. Y aunque parecía un sueño hace unos años, este es el desenlace de la intensa (y no menos apasionante) historia que he tenido el honor de poder contar.

Por todo ello, me gustaría agradecer a todas y cada una de las personas que me han acompañado durante este viaje. Quien bien me conoce sabe que las palabras me sobran. Aun así, intentaré ser breve.

En primer lugar, me gustaría dar las gracias a Angel, por tenderme la mano, confiar en mí y dejarme volar. No soy la misma que llamó la primera vez a la puerta de tu despacho. Me has dado la oportunidad de poder vivir la ciencia en muchas de sus facetas y aprender del trasluz de todos sus vértices. Que la importancia reside en el camino, en razonar cada paso que damos, y entender aquellos que, si bien no son en falso y no salen como esperábamos, nos hacen de guía cuando creemos haber perdido el norte. Gracias por haber conseguido que aquel proyecto de científica motivada e ingenua sea hoy una persona segura de sí misma, capaz de canalizar su energía y preparada para enfrentarse a cualquier reto que se le ponga por delante.

A los miembros del comité de la tesis, Neus Agell, Roger Gomis y Raúl Méndez, gracias por el enriquecedor feedback y el apoyo en cada reunión a lo largo del proyecto.

A todo el Nebrda's Lab, gracias por cada uno de los días desde septiembre del 2015. Por la gente que está y la que se fue. A todos, de corazón, os estaré eternamente agradecida. Gracias por escucharme (y oírme desde lejos) cada día y aguantar mi gran repertorio de tonterías varias (incluyendo bailes y chistes malos), mis momentos de exaltación y cuquismo, los episodios de culturización sin venir a cuento y cuando no tocan, atender (o intentarlo) en mis lab meetings extensos e intensos, y un largo etcétera. Ana, gracias por guiarme en mis primeros pasos, por las críticas constructivas y las charlas infinitas en nuestro pequeño confesionario (también llamado animalario) vestidas de astronautas. Bego, tu pequeña tinki-compañera de escritorio-bench se ha hecho mayor, gracias por ayudarme a crecer haciéndome pensar de manera ordenada y racional, por compartir la pasión por la enseñanza y la comunicación científica, por la marcha reggaetonera para hacer experimentos de buena mañana, y por los cotilleos y confesiones varias. Laura y Núria, el dúo dinámico, gracias por las risas en el pasillo entre discusiones científicas-canciones-tertulias, por el apoyo moral tras cada drama-experimento y las celebraciones de los buenos resultados. Clara (la meva petiteta) y Mónica, si es que sois de lo más cuqui que he conocido, gracias por retroalimentarme personal y científicamente, y por endulzar el lab cada día.

Eli, gracias por ser la energía y organizadora de eventos del laboratorio, por mantener la alegría de nuestro pasillo y el apoyo diario. Raquel, gracias por la orientación científica y las conversaciones vitales en el tramo cultivos-pasillo. Marga y Fani, gracias por empujar este proyecto y ser la sinergia que necesitaba en algunos momentos de desesperación. Nevenka and Dan, thanks for your daily enthusiasm and all your feedback.

A Nostrum, especialmente a Robert, Lucía, Dani y Chiara. También a Modesto e Isabelle. Gracias por enseñarme el increíble mundo de la bioinformática, las simulaciones y el drug discovery, por el pensamiento crítico y a la vez abstracto en nuestras tantas reuniones, por el entusiasmo en cada hipótesis y el ansia de ver los resultados de cada experimento.

A mi vecina, María. Gracias por acogerme en tu agradable despacho floreado y lleno de libros, por guiarme en el maravilloso mundo de la biología estructural, por enseñarme a ver más allá de hélices y láminas bonitas, y por las charlas en las que entre tanta ciencia hemos intentado arreglar el mundo. Y también a todo tu grupo, en especial a Blazej, Pau, Lídia, Eric y Carles, gracias por toda vuestra ayuda, por compartir vuestro conocimiento conmigo y darme infinitos consejos.

A Joan, gracias acogerme en "la casa de los cristales", por hacerme feliz viendo como crecían (y desaparecían) mis pequeños, y por enseñarme con mucha paciencia a entender la razón de ser de las proteínas.

A la gente del IRB, gracias por haber hecho de este lugar la casa en la he vivido unos de los años más felices de mi vida. Al resto de compañeros de doctorado, gracias por hacer inigualable el día a día y por dejar el listón muy alto en las Cool-offs, Welcome Parties, Fiestas de Navidad y Esquiadas. Especialmente, a los Chiquitos Personajes, Marina, Sara, Isa, Enric, Joel, Edu, Adri, gracias por llenar de risas todas las salidas, cumpleaños, terraceos y cenas. Marina, gracias cuca, por la ser la mejor compañera de té y chocolate de esta etapa (aunque a veces parecíamos del mismo lab), por todas las discusiones científicas, por el ENABLE, por acogerme en tu casa tantas noches, por las tertulias infinitas y los audios al llegar a casa, y por reírnos y llorar a la par de los resultados que teníamos. Leyre, (pero bueno!) gracias por ser la felicidad personificada, por acogerme en tu casa cada miércoles para ir el jueves a inglés con Chris, por las cenitas y las sesiones de netflix fallidas, por abrirme los ojos cuando me veías algo perdida, por decidir apuntarnos juntas a la media maratón, por todas las videollamadas durante el confinamiento y entrenar a la vez, y sobre todo, por animarme a darlo todo (y petarlo) por la vida (Vamos Lore sal a bailar, que tú lo haces fenomenal...). Cris Figueras, Raquel, Noelia, Cris Fuster, Helena, Ricardo, Denise, Pablo, etc, gracias

por todas las anécdotas compartidas y por vuestras ganas sin fin.

A la Tech Transfer Office, en especial a Tiago e Israel. Gracias por sacarme de mi (primera) zona de confort y hacer que conociera una segunda, por vuestros consejos y confianza, y motivarme a dar lo mejor de mí. Al Departamento de Comunicación, especialmente a Muriel, gracias por contar conmigo siempre y por dejarme crecer como divulgadora científica (y animadora).

Además, me gustaría agradecer a todas las personas que habéis formado parte en algún momento u otro de este camino, por nutrir mi pasión por la biología celular y molecular desde que empecé Biomedicina hasta que decidí que quería hacer, sin lugar a duda, el doctorado. Gracias a las chicas del laboratorio de Ginecología Oncológica del Vall d'Hebrón durante las prácticas de cada verano, a Carlos del Departamento de Genética de la UB por dejarme ser su ayudante, y al laboratorio de Bart Vanhaesebroeck en UCL.

A mis mejores amigos, Noelia, Ana, Homs, Laura, Jordi, Irene, Vicky, Elena, Ribbi y Ania, gracias por creer en mi y demostrarme que sería posible. A vosotros también Berta y Miguel, gracias por aparecer en el mejor momento y traerme el baile de vuelta.

A ti también Gerard, gracias por hacerme feliz y acompañarme en el último sprint.

Finalmente, agradecer a toda mi familia por su apoyo incondicional y por confiar siempre en mi. Mama, papa y Javier, gracias por ser la luz del faro y el timón del barco, por acompañarme en todos y cada uno de los momentos vividos hasta el día de hoy, por nunca soltar mi mano en las situaciones difíciles, por celebrar los logros y acurrucarme cuando necesitaba el calor de un buen abrazo en casa. Gracias infinitas por dejarme ser yo misma, en toda mi esencia.

Yaya, sé que nunca has dejado de creer en mí, y allí donde estés quiero que sepas que si estoy aquí es también gracias a ti.

CONTENTS

ABBREVIATIONS

A

Ala/A, Alanine
ADP, Adenosine diphosphate
AMPK, 5'-AMP-activated protein kinase
APAF, Apoptosis protease-activating factor-1
APS, Ammonium persulfate
Arg/R, Arginine
ASK1, Apoptosis signal-regulating kinase 1
Asn/N, Asparagine
Asp/D, Aspartic acid
ATF2, Activating transcription factor 2
ATP, Adenosine triphosphate

B

Bax, Bcl-2 Associated X protein
Bcl-2, B-cell lymphoma 2
BMRB, Biological magnetic resonance bank
BRET, Bioluminescence resonance energy transfer
BSA, Bovine Serum Albumin

C

CBFHH, Calcium and bicarbonate free Hanks HEPES buffer
cDNA, Complementary DNA
CREB, cAMP response element-binding protein
Cys/C, Cysteine

D

2D, Two-dimensional
DAPI, 4, 6-diamidino-2-phenylindole
DMA, Dimethylacetamide
DMEM, Dulbecco's modified Eagle´s medium
DMSO, Dimethyl sulfoxide
DNA, Deoxyribonucleic acid
DNAse, Deoxyribonuclease
DPBS, Dulbecco's phosphate buffered saline

DTT, Dithiothreitol
DUSP, Dual specificity phosphatase

E
EDTA, Ethylenediamine tetraacetic acid
EGTA, Ethylene glycol tetraacetic acid

F
FACS, Fluorescence-activated cell sorting
FBS, Fetal bovine serum
FITC, Fluorescein
FLPC, Fast protein liquid chromatography
Fw, Forward

G
GFP, Green fluorescent protein
Gln/Q, Glutamine
Glu/E, Glutamic acid
Gly/G, Glycine
GPCRs, G protein-coupled receptors
GRK2, G-protein-coupled receptor kinase 2
GST, Glutathione S-transferase

H
HBSS, Hanks' Balanced Salt Solution
HEPES, 4-(2-hydroxyethyl)-1-piperazineethanesulfonic acid
HIF1, Hypoxia-inducible factor 1
His/H, Histidine
HPLC, High performance liquid chromatography
Hsp27, Heat shock protein 27

I
IL-6, Interleukin-6
Ile/I, Isoleucine
IRE1a, Serine/threonine-protein kinase/endoribonuclease IRE1a

IPTG, Isopropyl β-D-1-thiogalactopyranoside
ITC, Isothermal titration calorimetry

J

JNK, c-Jun N-terminal kinase

K

KA, Kinase assay
KSR2, Kinase Suppressor of Ras 2

L

LB, Luria broth base
Leu/L, Leucine
LPS, Lipopolysaccharide
Lys/K, Lysine

M

MAPK, Mitogen- activated protein kinase
MAPKAPK2, MAPK-activated protein kinase 2
MAPKK, Mitogen- activated protein kinase kinase
MAPKKK, Mitogen- activated protein kinase kinase kinase
MBP, Myelin basic protein
MEKK, MAPK/ERK kinase kinase
Met/M, Metionine
MK,2 MAPKAPK2
MKI, MAPK insert
mRNA, Messenger RNA
MPTP, Mitochondrial permeability transition pore
mPT, Mitochondrial permeability transition.
MS, Mass spectrometry
MSK, Mitogen and stress activated protein kinase
MTT, 3-(4,5-dimethylthiazol-2-yl)-2,5-diphenyl tetrazolium bromide

N

NC, Non-canonical

NCX, Sodium-calcium exchanger
NLK, Nemo-like kinase
NRVM, Neonatal ventricular myocyte

O
O/N, Overnight

P
p38α, Mitogen- activated protein kinase 14
PAR1, Protease-activated receptor 1
PBS, Phosphate buffer solution
PDB, Protein data base
PDK1, 3-phosphoinositide-dependent protein kinase 1
PEG, Polyethylene glycol
PFA, Paraformaldehyde
PG, Propylene glycol
Phe/F, Phenylalanine
PIF, PDK1 interacting fragment
PK, Pharmacokinetic
PKC, Protein kinase C
PLA, Proximity ligation assay
PLK1, Polo-like kinase 1
PMA, Phorbol 12-myristate 13-acetate
PMSF, Phenylmethylsulfonyl fluoride
PP2A, Protein phosphatase 2A
PPI, Protein-protein interactions
Pro/P, Proline
PTM, Post translational modification

Q
qRT-PCR, Quantitative real time-Polymerase chain reaction

R
Reg3, Regenerating islet-derived protein 3
RMSD, Root Mean Square Deviation

RNA, Ribonucleic acid
Rpm, Revolutions per minute
ROS, Reactive oxygen species
RT, Room temperature
Rv, Reverse

S

SDS, Sodium dodecyl sulfate
SD, Standard deviation
Ser/S, Serine
SPR, Surface Plasmon Resonance
siRNA, small interfering RNA

T

TAB1, TAK1-binding protein1
TAK1, Transforming growth factor b-activated kinase
TCR, T-cell receptor
TCEP, Tris (2-carboxyethyl) phosphine hydrochloride
TE, Target engagement
TEMED, Tetramethylethylenediamine
TGFβ, Transforming growth factor b
Thr/T, Threonine
TMRE, Tetramethylrhodamine ethyl ester
TnI, Troponin I
TNFα, Tumoral necrosis factor alpha
TROSY, Transverse Relaxation Optimized Spectroscopy
Trp/W, Tryptophan
TSA, Thermal shift assay
Tyr/Y, Tyrosine

U

UCP1, Uncoupling protein 1
UV, Ultra

V

Val/V, Valine

VDAC1, Voltage-dependent anion-selective channel protein 1

Z

ZAP70, z-chain-associated protein kinase 70 kDa

SUMMARY / RESUMEN

Non-canonical activation of p38α MAPK has been associated to cardiomyocyte death in several cardiovascular pathologies, such as myocardial ischaemia-reperfusion injury. Unfortunately, current p38α inhibitors are mainly ATP-competitors, which have not progressed in clinical trials. Efforts to discover novel allosteric p38α inhibitors are crucial to overcome potential side effects that undermine their therapeutic efficacy. By running an *in silico* small molecule drug discovery program to target the non-canonical site on p38α, we have identified several compounds, named NC-p38i, which inhibit both TAB1-induced and spontaneous p38α autophosphorylation *in vitro*. Additionally, NC-p38i do not inhibit canonical MAP2K-dependent p38α activation but slightly impair its ability to phosphorylate substrates. A combination of biophysical and structural studies has allowed us to characterize their mechanism of action. NC-p38i do not interfere with the binding of TAB1 to p38α *in vitro* but modulate the ATP-binding site and the prone-to-autophosphorylate conformation of the kinase. Nuclear magnetic resonance and X-ray crystallography data suggest that NC-p38i probably bind to several sites on p38α, including the active site and the N-terminal domain, which may induce structural rearrangements that reduce its autoactivation capacity. Cell based assays show that NC-p38i decrease ischaemia-reperfusion-induced cardiomyocyte death both under prophylactic and therapeutic conditions. Moreover, these compounds ameliorate doxorubicin-induced cardiac toxicity in human iPSC-derived cardiomyocytes and zebrafish models. Importantly, NC-p38i are quite specific at inhibiting p38α but not a number of other protein kinases, and possess good drug-like properties, including weak cardiac hERG K^+ channel inhibition and low cytotoxic effects. Together, our data identify NC-p38i as novel allosteric p38α inhibitors with promising cardioprotective effects, which may serve as a good starting point to develop clinical candidates for treating non-canonical p38α signalling associated diseases.

La activación no canónica de p38α MAPK se ha asociado con la muerte de los cardiomiocitos en varias patologías cardiovasculares, como el daño miocárdico producido por isquemia-reperfusión. Desafortunadamente, los inhibidores de p38α actuales son principalmente competidores de ATP, y no han progresado en los ensayos clínicos. Por tanto, resulta crucial descubrir nuevos inhibidores alostéricos de p38α para evitar los potenciales efectos secundarios que reducen su eficacia terapéutica. En este trabajo, hemos desarrollado un programa *in silico* de descubrimiento de fármacos para diseñar compuestos que se puedan unir al sitio no canónico en p38α. Hemos identificado varias moléculas, denominadas NC-p38i, que inhiben la autofosforilación de p38α tanto inducida por TAB1 como espontánea *in vitro*. Además, los NC-p38i no inhiben la activación canónica de p38α dependiente de MAP2K, aunque afectan ligeramente la capacidad de p38α para fosforilar sustratos. La combinación de estudios biofísicos y estructurales nos ha permitido caracterizar su mecanismo de acción. Los NC-p38i no interfieren con la unión de TAB1 a p38α *in vitro*, pero alteran el sitio de unión del ATP y la conformación propensa a la autofosforilación de la quinasa. Los datos de resonancia magnética nuclear y de cristalografía de rayos X sugieren que los NC-p38i podrían unirse a varios sitios en p38α, incluido el sitio activo y el dominio N-terminal, lo que puede inducir alteraciones estructurales que reducen su capacidad de autoactivación. Ensayos celulares muestran que los NC-p38i reducen la muerte de los cardiomiocitos inducida por isquemia-reperfusión tanto en condiciones preventivas como terapéuticas. Además, estas moléculas mejoran la toxicidad cardiaca inducida por doxorrubicina tanto en cardiomiocitos humanos derivados de iPSCs como en pez cebra. Cabe destacar que los NC-p38i inhiben principalmente a p38α pero no a otras proteína-quinasas, y que poseen buenas propiedades farmacológicas, incluyendo una inhibición débil del canal hERG K^+ cardiaco y una citotoxicidad reducida. En conjunto, nuestros datos caracterizan a los NC-p38i como nuevos inhibidores alostéricos de p38α con efectos cardioprotectores prometedores, y que pueden servir como punto de partida para desarrollar candidatos clínicos utilizables en el tratamiento de enfermedades asociadas a la señalización no canónica de p38α.

INTRODUCTION

1. Cellular signalling by protein kinases

Cells are constantly dealing with signals from the extracellular environment. For example, cells respond to the limiting availability of nutrients and oxygen or to the exposure to toxic compounds. This means that they must respond efficiently to environmental changes in order to prevent cellular damage. To do that, cells have developed several signalling pathways that allow them to receive and interpret different stimuli in order to elaborate the appropriate responses (Berridge, 2014).

Proteins play a key role in these pathways as they regulate essential processes such as catalysis, transport and structural integrity. The human proteome is approximately three orders of magnitude more complex than the coding genome, mainly due to alternative splicing of mRNA and post-translational modifications (PTMs). A major class of PTM is phosphorylation, which is regulated by enzymes known as protein kinases that are essential signal transmitters in eukaryotic cells (Taylor and Kornev, 2011; Walsh et al., 2005).

1.1. Allosteric regulation of protein kinases

Proteins contain different sites where ligands and other proteins can bind. The catalytic site of an enzymatic protein is known as the orthosteric site. In protein kinases, this site corresponds to the pocket where ATP binds. Conversely, allosteric sites correspond to binding regions elsewhere in the protein surface that can regulate the protein activity (He et al., 2019; Nussinov and Tsai, 2012).

Allosteric regulation is defined as the mechanism by which a stimulus induces conformational changes and functional modulation in a protein. Binding with ligands (including other proteins and small molecules), mutations, PTMs and alterations in the environment (such as temperature, pH and ion concentrations), induce proteins to acquire different conformations. For example, phosphorylation induces structural rearrangements that can trigger protein activation (Nussinov et al., 2019).

However, it is difficult to identify allosteric regulatory sites, as some of them exist exclusively in intermediate functional states of proteins. Besides, physical and chemical properties of these sites might differ from those of conserved orthosteric sites. Nevertheless, data from crystallographic, nuclear magnetic resonance (NMR) and computational studies have allowed to predict and discover novel allosteric pockets in protein kinases (Cheng and Jiang, 2019).

The structural changes induced by allosteric mechanisms can be of two types. Some can be propagated linearly from the allosteric to the active site (dominomodel), while others can modify the dynamic profile of residues with no significant conformational changes of the whole protein (violin model) (Kornev and Taylor, 2015). Interestingly, allostery can be bidirectional, meaning that binding of small molecules at the ATP-site can also produce conformational changes at regulatory sites, which in turn influences protein-protein interactions (Leroux and Biondi, 2020).

1.2. Protein kinase structure and activation mechanisms

Protein phosphorylation is a highly regulated and reversible process that consists of the addition of a phosphate group (PO_4) to the hydroxyl (-OH) group of polar amino acids. It was discovered in the late 1950s by Krebs and Fischer through their studies of glycogen phosphorylase and phosphorylase kinase (Krebs and Fischer, 1956; Krebs et al., 1959). Eukaryotic protein kinases have been classified based on the sequence similarity of their catalytic domains (Hanks and Hunter, 1995) and human genome sequencing allowed to identification of 518 protein kinases that correspond to nearly 2% of all human genes (Manning et al., 2002). Based on the nature of the -OH group that they phosphorylate, these enzymes are classified as serine/threonine kinases, tyrosine kinases, tyrosine kinase-like enzymes and histidine kinases (Adam and Hunter, 2018; Roskoski, 2019). Protein phosphatases catalyse the removal of phosphate groups from proteins, thus reversing the action of protein kinases (Chen et al., 2017).

The structure of a typical protein kinases consists of a bi-lobal structure, containing a β-sheet rich N-terminal lobe and an α-helical C-terminal lobe, which are linked by a flexible hinge that forms the ATP-binding site. Both lobes contain functional motifs that enable the catalytic kinase activity (Figure 1) (Taylor et al., 2012). The main functional motifs are:

- The flexible P-loop (also known as G-loop, glycine-rich loop) located in the N-lobe coordinates the binding of the ATP for catalysis.
- The activation segment extends from the DFG-motif in the N-lobe to the APE-motif in the C-lobe and forms the A-loop (activation loop), which contains the phosphorylation sites required for catalytic activation.
- The APE (Ala-Pro-Glu) motif anchors the activation segment to the kinase domain.

- The DFG (Asp-Phe-Gly) motif moves between in and out conformations. The DFG-in position normally translates into the active state of kinases, whereas the DFG-out maintains the protein inactive, as the Phe residue blocks the binding of ATP. The Asp residue binds to a magnesium ion and is required for binding to the three phosphate groups of ATP.

- The P +1 loop mediates the correct position of the residue located one position C-terminal to the phosphorylation site (the P +1 residue) of the substrate.

- The αC-helix and β3-sheet, located in the N-lobe, form together the Glu-Lys bridge that favours the binding of ATP phosphates. Notably, the αC-helix also acquires in (active) and out (inactive) conformations.

- The catalytic loop contains an essential Asp residue required for the phosphotransfer reaction. Protein kinases that are regulated by phosphorylation of their A-loop, it is frequently preceded by an Arg residue (RD-motif).

The process that switches protein kinases from inactive to active states is highly regulated and involves dynamic reorganization of the protein. The phosphorylation of the A-loop triggers the movement of the DFG motif, the rotation of the αC-helix, the formation of the Glu–Lys salt bridge, and the closure of a domain between the two lobes. These structural rearrangements collectively stabilize the active conformation of the protein that catalyses the phosphotransfer reaction of the γ-phosphate in the ATP molecule to the phosphoacceptor site of a protein substrate (Beenstock et al., 2016; Taylor and Kornev, 2011). Besides phosphorylation at the active site, the addition of phosphate groups to sites distinct from the A-loop has been shown to modulate protein kinase activity (Pincus et al., 2018).

The A-loop phosphorylation can be achieved either by another kinase or by autophosphorylation, meaning that protein kinases can be autoactivating enzymes. However, autophosphorylation must overcome some obstacles. First, the A-loop residues are not correctly aligned in the absence of stabilizing elements. Second, kinases have a clear selectivity towards phosphoacceptors, which normally correspond to the Thr (or Tyr in tyrosine kinases) residues in their A-loop, that are not properly orientated towards the catalytic Asp. This means that protein kinases have to adopt a prone-to-autophosphorylate conformation in order to autoactivate (Beenstock et al., 2016).

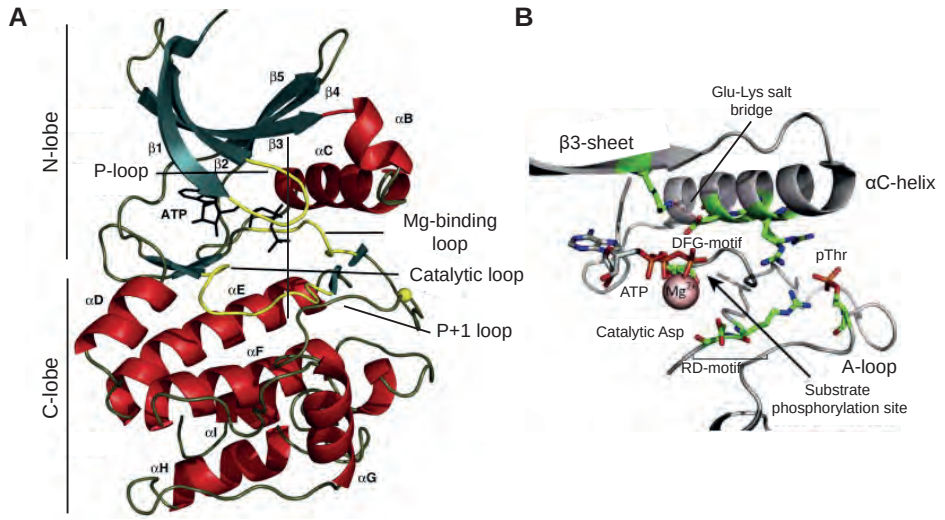

Figure 1. Conserved structure of eukaryotic protein kinases. (**A**) Detailed structure of protein kinases showing an ATP molecule bound between the two lobes. The main structural elements are labelled and indicated in different colours. β-sheets in the N-lobe are coloured in teal, α-helices in the C-lobe are shown in red and catalytically important loops are coloured in yellow. Adapted from (Taylor and Kornev, 2011). (**B**) Detailed structure of the phosphorylated A-loop and its interaction with functional motifs in active p38α MAPK (PDB 3PY3), including the RD-motif in the catalytic loop and the αC-helix, which forms the Glu-Lys salt bridge and aligns the DFG-motif to support catalysis in the substrate phosphorylation site. The important residues are labelled and coloured in green. Phosphate groups from ATP and the phosphorylated threonine (pThr) in the A-loop are coloured in red. Adapted from (Beenstock et al., 2016).

Autophosphorylation mechanisms involve a multistage process that can include either (I) the dimerization of non-active monomers or (II) binding to scaffold proteins that in turn promote a conformational change enabling a prone-to-autophosphorylate state (Figure 2).

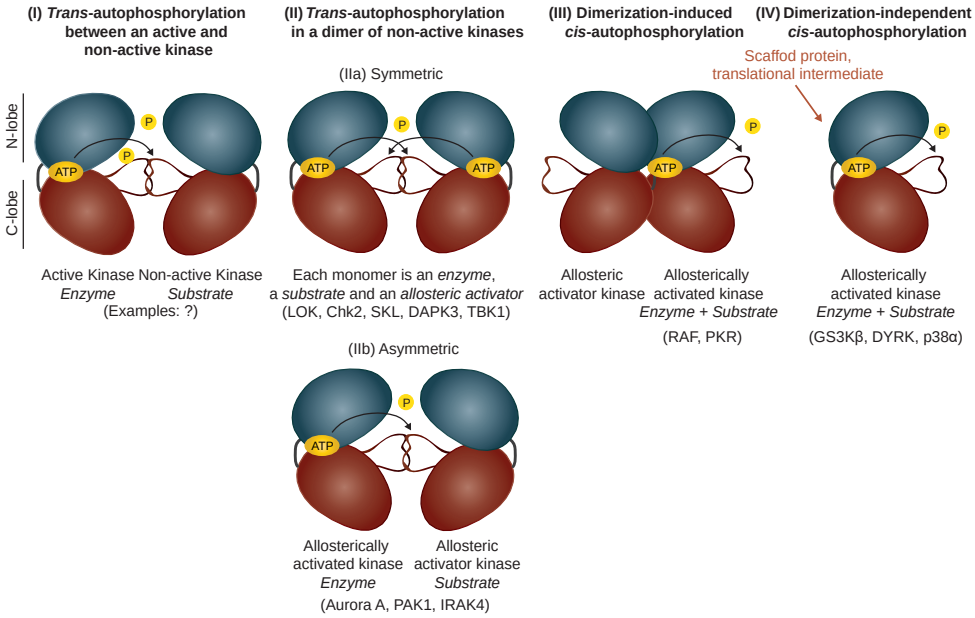

Figure 2. Possible mechanisms for protein kinase autophosphorylation. Protein kinase monomers are represented in a bi-lobal fold and phosphate group (yellow) transfer is shown with arrows. Examples of kinases that follow each mechanism are below the schemes. (**I**) *Trans*-autophosphorylation between a phosphorylated and active kinase and a non-active kinase that functions as a substrate. Theoretical possibility lacking experimental evidence. (**IIa**) Symmetric *trans*-autophosphorylation. Each monomer phosphorylates and activates the other. (**IIb**) Asymmetric trans-autophosphorylation. One monomer serves as an *enzyme* and phosphorylates the other. The *substrate* extends its activation loop into the active site of the *enzyme* monomer, which induces its active conformation. (**III**) Dimerization-induced *cis*-autophosphorylation. Each monomer induces *cis*-autophosphorylation of the other monomer, that works as an allosteric activator, in a mechanism that can either be simultaneous or non-simultaneous. (**IV**) Dimerization-independent *cis*-autophosphorylation. Autophosphorylation occurs in *cis* either by folding into an intermediate structure that is stable and catalytically active during translation (i.e. GSK3b and DYRK1A) or due to an interaction with another protein (i.e. p38α). Adapted from (Beenstock et al., 2016).

1.3. Small-molecule protein kinases inhibitors

Mutation, overexpression and dysregulation of protein kinases play important roles in the pathogenesis of many human diseases including cancer, cardiovascular, inflammatory, autoimmune and nervous disorders. Thus, protein kinases have become one of the most attractive drug targets for the last decades.

There are currently 52 FDA-approved small-molecule inhibitors to target around 20 different protein kinases (Roskoski, 2020). These inhibitors are mainly ATP-competitive enzyme antagonists, which stop entirely the kinase activity. Nevertheless, inhibition of protein kinases by targeting their active site does not ensure high selectivity and effectiveness. Actually, this type of inhibitors usually leads to numerous side effects, as they may non-specifically inhibit several kinases and other ATP-requiring enzymes. As an alternative, structural studies have highlighted that targeting allosteric sites can improve the specificity of protein kinase inhibitors.

Allosteric inhibitors induce conformational changes of specific motifs that modulate the kinase activity, thus increasing the population of inactive enzymes. Hence, this inhibitory mechanism of action is indirect, as they do not directly compete with the ATP binding. Indeed, some of these inhibitors can bind to their target even in presence of ATP. Importantly, allosteric sites are less conserved across families, offering a less disruptive way of kinase inhibition that is expected to produce fewer side effects (Nussinov and Tsai, 2012).

According to this information, protein kinase inhibitors are classified based on the enzyme-bound antagonist complexes (Figure 3) (Roskoski, 2016).

A

	Type I	Type II	Type III	Type IV	Type V	Type IV
Binding region	ATP-pocket	ATP-pocket	Near ATP-pocket allosteric region	Far allosteric region	ATP and substrates sites	ATP-pocket covalent inhibitor
ATP competitive	Yes	Yes	No	No	Variable	No
Enzyme conformation	Active (DGF-in)	Inactive (DFG-out)	Variable	Variable	Variable	Variable
FDA approved	Dasatinib (BCR-ABL)	Sorafenib (VEGFR, RAF1, BRAF, PDGFRB, KIT, RET)	Trametinib (MEK1/2)	Afatinib (EGFR)		

B

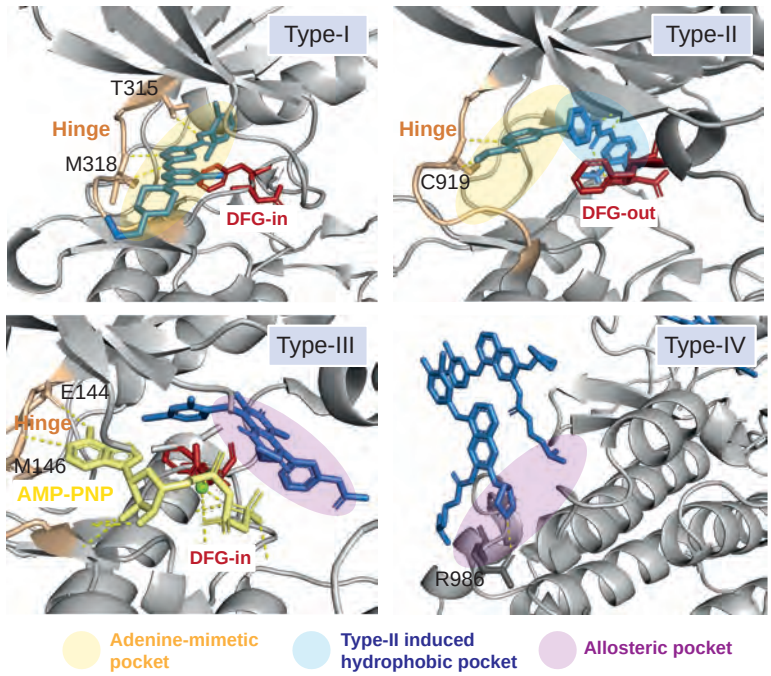

Figure 3. Classification of small-molecule protein kinase inhibitors. (**A**) Classification of protein kinase inhibitors based on the region where they bind, whether they compete with ATP binding site and the protein kinase conformation. Adapted from (Roskoski, 2016). (**B**) Inhibition of different protein kinase inhibitors (blue). Upper left, ATP-competitive type-I inhibitor dasatinib (ABL-dasatinib complex, PDB:2GQG). Upper right, ATP-competitive type-II inhibitor sorafenib (FLK-1-sorafenib complex, PDB:3WZE). Lower left, allosteric type-III inhibitor trametinib (MEK1:AMP-PNP:trametinib complex, PDB:7JUR). Lower right, allosteric type-IV inhibitor afatinib (EGFR:afatinib complex, PDB:4G5J). The main structural elements are labelled, and the binding pockets are indicated by coloured elipsoids.

2. Mitogen-activated protein kinase signalling pathway

The mitogen-activated protein kinases (MAPKs) are serine/threonine kinases that convert extracellular signals into a wide range of cellular responses, including proliferation, differentiation, apoptosis and inflammation. In mammals, there are fourteen MAPKs that are classified into seven different signalling pathways. The conventional extracellular signal-regulated kinase (ERK1/2), ERK5, c-Jun N-terminal kinase (JNK1-3) and p38 (α, β, γ and δ) families (Widmann et al., 1999). Atypical MAPKs include ERK3/4, ERK7 and Nemo-like kinase (NLK) which have different functions and regulation (Coulombe and Meloche, 2007). In general, whereas ERK1/2 are activated by growth factors and mitogens, JNK and p38 MAPKs are strongly activated by stress stimuli, such as osmotic shock and ionizing radiation, and by inflammatory cytokines (Zhang and Liu, 2002).

2.1. MAPK kinase activation and substrate recognition

Canonical MAPK pathways consist of a phosphorylation cascade divided into three sequential signalling modules conserved from yeast to human: a MAPK kinase kinase (MAP3K), a MAPK kinase (MAP2K) and a MAPK. Upon external stimuli, MAP3Ks are activated and phosphorylate MAP2Ks. Once activated, the MAP2K selectively interact with MAPK and phosphorylate the tyrosine and threonine residues in their conserved TXY motif (where X is any amino-acid) on the activation loop (Widmann et al., 1999). Activated MAPKs regulate many functions by phosphorylating target substrates at serine or threonine residues usually followed by a proline (SP/TP sites). These substrates include other kinases such as the MNKs (MAPK-interacting kinases), RSKs (p90 ribosomal S6 kinases), MK2/3 (MAPK-activated protein kinases 2/3), and MK5 (Cargnello and Roux, 2011).

In addition to the consensus phosphorylation sequence, MAPK-substrate selectivity is also regulated by dedicated domains termed docking motifs. There are two described docking motifs in MAPK substrates: D-domain and FXF motif. The D-domain (also known as D site, δ domain, or DEJL domain) consists of a core of basic residues followed by a short linker and a cluster of hydrophobic residues $(Lys/Arg)_2$ -Xaa_{2-6}-ΦA-X-ΦB, where Φ is a hydrophobic residue, such as Leu, Iso or Val). It is found in the N-terminus of MAPK activators (MAP2Ks) and phosphatases (MKPs) (classical D-motif), as well as in the C-terminal domain (reverse D-motif) of several substrates (Tanoue et al., 2000). In contrast, the FXF motif (also called DEF motif, docking site for ERK FXF) consists of two Phe residues separated

by one residue and is found in transcription factors, upstream activators and phosphatases (Figure 4A) (Cargnello and Roux, 2011; Liu et al., 2016).

In MAPKs, two conserved domains are involved in the interaction with the positively charged D-domain. The C-terminal CD (common docking) domain, which is located opposite to the ATP-binding pocket and is comprised of acidic residues (Asp313, Asp315, and Asp316), and the ED (ERK docking) domain that contributes to substrate selectivity in ERK and p38 MAPKs (Figure 4B) (Tanoue and Nishida, 2002).

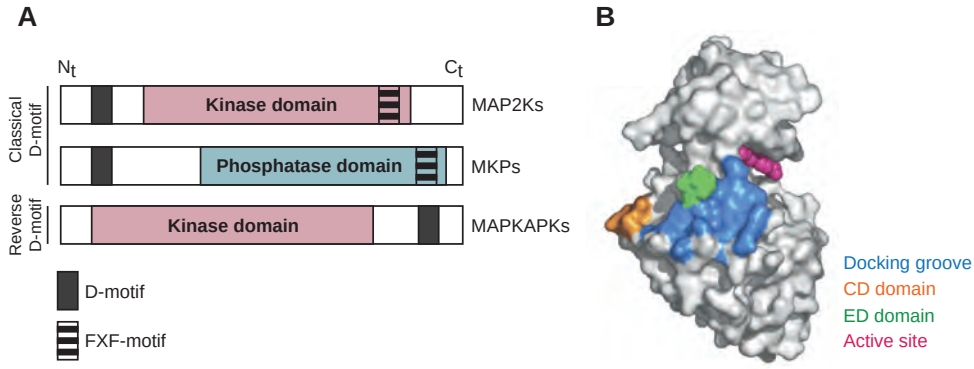

Figure 4. MAPK docking motifs. (**A**) Schematic representation of the D- and the FXF-motifs in activators (MAP2Ks), phosphatases (MKPs) and substrates (MAPKAPKs). Modified from (Tanoue and Nishida, 2002). (**B**) Molecular surface representation of p38α MAPK showing the docking groove (blue) that binds the D domains of activators and substrates (i.e. MKK3b and MEF2A, respectively). The CD site (orange) and ED site (green) that were identified in biochemical studies. The active site of the kinase is bound to the chemical inhibitor SB203580 (red). Modified from (Weston et al., 2002).

3. p38 MAPK signalling pathway

p38 MAPKs are strongly activated in response to different stress stimuli and are crucial in maintaining tissue homeostasis. However, deregulation of this signalling pathway has been associated with inflammatory, cardiovascular, and neurodegenerative diseases as well as with cancer (Canovas and Nebreda, 2021). The p38 MAPK family is comprised by four members p38α, p38β, p38γ and p38δ, which are encoded by different genes and share approximately 60% of their amino acid sequence (Figure 5). Whereas p38α is ubiquitously expressed, expression of the other isoforms is more restricted to specific tissues, for example p38β in the brain, p38γ in skeletal muscle and p38δ in endocrine glands (Cuadrado and Nebreda, 2010).

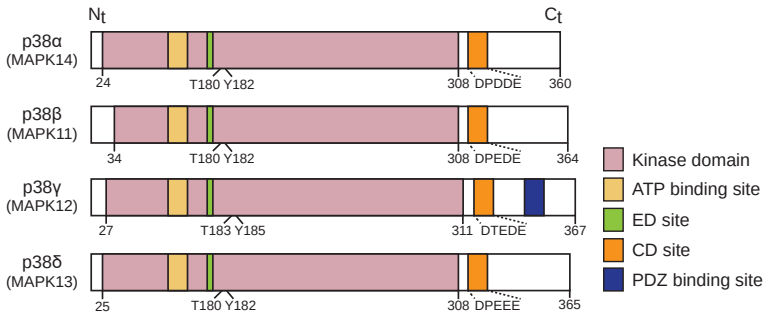

Figure 5. Schematic representation of the four p38 MAPKs. The gene names (in parentheses), amino acid numbers and the different domains are indicated. The kinase domain is 90% identical in amino acid sequence among the four members. The CD and ED domains contribute to docking interactions with substrates and regulators. The ATP binding site and the phosphorylated Thr and Tyr residues of the activation loop are also indicated. p38γ has an additional carboxy-terminal region that binds to PDZ domain-containing proteins (serving as scaffolding proteins for various signalling pathways). Adapted from (Canovas and Nebreda, 2021).

3.1. p38α MAPK structure

p38α is encoded by the MAPK14 gene located on the 6p21.3-p21.2 chromosome region (Coulthard et al., 2009). In addition to the full-length protein, three spliced variants of p38α have been identified: CSBP1, Mxi2 and Exip. CSBP1 differs from p38α only in an internal 25-amino-acid sequence (Lee et al., 1994). Mxi2 contains identical amino acid sequence 1–280 but has a unique C-terminus of 17 amino acids (Casar et al., 2007). Finally, Exip has a unique 53-amino-acid C-terminus and is not phosphorylated by the usual p38 MAPK-activating treatments (Sudo et al., 2002; Yagasaki et al., 2004).

p38α has a typical bi-lobal structure of protein kinases. The N- and C-terminal lobes are linked by the ATP-binding site, which contains the K53, R67, R70, E71 and D168 residues that participate in the ATP and Mg^{2+} stabilization. Dual phosphorylation by MAP2K in the T180 and Y182 residues of the A-loop TGY motif triggers conformational rearrangements that led to the appearance of a new β-sheet away from the ATP and substrate binding sites. In addition, p38α contains the MAPK insert (MKI), which consists of two α-helices that form a lipid-binding site, and the L16 loop, which extends from the C- to the N-lobe (Diskin et al., 2008). The L16 loop contains the acidic CD site, which together with the ED site define the conserved peptide docking sequence recognized by interacting activators, regulators and substrates (Figure 6) (Roux and Blenis, 2004;Tanoue et al., 2000).

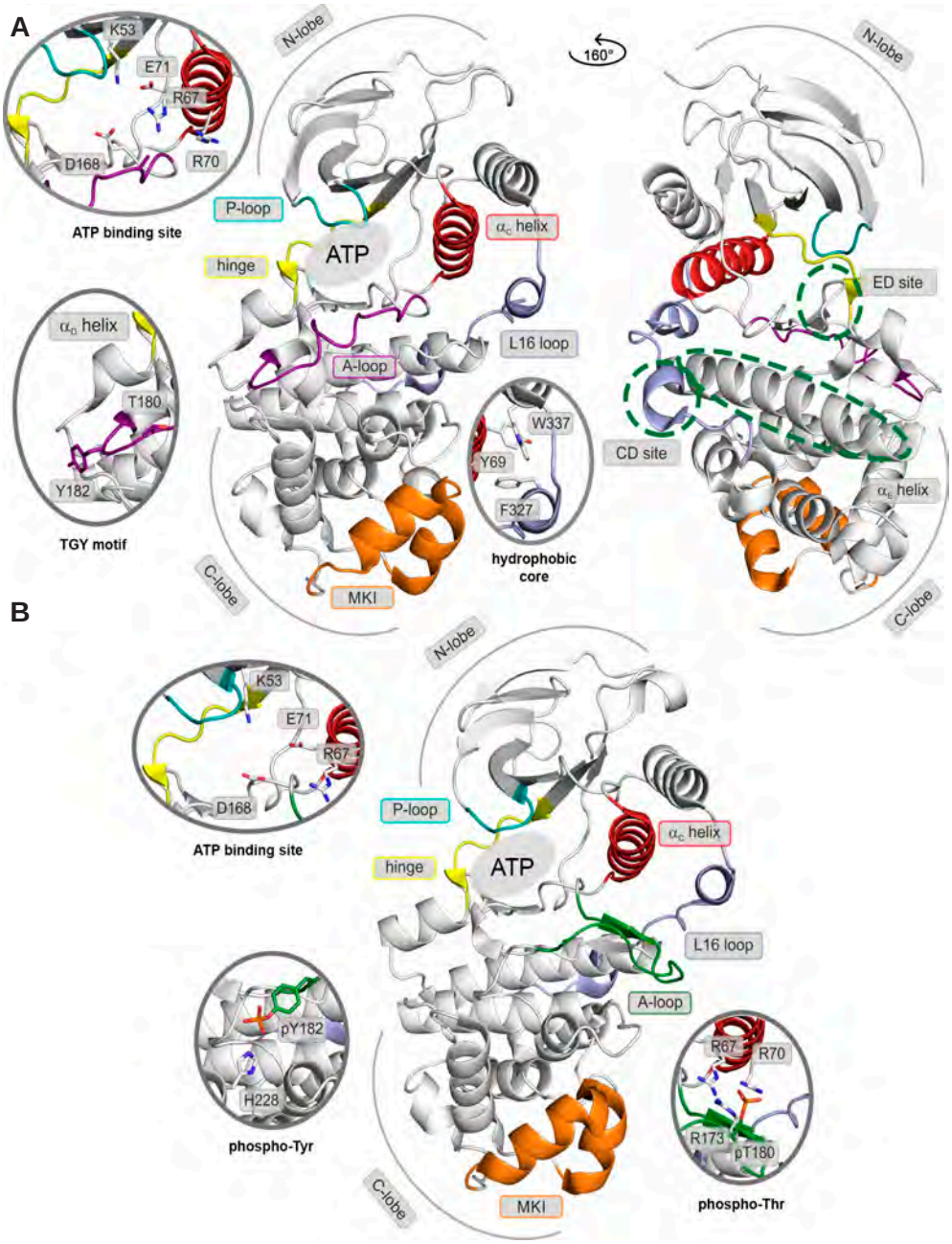

Figure 6. Structural models of p38α MAPK. (**A**) Inactive p38α (PDB 3S3I), and (**B**) active, dually phosphorylated p38α (PDB 3PY3). Main structural elements are indicated as follows: A-loop in purple (inactive) and green (active), αC-helix in red, L16 loop in slate gray, P-loop in cyan, hinge in yellow, MKI in orange, ATP-binding site by a grey filled ellipse and αE-helix CD and ED sites by a green dashed ellipse. Key residues are labelled and shown as sticks. Different regions are indicated by the grey ellipse or green dashed ellipse. Taken from (Kuzmanic et al., 2017).

3.2. Canonical activation of p38α

p38α is inactive in the non-phosphorylated state. It is present both in the cytoplasm and nucleus of quiescent cells and it accumulates in the nucleus of cells subjected to certain stresses. The canonical activation takes place through dual phosphorylation by the upstream MAP2Ks MKK3 and MKK6. In addition, MKK4, an activator of the JNK pathway, can also activate p38α (Cuadrado and Nebreda, 2010). Active p38α can phosphorylate a wide range of substrates at SP/TP sites, including protein kinases, transcription factors, membrane receptors, cytosolic proteins and nuclear proteins (Figure 7). Functions attributed to the different phosphorylated substrates are frequently cell-type specific and include cell proliferation, differentiation, apoptosis, cell-cycle arrest, senescence, RNA splicing regulation and inflammatory cytokine production (Canovas and Nebreda, 2021; Trempolec et al., 2013).

Downregulation of the p38α kinase activity is critical to regulate the intensity and the duration of the signal. This involves several phosphatases, such generic Ser/Thr phosphatases (PP2A and PP2C) and DUSPs (dual-specific phosphatases)/MPKs (MAPK phosphatases), which dephosphorylate both tyrosine and threonine residues (Cuadrado and Nebreda, 2010). In addition, p38α activity can be also attenuated by phosphorylation on Thr123 by GRK2, which decrease the association of p38α with MKK6 (Peregrin et al., 2006).

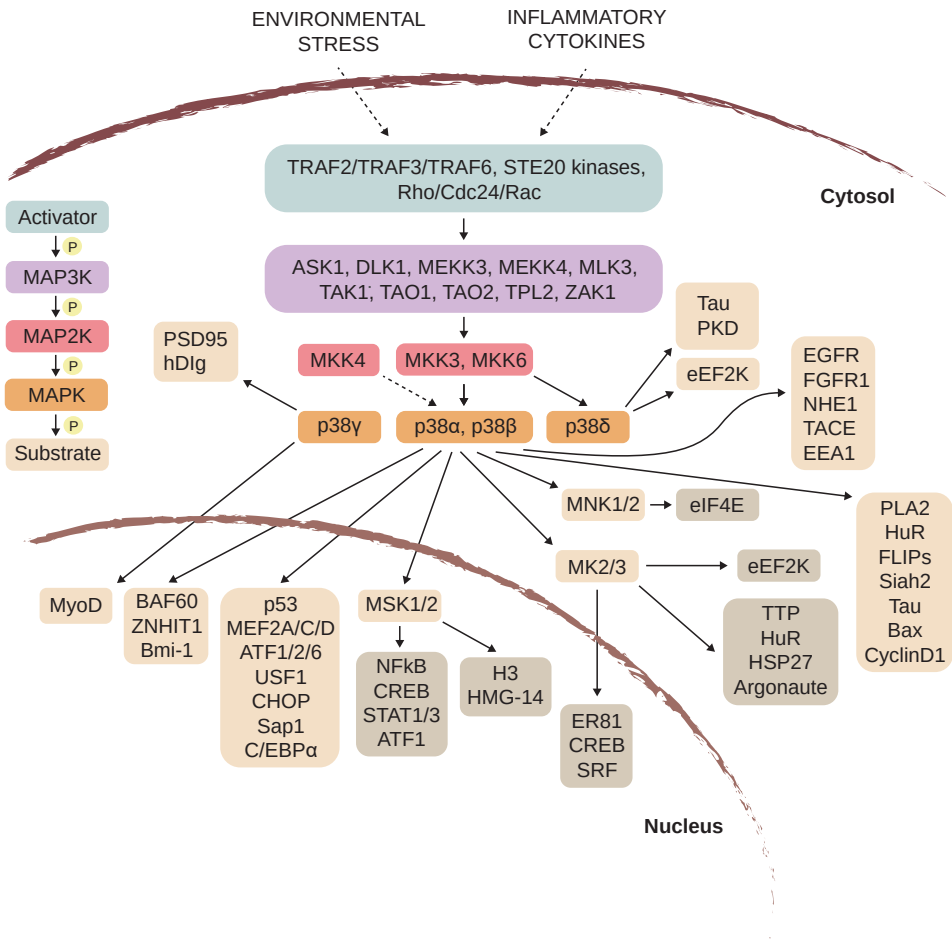

Figure 7. The p38 MAPK pathway. Stimuli such as environmental stresses and inflammatory cytokines can activate p38 MAPKs, which in turn target protein kinases, cytosolic substrates, transcription factors or chromatin remodelers. Adapted from (Cuadrado and Nebreda, 2010).

3.3. Non-canonical activation of p38α

Several MAP2K-independent (non-canonical) mechanisms of p38α activation have been described. First, the scaffold protein TAB1 can bind to p38α and promote a conformational change that induces its autophosphorylation in *cis* (DeNicola et al., 2013; Ge et al., 2002; Ge et al., 2003). This activation mechanism has been shown to be specific to certain stimuli and it has been reported mainly in cardiomyocytes. Second, phosphorylation on Y323 by ZAP70 upon TCR stimulation in

$CD4^+$ T-cells promotes p38α autoactivation (Salvador et al., 2005b). In addition, the GRA24 protein secreted by *Toxoplasma gondii* into the cytoplasm of infected cells can bind to p38α and induce its autophosphorylation and nuclear translocation (Pellegrini et al 2017).

On the other hand, several mutations have been described to disrupt the inactive conformation of the kinase. These include point mutations in D176 and F327 of the L16 loop, which trigger a conformational change in p38α that induces protein dimerization and its trans autophosphorylation on T180 (Diskin et al., 2007). Interestingly, binding to phosphatidylinositol analogues also enhance p38α autophosphorylation via disruption of the stabilization of the L16 loop (Gills et al., 2007).

4.The p38α-TAB1 complex

4.1. Structure of the TAB1-p38α complex

TAB1 is a pseudo phosphatase with no catalytic activity that was originally described as an activator of the MAP3K TAK1 in response to TGFβ stimulation (Conner et al., 2006; Shibuya et al., 1996). In addition to TAK1, TAB1 can interact with p38α and induce its autophosphorylation and activation independently of canonical MAP2Ks (Ge et al., 2002). Moreover, the splice variant TAB1β, which lacks the 69 C-terminal residues (exon 11 and 12, including the TAK1-binding motif), can interact with and activate p38α as well as the full-length TAB1 protein (Ge et al., 2003) (Figure 8).

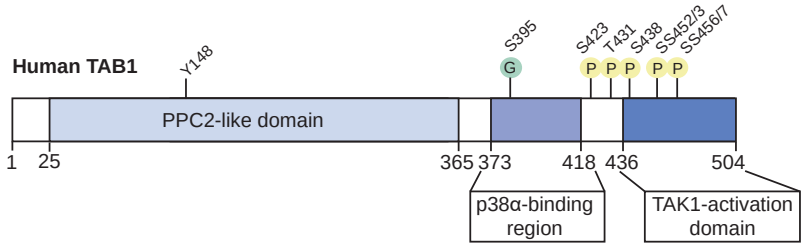

Figure 8. Schematic diagram of full-length TAB1 structure. S423 and T431 are phosphorylated by p38α, whereas S438 is phosphorylated by both JNK1/2 and ERK1/2. In addition, S452/453 and S456/457 are phosphorylated by p38α and TAK1. Moreover, ITCH E3 ubiquitin ligase interacts with Y148 and O-GlcNAcylation (G) takes place at S395. Adapted from (Pathak et al., 2012; Theivanthiran et al., 2015; Wolf et al., 2011).

Mutagenesis (Zhou et al., 2006) followed by NMR and crystallography (DeNicola et al., 2013) analysis has elucidated the key residues (Figure 9) and structural features (Figure 10) of the TAB1-p38α interaction.

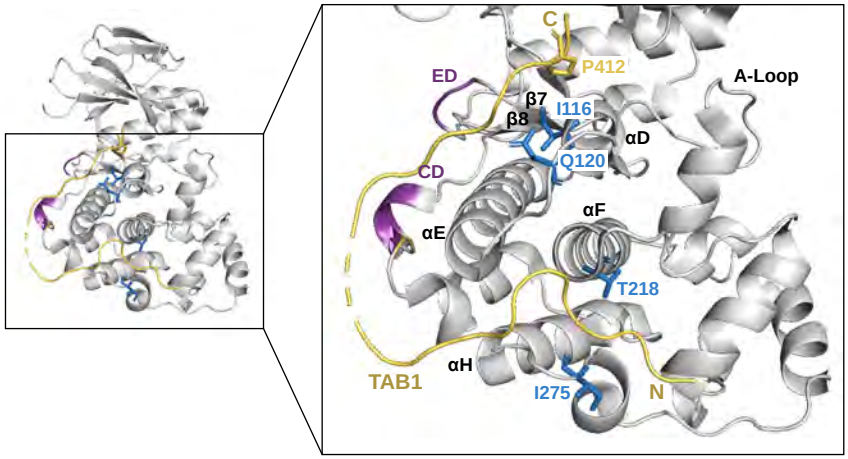

Figure 9. Structural overview of the p38α–TAB1(384-412) complex. p38α and TAB1 are shown in grey and yellow, respectively. Structural elements on p38α are indicated (A-loop, β7-8 strands and αD-H helices) and coloured in purple (ED and CD domains). Important residues involved in the interaction are shown as sticks and coloured in blue (p38α) and yellow (TAB1). p38α and TAB1(384–412) sequences are both from mouse (PDB:4LOO). Adapted from (DeNicola et al., 2013).

TAB1 interacts with p38α in a bipartite manner. The C-terminal 403–412 residues of TAB1 interact with a groove of p38α defined by the αD and αE helices and the reverse turn between the β7 and β8 sheets in the upper canonical docking site (CD and ED domains). Within these residues, P410 of TAB1 is a key docking site for p38α. The N-terminal 384–393 residues interact with a lower hydrophobic pocket created by αF and αH helices, defined as the lower non-canonical docking site of p38α. On the other hand, the p38α Q120 and I116 residues are key to stablish hydrophobic interaction with TAB1. In addition, T218 and I275 are essential for binding to an adjacent site to αD helix (Figure 9) (DeNicola et al., 2013; Zhou et al., 2006). Moreover, T185 and D150 were shown to form a hydrogen bond crucial to initiate the autoactivation reaction, providing the energy to orient the TGY motif toward the kinase catalytic site (Figure 10) (Thapa et al., 2018).

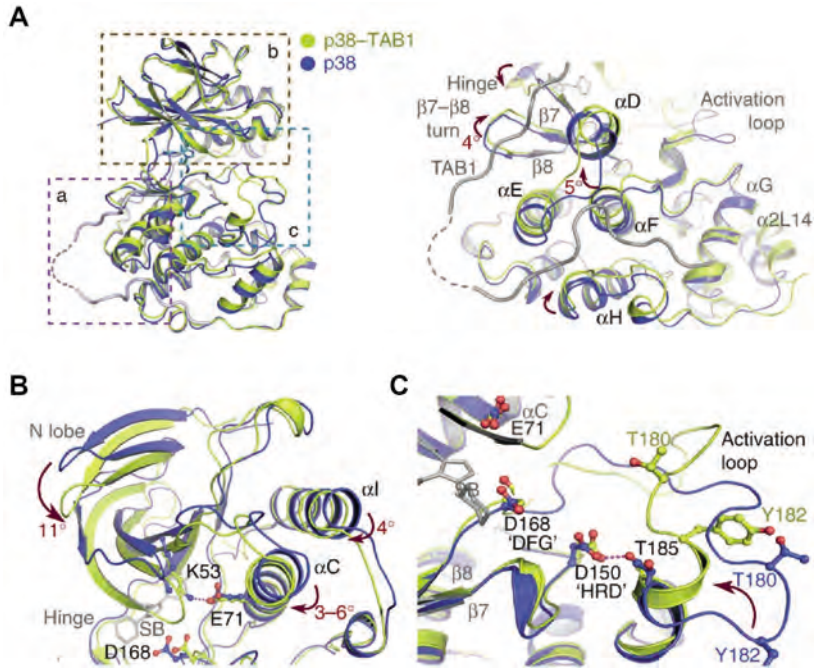

Figure 10. Structural rearrangements within the p38α-TAB1(384–412) complex. All comparisons are with PDB 1P38 (blue). (**A, left**) Location of zoom views in **A (right), B and C panels**. (**A, right**) Accommodation of TAB1 (384-412) peptide, causing displacements in the C-terminal lobe of p38α, including an ~5° upward swing of αF. (**B**) Structural rearrangements in the N-terminal lobe. A downward swing brings the two lobes of the kinase into proximity and is followed by a movement of αC toward the ATP-binding pocket, thus allowing the formation of a K53-E71 salt bridge. (**C**) Conformational changes of the activation loop. The short α-helix at the C-terminus of the activation segment becomes extended. This swings T180 towards D150 and D168, the key residues coordinating ATP-binding. This loop is stabilized by an interaction between Asp150 (from the catalytic HRD-motif) and T185 that may mimic the function in coordinating substrates to phosphorylate them. Adapted from (DeNicola et al., 2013).

Indeed, TAB1 not only binds to p38α and induces its autoactivation, but it also acts as a substrate. p38α phosphorylates TAB1 at S423 and T431, which creates a negative feedback mechanism that inhibits TAK1 activation (Cheung et al., 2003). In addition, activated p38α can phosphorylate TAB1 at S452/S453 and S456/S457, thus affecting TAB1 and p38α subcellular localization and posttranscriptional gene expression (Wolf et al., 2011). It has been reported that TAB1 expression in cultured neonatal cardiac myocytes was able to modulate the intracellular localization of p38α and attenuate canonical MKK3 signalling by competing with MKK3 binding to p38 (Lu et al., 2006).

4.2. TAB1-induced p38α activation and disease

The discovery of TAB1-induced p38α autophosphorylation raised the question of its physiological and pathological relevance. Interestingly, there is evidence indicating that non-canonical p38α activation mechanism is relevant in some cardiovascular diseases. Thus, in cardiomyocytes, p38α activation by TAB1 regulates cell death during myocardial ischaemia-reperfusion injury (IRI) (Fiedler et al., 2006; Li et al., 2005a; Tanno et al., 2003). Other than IRI, this activation mechanism might also play a role in the pathogenesis of cardiac AL (amyloidogenic Ig light chain) amyloidosis by regulating oxidative stress, cardiomyocyte dysfunction and apoptosis (Mishra et al., 2013; Shi et al., 2010). In endothelial cells, it has been described that the G-coupled protein receptors PAR1 and P2Y1 can induce p38α autoactivation and regulate cell permeability *in vitro* as well as vascular leakage *in vivo* (Grimsey et al., 2015; Grimsey et al., 2019).

Furthermore, non-canonical p38α activation has been proposed to play a role in inflammation. Skin lesions formed in knock-out mice of the E3 ubiquitin ligase Itch present high levels of p38α phosphorylation and proinflammatory cytokines. In this scenario, Itch was found to bind TAB1, thus preventing its binding to p38α. Itch deficiency leads TAB1 to bind to and activate p38α, which promotes the subsequent skin inflammatory phenotype (Theivanthiran et al., 2015). *Toxoplasma gondii* infection of macrophages also triggers TAB1-dependent p38α autoactivation and IL-12 production (Kim et al., 2005).

Activation of p38α by TAB1 may also increase pregnancy risks and pre-term birth, as it has been shown that cigarette smoke extract induces oxidative stress in amnion endothelial cells by triggering TGFβ and p38α autoactivation (Richardson et al., 2018).

In senescent T-cells, DNA damage and intracellular low glucose concentration activate AMPK, which triggers p38α autophosphorylation through its recruitment to TAB1. In this setting, T-cell proliferation, telomerase activity and expression of components of the TCR signalosome are inhibited by p38α (Lanna et al., 2014).

Finally, AMPK/TAB1 pathway has been described to mediate non-canonical p38α activation in white adipocytes and increase their browning through ATF2 phosphorylation and UCP1 transcription. This induces thermogenesis and energy expenditure in adipocytes, suggesting its possible relevance for obesity treatment (Matesanz et al., 2017).

5. Role of p38α in cardiomyocytes

While all p38 MAPK family members are expressed in the heart, cardiomyocytes predominantly express p38α, which plays both protective and deleterious roles (Romero-Becerra et al., 2020; Yokota and Wang, 2016). There is evidence that p38α is essential for normal cardiovascular development (Adams et al., 2000; Allen et al., 2000; Mudgett et al., 2000). However, it can act as a negative regulator of neonatal and adult cardiomyocyte proliferation, suggesting that its inhibition would enhance tissue regeneration after damage (Engel et al., 2006a; Engel et al., 2005; Jopling et al., 2012; Ruiz-Bonilla et al., 2008). In contrast, p38γ has been shown to induce muscle regeneration by activating both proliferation and myogenesis in satellite cells (Brien et al., 2013; Gillespie et al., 2009).

5.1. p38α in ischaemia-reperfusion injury

IRI is the pathological condition that results from the recovery of the coronary blood flow supply after a severe impairment usually produced by alterations of coronary atherosclerotic plaques or thrombosis.

Myocardial ischaemia reduces oxygen and intracellular glucose levels of cardiomyocytes, thus inhibiting glycolysis, oxidative phosphorylation and ATP production. To compensate this, cardiomyocytes trigger anaerobic glycolysis, which generates lactate and hydrogen ions (H^+) that lower the cytosolic pH. The elevated pool of H^+ activates the Na^+/H^+ exchanger. The increase of Na^+ uptake leads to the activation of the plasmatic membrane and sarcolemmal Na^+/Ca^{2+} exchanger (NCX), which increases the cytosolic and mitochondrial concentration of Ca^{2+} and impairs myofibrillar contracture. Additionally, there is ROS production as well as mitochondrial changes including the opening of membrane VDAC-1 and MPTP channels, impairment of its membrane potential, electron transport chain dysfunction and matrix swelling. Then, cytochrome C release promotes apoptosis by activating the caspase cascade.

Although tissue reperfusion tries to limit the ischaemic injury, restoration of the respiratory activity and membrane potential enhances ATP synthesis and increases intracellular pH, which worsens cell and tissue damage. The availability of ATP together with increased cytosolic Ca^{2+} levels cause further Ca^{2+} release from the sarcoplasmic reticulum, triggering uncontrolled myofibrillar hypercontraction and reopening MPTP channels. Moreover, Ca^{2+} oscillations activate xanthine oxidases that promote additional oxidative stress, which further exacerbates the

mitochondrial damage and necrosis (Buja, 2005; Hausenloy and Yellon, 2013; Li et al., 2016).

p38α is activated in response to IRI and is associated with a poor cardiac outcome (Tibaut et al., 2017). Interestingly, there is evidence suggesting that p38α and p38β play opposite roles in this setting. While p38α activation triggers cardiomyocyte apoptosis during myocardial ischaemia, p38β protects cardiac cells when activated during ischaemic preconditioning (Saurin et al., 2000). Although the upstream mechanisms leading to p38α activation are not fully elucidated, the energy sensing factor AMPK (Jacquet et al., 2007; Li et al., 2005a) and ROS (Emerling et al., 2005) have both been suggested to play a key role. First, AMPK interacts with TAB1 forming a complex that recruits p38α, which is autoactivated through its interaction with TAB1 (Li et al., 2005a). Alternatively, ROS activate ASK1, which in turn activates p38α through MKK3/6 (Meijles et al., 2020) (Figure 11).

Once activated, p38α phosphorylates many substrates, including TAB1 (De Nicola et al., 2018), MK2, p53 and CREB (Kumphune et al., 2015; Surinkaew et al., 2013); stabilizes HIF1 (Emerling et al., 2005); and promotes Ca^{2+} overload (Song et al., 2020; Zhu et al., 2017). These events lead to mitochondrial dysfunction (Kumphune et al., 2015) and apoptotic cardiomyocyte death (Ashraf et al., 2014). Furthermore, p38α has been shown to promote cardiac inflammation by inducing Reg3 expression (Sakkinen et al., 2016) and to induce fibrosis after myocardial infarction (Molkentin et al., 2017; Wang et al., 2015) (Figure 11).

Consistently, it has been shown that treatment with antioxidants (Du et al., 2010; Guo et al., 2018; Yang et al., 2015) and p38α inhibitors during IRI reduces cardiomyocyte apoptosis, decreases infarct size and improves of ventricular function (Kumphune et al., 2012; Martin et al., 2015).

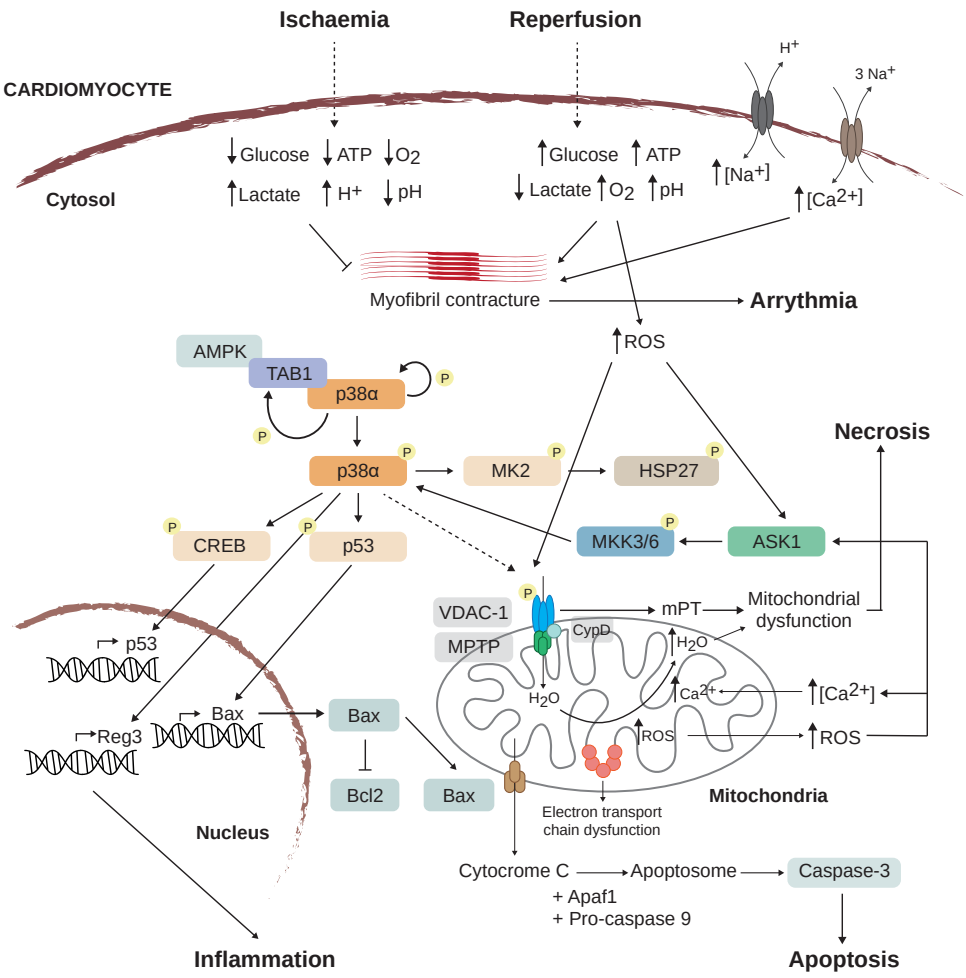

Figure 11. Proposed mechanism for IRI-induced p38α activation and cardiomyocyte damage. Myocardial ischaemia-reperfusion produces changes in the cytosolic Ca^{2+} levels, oxidative stress, myofibrillar hypercontracture and mitochondrial damage. In this setting, p38α is activated and induces the opening of mitochondrial membrane channels and production of ROS, as well as transcription of Reg3 and Bax, which triggers inflammation and cell death, respectively. Adapted from (Buja, 2005; Kumphune et al., 2015; Li et al., 2005a). Solid and dashed lines represent direct and indirect regulation, respectively.

5.2. p38α in heart failure and cardiac arrhythmia

The p38α pathway is activated in heart failure and regulates cardiac remodelling and fibrosis, which is necessary for the differentiation of cardiac fibroblasts to myofibroblasts and for the expression of TNFα and IL6 (Cardin et al., 2003; Li et

al., 2001; Li et al., 2005b; Molkentin et al., 2017; Segura et al., 2014). These data suggest that p38α inhibition would be beneficial to ameliorate heart failure (Dorn and Molkentin, 2004; Kyoi et al., 2006).

However, p38α may contribute to the development of arrhythmia, as it reduces cardiomyocyte contractility by desensitizing the response of myofibrils to Ca^{2+} (Espejo et al., 2017) and also interferes with the cell-to-cell electrical and metabolic coupling through regulation of gap-junctions (Surinkaew et al., 2013). The mechanisms that mediate alterations in Ca^{2+} sensitivity by p38α include dephosphorylation of α-tropomyosin and troponin I proteins (Vahebi et al., 2007), regulation of the sarcoplasmic/endoplasmic reticulum Ca^{2+} transporter SERCA2 (Ca^{2+}-ATPase 2) (Andrews et al., 2003; Kaikkonen et al., 2014; Scharf et al., 2013) and sarcolemmal NCX expression and activity (Menick et al., 2007). There is evidence indicating that p38α also regulates the expression, localization and activity of the gap-junctions protein Cx43 (Salameh et al., 2008; Wang et al., 2011; Yao et al., 2019).

Contractile dysfunction and arrhythmia are common side effects of some chemotherapeutic treatments, such as doxorubicin, which result in heart failure in a dose dependent manner. Doxorubicin-induced cardiotoxicity is associated with ROS production, lipid peroxidation, myofibrillar deterioration, Ca^{2+} homeostasis dysregulation, and iron metabolism changes (Ma et al., 2020). In addition, doxorubicin interacts with the nuclear DNA topoisomerase Top2β, which is highly expressed in cardiomyocytes, and the mitochondrial topoisomerase Top1mt, causing double-strand breaks in both nuclear and mitochondrial DNA, and triggering changes in the expression of genes involved in mitochondrial biogenesis and function (Khiati et al., 2014; Zhang et al., 2012). There is also evidence showing that doxorubicin-induced oxidative stress activates AMPK and p38α, and its inhibition improves cell function and reduces cell death (Guo et al., 2013; Kang et al., 2000; Ruan et al., 2015; Wold et al., 2005).

Although non-canonical p38α signalling is thought to be important in cardiomyocytes subjected to IRI, the implication of this alternative p38α activation mechanism in doxorubicin-induced cardiomyocyte damage has not been investigated yet.

6.p38α as a therapeutic target

6.1. p38 MAPK inhibitors

Historically, p38α has been an attractive druggable target for treating inflammatory diseases. The majority of p38α inhibitors have been designed to bind to the ATP-pocket and compete with ATP binding (Type I, such as SB203580 and PH797804) (Selness et al., 2011; Young et al., 1997), or to allosterically interfere with the binding of ATP (Type II, such as BIRB0796) (Pargellis et al., 2002). The potency of these inhibitors is in the low nanomolar range whereas the cellular concentration of ATP ranges from 1 to 10 mM (Wilson et al., 2016).

Despite being used in several clinical trials, p38α inhibitors have shown limited efficacy and none of them has progressed to phase III yet (Figure 12) (Canovas and Nebreda, 2021). Systemic inhibition of p38α has several limitations. Given the ubiquitous expression of p38α and its importance in regulating cell homeostasis, p38α inhibition sometimes triggers undesirable toxicity, which provokes the use of lower inhibitor doses limiting the therapeutic effect. It is also possible that long-term treatments may lead to the emergence of resistance mechanisms that bypass the effect of p38α inhibition. In addition, some p38α inhibitors lack selectivity and could have off-target actions. For example, ATP-competitive inhibitors may non-specifically target protein kinases in other signalling pathways. The inhibition of p38α may also deregulate feedback loop mechanisms, affecting other cell functions unrelated to the desired one (Genovese, 2009; Hammaker and Firestein, 2010).

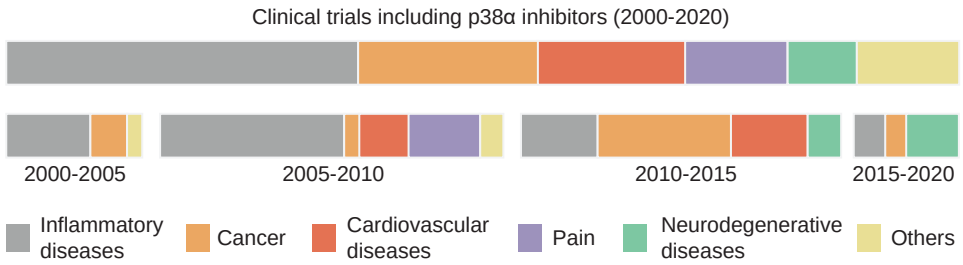

Figure 12. Summary of clinical trials including p38α inhibitors over the past 20 years. Taken from (Canovas & Nebreda 2021).

It is therefore important to investigate other strategies to target p38α and design novel inhibitory compounds that are independent of the catalytic site (Haller et al., 2020).

6.2. Novel strategies to target p38α

In the last decade, several publications have reported inhibitors that bind to allosteric regions in the p38α protein. This may potentially decrease the drawbacks associated with orthosteric inhibitors. In this regards, type IV allosteric kinase inhibitors are aimed to either stabilize inactive conformations of the kinase or block interactions with other proteins (Gomez-Gutierrez et al., 2016).

Several compounds have been designed to target selective p38α substrates. CMPD1 was described as a MK2 substrate specific inhibitor that binds near the p38α active site and induces rearrangements within the ATP-pocket, docking groove and Mg^{2+} binding residues (Davidson et al., 2004). Moreover, UPC-K-005 was reported to bind to the MK2-binding site in p38α and inhibit both MK2 and ATF2 phosphorylation (Gomez-Gutierrez et al., 2016). In addition, UM101 was shown to bind to a pocket near the ED-docking site and inhibit MK2 activation without affecting ATF2 (Shah et al., 2017). Other non-ATP-competitive p38α inhibitors include Compound 10, which binds to a groove formed by the MAPK insert (Comess et al., 2011), and Compound 1, whose binding mechanism remains to be elucidated (Wilson et al., 2016).

Interfering with the interaction between TAB1 and p38α by using cell-penetrating peptides has been reported to have beneficial effects in mouse models of myocardial IRI (De Nicola et al., 2018; Wang et al., 2013) and skin inflammation (Theivanthiran et al., 2015). Recent data have described small molecules derived from admantanes that bind to the non-canonical site on p38α and inhibit TAB1 phosphorylation *in vitro*, but not p38α autoactivation (Nichols et al., 2020). Further studies are needed to address the potential of these compounds to treat cardiovascular and inflammatory diseases.

Modulating the non-canonical activation of p38α downstream of the TCR seems a promising therapeutic approach to treat tumours highly infiltrated tumors with $pY323^{+}$ $CD4^{+}$ T cells (Alam et al., 2015). It was described that binding of GADD45-α to p38α inhibits its phosphorylation on Y323 by ZAP70 (Salvador et al., 2005a). Notably, treatment with a plasma membrane–permeable peptide derived from GADD45-α was shown to reduce the production of proinflammatory cytokines and pancreatic tumour progression in mice (Alam et al., 2015). To date, this alternative signalling pathway remains unexplored by other pharmacological approaches.

These data clearly demonstrate the relevance of exploring the non-canonical activation of p38α as a novel therapeutic approach. However, little is known

about allosteric inhibition of p38α autoactivation. Therefore, the discovery of novel non-canonical inhibitors is needed to exploit this activation mechanism for the treatment of human diseases.

AIM OF THE WORK

The main goal of this study was to discover and characterize modulators of the non-canonical p38α activation pathway.

Specific objectives

- Identification of small molecules that target non-canonical p38α activation (NC-p38i).
- Characterization of the mechanism of action of selected NC-p38i.
- Assessment of the efficacy of NC-p38i in models of non-canonical p38α activation-associated diseases.

MATERIALS AND METHODS

1. Materials

1.1. General buffers and solutions

Specific buffers are specified in the corresponding sections.

10X Electrophoresis running buffer
0.25 M Tris base
2 M glycine
1% SDS
pH 8.3

10X Immunoblotting transfer buffer
0.2 M Tris base
1.5 M glycine

Ponceau staining
0.1% Ponceau Red powder
5% acetic acid

2X HBS buffer
50 mM HEPES
280 mM NaCl
1.5 mM Na2HPO4
pH 7.12

Coomassie staining solution
0.5% Coomassie Blue R250
10% acetic acid
45% methanol

5X Sample loading buffer
250 mM Tris pH 6.8
50% glycerol
250 mM DTT
10% SDS
0.1% bromophenol blue

RIPA buffer
50 mM Tris-HCl
150 mM NaCl
1% NP-40
5 mM EDTA
1 mM DTT
1 mM Na3VO4
1 mM PMSF
10 µg/ml pepstatin A
10 µg/ml aprotinin
10 µg/ml leupeptin
20 mM NaF
1 µM microcystin
2.5 mM benzamidine

10X PBS
1.37 M NaCl
27 mM KCl

Coomassie distaining solution
40% methanol
10% acetic acid

100 mM Na2HPO4
17.5 mM KH2PO4
pH 7.4

1X TBS
0.1 M Trizma base
1.5 NaCl

1.2. Commercial reagents and kits

1.2.1. Cell culture

Reagent	Company	Reference
2-Deoxy-D-Glucose	Sigma	D8375
Collagenase Type II	Worthington	LS004174
Cytosine β-D-arabinofuranoside	Sigma	C1768
D-glucose	Sigma	G8260
DMEM (High glucose)	Sigma	5796
DMSO	Sigma	D8418
Doxorubicin	Accord	677176
10X DPBS	Sigma	D1408
DPBS (Mg^{2+}, Ca^{2+})	Gibco	14040133
DPBS without Mg^{2+} and Ca^{2+}	Gibco	14190144
FBS	Gibco	10500064
FBS Premium	Pan Biotech	P30-3302
Fibronectin	Sigma	F1141
Glutamine	LabClinics	X0550-100
Horse Serum	Gibco	26050088
Lipofectamine 3000	Invitrogen	L3000008
LY-2228820	Axon	1895

M199	Gibco	31150022
Mr.Frosty container	ThermoFisher	5100-0001
Pancreatin	Sigma	P3292
Penicillin/Streptomycin	LabClinics	P11-010
PH-797804	Selleckem	S2726
RPMI	Sigma	C0378
1x TrypLE Express	ThermoFisher	12604013
SB-203580	Selleckem	S1076
TC10 Automated cell counter	BioRad	S06BR2077
Trypsin	Sigma	T3924
Y27632	MedChemtronica AB	HY-10583

1.2.2. Cellular and molecular biology

Reagent	Company	Reference
Acetic acid	Panreac	1.310.081.611
40% Acrylamide/Bis 29:1	BioRad	161-0146
Ammonium Chloride (^{15}N)	Cambridge Isotopes	NLM-467
Ampicillin	Vitro	CAY-14417
Aprotinin	Sigma	A6279
APS	Sigma	A3678
Benzamidine	Sigma	B6506
Bromophenol blue	Sigma	B8026
BSA	Sigma	A7906
Cell strainer 40µm nylon	Falcon	352340
Chloramphenicol	Sigma	C0738
Complete EDTA-free protease inhibitors	Roche	11873580001
DAPI	Life Technologies	P36935

Deuterated water	Silantes	300101400
DTT	GE Healthcare	17-1318-02
Dyalisis membrane (12-14KDa)	Spectra/Por	132678
Dyalisis membrane (6-8KDa)	Spectra/Por	132660
ECL prime WB detection	GE Healthcare	RPN2232
EDTA	Sigma	E46758
EGTA	Sigma	E4378
Ethanol absolute	Panreac	1.410.861.214
Glutathione-Sepharose™ 4 Fast Flow beads	GE Healthcare	GE17-5132-01
Glycerol	Sigma	49782
Glycine	Sigma	G7126
HBSS	Gibco	14175-137
HEPES	Sigma	H3375
IPTG	Sigma	I6758
Kanamycin	Sigma	K4000
Lambda Phosphatase	BioLabs	P0753S
L-glutathione reduced	Sigma	G425
Leupeptin	Sigma	L2884
Luria Broth Base	Invitrogen	12795-084
Lysozime	ThermoFisher	89833
Magnesium cloride	Merck millipore	1.058.331.000
Methanol	Panreac	1.310.911.214
Microcystin	Enzo LifeScience	ALX350012
Nitrocellulose membrane 0.2 mm	GE Healthcare	10600002
NP40	AppliChem	A16960250
Paraformaldehyde 16%	Electron Microscopy Sciences	15710

Pepstatin A	Sigma	P4265
Phusion Polymerase High Fidelity Master Mix	NEB	M0531S
PMSF	Sigma	P7626
Ponceau Red	Sigma	P3504
Potasium chloride	Sigma	P9541
Potasium phosphate dibasic	Sigma	P3786
Proteinase K	Roche	3115852001
Random primers	Invitrogen	48190-011
RNAsin	Promega	N211
SDS	Sigma	71725
Sodium chloride	Sigma	433209
Sodium fluoride	Sigma	S7920
Sodium orthovanadate	Sigma	S6508
Sodium phosphate dibasic	Sigma	255793
Superfrost glass slides	VWR	J1800AMNZ
SYBR Select master mix	ThermoFisher	4472942
TCEP-HCl	Generon	B6055
TEMED	Sigma	T9281
Triton X-100	Sigma	T9284
TRIZMA base	Sigma	T6066
TRIZMA HCl	Sigma	T3253
Tween 20	Sigma	P7949
TRIzol	ThermoFisher	15596026
Triton X-100	Sigma	T9284
VECTASHIELD Antifade Mounting Medium	NOVUS	H-1000-NB

1.2.3. Commercial kits

Reagent	Company	Reference
Cell proliferation kit (MTT)	Roche	11465007001
Mycoalert	Lonza	LT07-318
PureLink on column Dnase set	Invitrogen	121-85-010
Duolink in situ detection (PLA)	Sigma	DUO92007
DC Protein assay kit	BioRad	5000111
QIAfilter plasmid maxi kit	Quiagen	12263
GenElute Plasmid miniprep kit	Sigma	PLN350-1KT
Protein Thermal Shift Dye Kit	Applied Biosciences	4461146
PureLink on column Dnase set	Invitrogen	121-85-010
RNA PureLink Minikit	Ambion	12183018A
Superscript IV reverse transcriptase	Invitrogen	18090010
SYBR Select master mix	ThermoFisher	4472942

2. Methods

2.1. Biochemical and structural assays

2.1.1. Purification of recombinant proteins

Table 1. Recombinant protein expression constructs

Protein	Vector	Resistance
GST-p38α (Hu)	pGEX-4T-3 and pGEX-6P-1	Ampicilin
GST-p38β (Hu)	pGEX-4T-1	Ampicilin
His-Avi-p38α (Hu)	pOPIN	Ampicilin
MBP-MKK6^{DD} (Hu)	pMalc2 (Alonso et al., 2000)	Ampicilin
GST-MK2 (46-400) (Hu)	pGEX-KG (Ben-Levy et al., 1995)	Ampicilin
GST-ATF2 (19-96) (Hu)	pGEX-KG (Livingstone et al., 1995)	Ampicilin
His-SUMO-p38α (Ms)	pOPINS	Kanamycin
GST	pGEX-6P-1	Ampicilin

Hu, Human; Ms, mouse

GST-tagged proteins

Human p38α and p38β proteins with an N-terminal GST-tag were produced in *E. coli* BL21 (BL21-DE3 or BL21-DE3-pLysS). Bacteria was grown in 250-500 ml of LB medium containing ampicillin (50 μg/ml) at 37°C until an OD_{600} of 0.6-0.8 and induced for 3 h at 18°C with 0.05 mM IPTG. Other GST-tagged proteins, including MK2, ATF2 and GST alone, were induced for 3 h at RT with 1 mM IPTG.

After induction, cells were harvested by centrifugation (4000 rpm for 10 min at 4 °C), resuspended in 13.5 ml of cold PBS containing 1 mg/ml lysozyme, 5 mM EDTA, 1 complete EDTA-free protease inhibitor cocktail tablet, and sonicated. Then, Triton X-100 was added to a final concentration of 1% (v/v) and cell debris

was cleared by centrifugation (10000 rpm for 20 min at 4 ºC). Glutathione-Sepharose™ 4 Fast Flow beads were washed in cold PBS buffer, resuspended in PBS (50:50), and 70 µl of the bead slurry were added per 1 ml of supernatant. After 2 h rotating at 4ºC, samples were centrifuged (1000 rpm for 2 min at 4 ºC) and the

After 2 h rotating at 4ºC, samples were centrifuged (1000 rpm for 2 min at 4 ºC) and the supernatant was removed. Beads were washed three times with 10 ml of cold PBS and once with 10 ml of cold 50 mM Tris-HCl pH 8.0, and then centrifuged to remove residual buffer. Beads were incubated with 1 ml of 10 mM L-glutathione in 50 mM Tris-HCl pH 8.0 to elute the proteins. After 2-3 min at RT, beads were centrifuged (1000 rpm for 1 min at 4 ºC), and the supernatant was collected. Protein elution was repeated three times. To remove glutathione, eluted proteins were put into a dialysis bag (12-14 MWCO) and dialyzed against 2 l of buffer containing 20 mM Tris pH 8.0, 50 mM NaCl, 0. 1 mM EDTA, 0.5 mM DTT and 5% glycerol, overnight at 4ºC. Following dialysis, samples were collected, aliquoted and stored at -80°C. An aliquot was analyzed in 10% SDS-PAGE gel and stained with Coomassie blue to quantify the purified proteins using BSA as a reference.

His-Avi-p38α protein

Human p38α with an N-terminal His-tag followed by an Avi-tag sequence were expressed in E.coli BL21-DE3-pLysS. A bacteria pre-culture was grown in 50 ml of LB medium containing kanamycin (50 µg/ml) and chloramphenicol (25 µg/ml) overnight at 37ºC. Then, 10 ml of pre-culture was added to 500 ml of LB medium containing ampicillin (50 µg/ml) and grew at 25ºC until the OD_{600} was 0.5, and then expression was induced for 3 h at 21ºC with 0.2 mM IPTG after adding biotin at 2µM final concentration. After induction, cells were harvested by centrifugation (4000 rpm for 10 min at 4 ºC) and pellets were resuspended in lysis buffer (50 mM $NaPO_4$ pH 8, 300 mM NaCl, 10 mM imidazole, 1 mM PMSF) containing 0.2 mg/ml lysozyme, 10 µg/ml DNAse and 1 complete EDTA-free protease inhibitor cocktail tablet, and sonicated. The protein was purified using His GraviTrap™ TALON Column (Cytiva), and was dialyzed overnight in 50mM $NaPO_4$ pH 7.4 and concentrated using Amicon Ultra 4lm 10K.

The phosphorylated and active His-Avi-p38α was obtained by incubation of the purified protein with MBP-$MKK6^{DD}$.

His-SUMO-p38α protein

Mouse p38α with an N-terminal His-tag followed by a SUMO protease cleavage sequence were expressed in *E.coli* Rosetta-DE3-pLysS and in BL21. Bacteria pre-cultures were grown in 50 ml of LB medium containing kanamycin (50 μg/ml) and chloramphenicol (25 μg/ml) (Rosetta-DE3-pLysS) or in minimal medium (BL21) prepared with ^{15}N ammonium chloride and deuterated water and kanamycin (50 μg/ml) overnight at 37°C (Aragón et al, 2019). Then, Rosetta-DE3-pLysS pre-cultures were grown in LB medium containing ampicillin (50 μg/ml) at 25°C until an OD_{600} of 0.5 and were induced for 3 h at 18°C with 0.2 mM IPTG. Alternatively, BL21 cells were grown at 37 °C to reach an OD_{600} of 0.8-1.0 and induced overnight at 20°C with 0.2 mM IPTG. After induction, cells were harvested by centrifugation (4000 rpm for 10 min at 4 °C) and pellets were stored at -80°C until protein purification.

Thawed cells from 1 l culture were resuspended in 50 ml of cold lysis buffer containing 50 mM Tris pH 7.4, 500 mM NaCl, 10 mM imidazole and 1 complete EDTA-free protease inhibitor cocktail tablet, and sonicated. Cell debris was cleared by centrifugation (13000 rpm for 30 min at 4 °C) and the supernatant was passed through a 0.45 μm filter. Then, protein was purified by FPLC using an NGC Quest 10 Plus Chromatography system (BioRad) on a HisTrap HP column 5ml (GE Healthcare, 17-5248-01) at 4°C, which was previously equilibrated with buffer A (50 mM Tris pH 7.4, 500 mM NaCl, 10 mM imidazole). Protein was eluted by applying 16 CV (column volumes) of a linear 10 mM to 500 mM gradient of imidazole.

Fractions from each chromatographic step were analysed by 12% SDS-PAGE gel and stained with Coomassie blue. Cleavage of His-SUMO-tag was performed overnight at 4°C (6-8KDa membrane) with in-house purified Recombinant His-Tagged SUMO protease (50μl at 2.5mg/ml for 2.5mg of fusion protein) against 3 l of dialysis buffer containing 25 mM Tris pH 7.4, 150 mM NaCl, 10 mM $MgCl_2$ and 1 mM DTT. Cleaved p38α was checked by SDS-PAGE stained with Coomassie blue. The cleaved protein was dilute to 50mM of NaCl and was loaded onto a HiTrap Q HP anion exchange column 5 ml (GE Healthcare, 17-1154-01) at 4°C, which was previously equilibrated with buffer A (50 mM Tris pH 7.4, 50 mM NaCl, 10 mM $MgCl_2$, 5% glycerol and 1 mM DTT) and buffer B (50 mM Tris pH 7.4, 500 mM NaCl, 10 mM $MgCl_2$, 5% glycerol and 1 mM DTT) (5 CV of buffer A + 5 CV of buffer B + 5 CV of buffer A). Protein was eluted by applying 40 CV of a linear 50 mM to 500 M NaCl gradient. Fractions from each chromatographic step were analysed by 12% SDS-PAGE and stained with Coomassie blue. Fractions containing p38α were further purified by size-exclusion chromatography using

a predgrade HiLoad 16/600 Superdex 75 column (GE Healthcare) in buffer C (20 mM Tris pH 7.5, 100 mM NaCl, 10 mM $MgCl_2$, and 5 mM TCEP). Pure p38α protein was quantified using a NanoDrop One Microvolume UV-Vis Spectrophotometer (Thermo Scientific). Finally, protein was concentrated to 10-15 mg/ml with Amicon Ultra-4 filter units (10KDa) and used for crystallography or to 5-10mg/ml for NMR experiments.

Expression, purification and mass spectrometry analysis of the [^{2}H,^{15}N]p38α protein used for NMR was performed by Eric Aragón and Dr. Lidia Ruiz (Macias Lab, IRB Barcelona).

2.1.2. Cloning

The cloning method as described in (Gibson et al., 2009) was used to generate the following constructs.

Human p38α was amplified from pGEX-4T-3-p38α and was inserted into BamHI/XhoI of the pGEX-6-P1 expression vector with primers:

Construct	**GST-p38α**
Fw 5'-3'	CCAGGGGCCCCTGGGATCCATGTCTCAGGAGAGGCCCAC
Rv 5'-3'	CGATGCGGCCGCTCGAGTCAGGACTCCATCTCTTCTTGGTCA

Mouse p38α was amplified from pET30-p38α and inserted into KpnI/HindIII of the pOPINS expression vector with primers:

Construct	**GST-p38α**
Fw 5'-3'	GCGCATCGCGAACAGATCGGTGGTGGTATGTCGCAGGAGAGGCCC
Rv 5'-3'	GGTGTTTAAATGGTCTAGAAAGCTTTCAGGACTCCATTTCTTCTTGGTCAAG

The PCR parameters were as follows: melting temperature at 58°C and elongation at 72°C for 20 sec.

2.1.3. Dephosphorylation of p38α with Lambda Phosphatase

Purified and dialyzed recombinant GST-p38α protein (5 μg) from *E. coli* BL21 *E. Coli* was dephosphorylated with 1 μl of Lambda Phosphatase (BioLabs) in 20 μl of 1X PMP Buffer (50 mM HEPES 100 mM NaCl, 2 mM DTT and 0.01% Brij 35) containing 1 mM $MnCl_2$. After 2 h at 37°C, 2 μl of 100 mM Na_3VO_4 were added to stop the reaction. Dephosphorylated GST-p38α protein was stored in aliquots at -80°C.

2.1.4. p38α kinase activity assays

Phosphorylation of p38α by MKK6

Purified and dialyzed recombinant GST-p38α protein (4 μg) was incubated with purified MBP-$MKK6^{DD}$ (1 μg) in 20 μl of buffer containing 50 mM Tris-HCl pH 7.5, 2 mM DTT, 10 mM $MgCl_2$, 100 μM Na_3VO_4, 1 mM PMSF, 10 μg/ml aprotinin, 10 μg/ml leupeptin and 200 μM ATP for 30 min at 37 °C. Reactions were stopped by the addition of 5X sample loading buffer and boiling at 95 °C for 5 min. Phosphorylation of GST-p38α was confirmed by western blotting using antibodies that recognize the two phosphorylation sites in the activation loop of p38α.

Basal p38α autophosphorylation

Dephosphorylated GST-p38α protein (2 μg) was incubated with 600 μM ATP in 20 μl of buffer containing 100 mM NaCl, 20 mM Tris-HCl pH 7.5, 2 mM DTT, 2 mM $MgCl_2$ for 2 h at 37°C. Reactions were stopped by the addition of 5X sample loading buffer and boiling at 95 °C for 5 min. Autophosphorylation was detected by western blotting as above.

TAB1-induced p38α autophosphorylation

A peptide corresponding to amino acids 386-414 of human TAB1 [RVYPVSVPYS-SAQSTSKTSVTLSLVMPSQ] (GenScript) was resuspended in 50 mM Tris-HCl pH 7.5, at a concentration of 100-300 mM and stored in aliquots at -80°C. Non-phosphorylated GST-p38α protein (2 μg) was incubated with 15 μM TAB1 peptide in 20 μl of buffer containing 100 mM NaCl, 20 mM Tris-HCl pH 7.5, 2 mM DTT, 2 mM $MgCl_2$ and 600 μM ATP for 2 h at 37°C. Reactions were stopped by the addition of

5X sample loading buffer and boiling at 95 °C for 5 min. Autophosphorylation was detected by western blotting as above.

Phosphorylation of substrates by active p38α

Active GST-p38α (200 ng) was prepared by incubation with MKK6 as describe above, and was incubated with purified GST-ATF2 or GST-MK2 proteins (0.5 μg) in 20 μl of buffer containing 50 mM Tris-HCl pH 7.5, 2 mM DTT, 10 mM $MgCl_2$, 100 μM Na_3VO_4, 1 mM PMSF, 10 μg/ml aprotinin, 10 μg/ml leupeptin and 200 μM ATP for 30 min at 30 °C. Reactions were stopped by the addition of 5X sample loading buffer and boiling at 95 °C for 5 min. Phosphorylation of ATF2 or MK2 was detected by western blotting using antibodies that recognize the corresponding p38α phosphorylation sites.

2.1.5. Surface plasmon resonance assay

Surface plasmon resonance assays were performed in collaboration with Dr. Isabelle Brun-Heath (Orozco Lab, IRB Barcelona) using a Biacore T200 instrument at 25°C (Cytiva) (Bukhtiyarova et al 2004).

Inactive (non-phoshorylated) and active (phosphorylated) biotinylated His-Avi-p38α protein were coupled to a high-affinity streptavidin (SA) sensor (Cytiva, 29104992) in buffer containing 10 mM Tris, 150mM NaCl and 5% DMSO using the manufacturer's directions. Of the four channels in the chip, channel 1 did not contain any protein, channel 2 contained inactive non-phosphorylated protein, and channel 3 contained phosphorylated protein. The immobilization level was 2200 resonance units (RU) for both proteins.

Kinetic parameters were measured by injecting different concentrations of each compound (SB203580, 3-400 nM; NC-p38i 37 and A02, 0.2-25 μM; 60 and E2.2, 2-100 μM) to the immobilized protein at a flow rate of 60 μl/min. Washing and solvent correction steps were performed between each compound. All samples were prepared as 2-fold serial dilutions in the experimental buffer. Affinity and kinetics data were determined using the BiacoreT200 Evaluation Software.

2.1.6. Thermal shift assay

Thermal shift assays were performed in 96-well plates (MicroAmp Fast 96 well plates, Applied Biosystem, 4346907) using (BioRad) instrument. Samples were prepared in triplicates by mixing purified GST-p38α or GST proteins (1.5 μM) with assay buffer (20 mM TRIS pH 7.5, 100 mM NaCl, 2mM $MgCl_2$, 2 mM DTT), Protein Thermal Shift Buffer (1X final concentration, Applied Biosystem Protein Thermal Shift™ Kit) and NC-p38i compounds at different concentrations (10 mM stock in 100% DMSO) or the equivalent volume of DMSO as a control. Samples were incubated at RT for 30 min prior to the assay. 1X SYPRO Orange was added before reading the plate. Fluorescence intensity was measured at 1ºC intervals from 25°C–95°C at a rate of 0.5°C/s. All measurements were performed in triplicates and mean values were reported for all compounds to calculate their ΔT_m relative to DMSO control samples.

2.1.7. Isothermal titration calorimetry

Isothermal titration calorimetry experiments were carried out in a NanoITC Low volume calorimeter (TA instruments).

GST-p38α protein at 260 μM (50 μl) was injected into a rapidly mixing solution (200 rpm) of $TAB1_{386-414}$ peptide at 26 μM (320 μl) within the calorimetric cell (De Nicola et al 2013). In addition, NC-p38i at 260 μM (50 μl) were injected into a rapidly mixing solution (200 rpm) of GST-p38α at 26 μM (320 μl) within the calorimetric cell. All reagents were prepared in a buffer containing 20 mM Tris pH 8, 50 mM NaCl, 5% glycerol and 1mM TCEP. A total of 17 injections of 2.97 μl were made during the experiment.

After completion of the experiment, Nanonalize de TA data software was used to analyse the result. The heat of the first injection was discarded from the analysis to avoid artefacts due to diffusion that occur during the long equilibrium period which affected the local protein concentration near the syringe. Control experiment injecting identical amounts of ligands into buffer alone were performed to subtract the dilution heat for each experiment.

The data fitting gave us the values for binding stoichiometry (n), binding affinity (K), enthalpy (ΔH) and entropy (ΔS) and Gibbs free energy (ΔG) was calculated according to the formula $\Delta G = \Delta H - T\Delta S$.

2.1.8. Fluorescence polarization assay

Fluorescence polarization assays were performed in low volume 384-well plates (non-binding surface, black, Corning, 3575) using an Infinite® 200 (Tecan) microplate reader. GST-p38α protein was dialyzed overnight against assay buffer containing 20 mM Tris pH 7.5, 100 mM NaCl, 1 mM DTT and 10 mM $MgCl_2$. The fluorescent N-terminally labelled-fluorescein isothiocyanate (FITC)-$TAB1_{386-414}$ peptide (ChinaPeptides) stock was prepared at 10 mM in 100% DMSO.

For direct binding assays, FITC-$TAB1_{386-414}$ (10 nM) and non-phosphorylated GST-p38α (0.17-22 μM) were prepared in triplicates in assay buffer (30 μl/well) and incubated for 1h at RT. The FP signal (mP) was measured at an excitation wavelength (λex) of 485 nM and emission wavelength (λem) of 535 nM. The concentration of GST-p38α that increased the FP signal up 80% was used to perform the competitive assays.

For competition assays, FITC-$TAB1_{386-414}$ (10 nM) and non-phosphorylated GST-p38α (5.6 μM) were prepared in triplicates in assay buffer (30 μl/well) in presence of either non-labelled $TAB1_{386-414}$ peptide or NC-p38i at increasing concentrations (diluted from a 10 mM stock in 100% DMSO). The equivalent volume of DMSO (1%) was added as a control. The FP (mP) signal was measured after incubation for 1h at RT.

2.1.9. NMR spectroscopy

NMR experiments were performed by Dr. Maria Macias and Dr. Pau Martin (Macias Lab, IRB Barcelona).

2D ^{1}H-^{15}N Transverse Relaxation Optimized Spectroscopy (TROSY) experiments were performed to obtain the spectra of p38α alone or in complex with either $TAB1_{386-414}$ peptide (2 equivalents) or NC-p38i (5 equivalents), or both simultaneously in buffer containing 20 mM Tris pH 7.5, 100 mM NaCl, 2 mM TCEP and 10 mM $MgCl_2$. Measurements were performed in a Bruker Avance III 600 MHz spectrometer equipped with a quadruple (^{1}H, ^{13}C, ^{15}N, ^{31}P) resonance cryogenic probe head and a z pulsed-field gradient unit at 293 K. All spectra were acquired and processed with the Bruker TopSpin 3.5pl7 software and were analysed with CARA (Bartels et al., 1995). Chemical-shift variations were determined by comparison of the 2D ^{1}H-^{15}N -TROSY spectrum of free p38α with that of p38α-$TAB1_{386-414}$ and p38α-NC-p38i, respectively, and mapped onto the structure of p38α (PDB:3MGY) using the assignments from BMRB:27273.

2.1.10. X-ray crystallography

Crystallography experiments were performed in collaboration with Dr. Joan Pous at the Automated Crystallography Platform (PAC) of IBMB-CSIC and IRB. Crystals harvesting, data collection and analysis were performed by Dr. Joan Pous (PAC), Blazej Baginski and Dr. Radoslaw Pluta (Macias Lab, IRB Barcelona).

Full-length mouse p38α protein (10-15 mg/ml) was crystallized in the presence of different combinations of NC-p38i (p38α:NC-p38i, 1:1.5 ratio) and SB203580 (1 mM) in a solution containing 20 mM Tris pH 7.5, 100 mM NaCl, 10 mM $MgCl_2$, and 5 mM TCEP. Standard screenings and optimizations were done in a Tecan Evo 100 (Table 2). The resulting crystallization conditions and the protein-ligands mix were dispensed in volumes of 200 nl each using a Phoenix robot from ARI. Crystal complexes were grown by sitting-drop vapor diffusion and monitored on Bruker Crystal Farmsat in 4 ºC or 20 ºC.

Table 2. Summary of crystallization experiments

Crystallization plates	51
Crystallization conditions	9792
Diffracted crystals	196
Collected datasets	65
Indexed, processed and molecular replacement performed datasets	27
Datasets refined	15
Datasets selected	2

Crystals were cryoprotected in mother liquid solution supplemented with glycerol and flash-frozen in liquid nitrogen in a polyamide loop. The X-ray data were collected at 100 K from an Orthorhombic crystal using a PILATUS 6M detector on BL13-XALOC at the ALBA Synchrotron Light Source (Barcelona) (Juanhuix et al., 2014). In each case, a total rotation of 180° was collected at a wavelength of 0.9792 Å with an exposure time of 0.1 s and an oscillation of 0.2°.

Data reduction and processing were carried out using iMOSFLM (Battye et al., 2011), POINTLESS and SCALA from CCP4 (Winn et al., 2011), and autoPROC (Vonrhein et al., 2011) with STRANISO (Tickle et al., 2018). Structures were solved by molecular replacement of the template structure file PDB:4LOO using Phaser and refined using REFMAC5 (Murshudov et al., 2011), Coot (Emsley et al., 2010)

and Phenix software suite (Liebschner et al., 2019). PDB-REDO web server was also used during structure refinement (Joosten et al., 2014) (Supplementary Table 1). Graphical representations were prepared using PyMOL (Schrödinger, LLC) and Chimera (Pettersen et al., 2004).

2.2. Cellular and molecular biology assays

2.2.1. Cell culture

Cell maintenance

HEK293T, H9c2, U2OS, BBL358, MCF-7, MDA-MB-231 cells were cultured DMEM (high glucose) medium supplemented with 10% FBS, 1% penicillin/streptomycin and 1% L-glutamine. BT549 cells were cultured in RPMI supplemented with 10% FBS, 1% penicillin/streptomycin and 1% L-glutamine. Cells were maintained at 37°C and 5% CO2.

For sub-culturing and passage, cells were washed with 1X DPBS and incubated with trypsin-EDTA for 5 min at 37°C. Then, complete fresh media was added, cells were counted automatically in a Bio-Rad TC20™ cell counter and diluted as desired depending on the confluence.

Human iPSC-derived cardiomyocytes were cultured following providers' instructions (NCardia).

Cell collection

For harvesting, cell cultures were washed with 1X DPBS and trypsinized. Then, cells were resuspended in complete fresh media and centrifuged at 1200 rpm for 5 min. Media was aspirated, and the pellet was washed with 1X DPBS. Cell suspension was again centrifuged, and supernatant was discarded. The final cell pellet was resuspended according to the specific procedures.

Cell freezing and thawing

For freezing, cells from 70-85% confluent culture plates were collected as above and resuspended in freezing media consisting of 90% FBS and 10% DMSO and transferred to 1.5 ml cryo-tubes. Specifically, H9c2 cells were frozen in 95% DMEM and 5% DMSO. Cryo-tubes were stored in a Mr. Frosty container at -80°C

for up to one week and then transferred to liquid nitrogen for long term storage.

For thawing, frozen cells were placed in a 37°C water bath for 2-3 min. Then, cells were diluted in fresh media and centrifuged at 1200 rpm for 5 min to remove DMSO. The supernatant was aspirated, cells were resuspended in fresh complete media and transferred to a new plate. Next day, the media was replaced to remove dead cells.

Mycoplasma detection

Cells were routinely tested using Mycoplasma Detection Kit. 100 µl of cell media were taken, centrifuged and transferred to a test tube. First, MycoAlert Reagent (A, 100 µl) was added and luminescence was measured after 5 min incubation. Then, MycoAlert Substrate (B, 100 µl) was added and luminescence was measured after 10 min. The ratio of B/A was used to determine the mycoplasma status according to the manufacturer´s protocol.

Cell treatments

ATP-competitive inhibitors of p38α and NC-p38i compounds were prepared in 100% DMSO and stored in aliquots at -20°C.

Inhibitors were used at the indicated concentrations and for the indicated times depending on each experiment.

2.2.2. Cellular protein extraction and quantification

For protein extraction, cell plates were placed on ice and cells were washed with ice cold 1X PBS. Then, cells were lysed in 1X RIPA buffer using a scrapper. Samples were incubated for 30 min on ice and then centrifuged at 15000 rpm at 4°C for 15 min. Then, supernatants were collected and processed by western blotting or frozen at -80°C.

Total protein was quantified using RC DC protein assay kit according to manufacturer's instructions. Protein concentration was measured at 750 nm using Epoch 2 spectrophotometer (BioTek) and a BSA standard curved as a reference.

2.2.3. Western blotting

Cell lysates (30-40 µg of protein) were prepared in 1X loading buffer and boiled for 5 min at 95°C. Then, samples were loaded onto different types of SDS-polyacrylamide gels (SDS-PAGE) depending on protein size. Gel composition is shown in Table 3.

Table 3. Composition of SDS-polyacrylamide gels

	Stacking	8% SDS-PAGE	10% SDS-PAGE	12% SDS-PAGE
Tris-HCl 1.5 mM (pH 8.8)	--	2.5 ml	2.5 ml	2.5 ml
Tris-HCl 1M (pH 8.8)	625 µl	--	--	--
40% Acrylamide/Bis (29:1)	500 µl	2 ml	2.5 ml	3 ml
H2O	3.8 ml	5.3 ml	4.9 ml	4.3 ml
10% SDS	25 µl	50 µl	50 µl	50 µl
10% APS	50 µl	100 µl	100 µl	100 µl
TEMED	5 µl	8 µl	8 µl	8 µl

Proteins were separated by SDS-PAGE for 1.5 h at 100-120 V. After electrophoresis, proteins were transferred from the gel to a nitrocellulose membrane using a wet-transfer system (Mini Trans-Blot Cell, BioRad). After the transfer, membranes were stained with Ponceau S solution to assess the transfer. Membranes were rinsed in distilled water and distained in 1X PBS. Then, membrane was blocked in 5% non-fat dry milk in 1X PBS for 1 h at RT. The primary antibody diluted in 5% BSA in TBS-Tween 0.05% was added to the membrane and incubated overnight at 4°C or for 2h at RT. Then, membranes were washed three times with PBS and incubated with the secondary antibody diluted in 2.5% BSA in TBS-Tween 0,05% for 1 h at RT. Finally, membranes were washed three times as above and protein-bound antibodies were detected using the Odyssey Infrared Imaging System. The antibodies used are indicated in Tables 4 and 5.

Table 4. Primary antibodies used for western blotting

Antibody	Dilution	Company	Reference
c-Myc	1:1000	Abcam	Ab9132
Caspase-3	1:1000	Cell Signalling	9662
Flag	1:1000	Sigma	F3165.2MG
GFP	1:1000	Santa Cruz	sc9996
GST	1:1000	Santa Cruz	sc138
HSP27	1:1000	Santa Cruz	sc-1049
HSP27 phospho-S82	1:1000	Cell Signaling	2401
MK2 phospho-T334	1:500	Cell Signaling	3007
MKK6	1:500	Homemade	(Ambrosino et al., 2003)
p38α	1:1000	Cell Signaling	9218
p38α	1:1000	Santa Cruz	sc81621
p38 phospho-T180/ Y182	1:1000	Cell Signaling	9211
p38 phospho-T180/ Y182	1:1000	BD Biosciences	612288
TAB1	1:1000	MRC	S823A
TAB1 phospho-S423	1 ug/ml	MRC	S739A
Tubulin	1:10000	Sigma	T9026

Table 5. Secondary antibodies used for western blotting

Antibody	Dilution	Company	Reference
Goat anti-Mouse IgG (AlexaFluor 680)	1:5000	Invitrogen	A21057
Goat anti-Rabbit IgG (AlexaFluor 680)	1:5000	Invitrogen	A21076
Donkey anti-Goat IgG (IRDye 800CW)	1:5000	Licor	926-33214

Donkey anti-Mouse IgG (IRDye 800CW)	1:5000	Licor	926-32212
Rabbit anti-Sheep IgG (DyLight 800)	1:5000	Invitrogen	SA5-10060
Donkey anti-Sheep IgG (HRP)	1:5000	Santa Cruz	sc2473

2.2.4. Cell transfection

Mouse myc-tagged p38α and GFP-tagged TAB1 sequences were inserted into the pcDNA3 mammalian expression vector and used for transient transfection.

Transfection of HEK293T cells with $CaCl_2$

HEK293T cells seeded in 10 cm plates were used for transfection when reached a 60-70% confluency. DNA (5 µg myc-p38α, 10 µg GFP-TAB1) was dissolved in 450 µl of sterile water, and 50 µl of 2.5 M $CaCl_2$ were added drop by drop and incubated for 5 min at RT. Afterwards, 500 µl of 2X HBS were added drop-wise with bubbling and incubated for 20-30 min at RT. The final mix (1 ml) was added to cells and incubated overnight. Next day, the media was replaced by fresh DMEM to avoid $CaCl_2$ toxicity. After 24 h, cells were trypsinized and seeded in 60 mm plates to perform experiments.

Transfection of U2OS cells with Lipofectamine 3000

U2OS cells were seeded in coverslips in 6-well plates and used for transfection with Lipofectamine 3000 following manufacturer's instructions. Briefly, DNA (2.5 µg) was mixed with 125 µl of Opti-MEM and 10 µl of p3000 reagent. In parallel, 9 µl of lipofectamine were mixed with 125 µl of Opti-MEM. After 5 min, the mixture containing the DNA was transferred to the tube containing the lipofectamine and mixed. After 10 min, the mixture was added to the cells in 6-well plates cultured in media without antibiotics. Medium was replaced after 16 h.

2.2.5. Proximity ligation assay

U2OS cells were transfected with the required plasmids as indicates in the *Cell transfection* section (2.2.4), grown on coverslips, washed with PBS and fixed for 20 min with ice-cold methanol (-20°C). After fixation, cells were incubated with anti-Myc and anti-GFP primary antibodies (Table 3) as for a normal immunofluorescence. The next day, PLA was performed following manufacturer's instructions. Briefly, anti-mouse and anti-rabbit antibodies were diluted 1:5 in blocking buffer and incubated 20 min at RT. Then, coverslips were incubated with the antibodies for 1 h at 37°C in a humid chamber. After incubation, coverslips were washed with buffer A (0.01 M Tris HCl, 0.15 M NaCl and 0.05% Tween 20) and incubated with the ligation reaction (ice-cold ligase diluted 1:40 in 1X ligation buffer provided in the kit) for 30 min at 37°C in humidity chamber. Coverslips were washed again with buffer A and incubated in the amplification reaction (polymerase diluted 1:80 with 1X amplification buffer supplied in the kit) for 100 min at 37°C in humidity chamber. The, samples were washed three times with buffer B (0.2 M Tris HCl, and 0.1 M NaCl) and dried. Coverslips were placed in superfrost glass slides with ProLong Gold antifade DAPI mountant or VECTASHIELD Antifade Mounting Medium.

2.2.6. NanoBRET target engagement assay

These experiments were performed by Aurelia Bioscience as indicated in the following protocol.

HEK293T cells were trypsinized, counted and resuspended in Opti-MEM containing 1% FBS. Then, cells were transfected in suspension with a mixture of Transfection Carrier DNA (9 μg/ml) and NanoLuc fusion p38α vector (1 μg/ml) using 30 μl of FuGENE HD transfection reagents in Opti-MEM without serum and seeded into 96-well plates for 20 h to allow NanoLuc fusion p38α expression.

To prepare 1X Tracer for BRET assay, 100X NanoBRET Tracer (in 100% DMSO) was diluted 1:4 in Tracer Dilution Buffer (20X) and added directly to cells (1:20). Then, the plates were mixed for 15 s at 700 rpm. NC-p38i compounds were prepared by serial dilutions in Opti-MEM and added to cells. Plates were again mixed for 15 s at 700 rpm and further incubated for 2 h at 37°C 5% CO_2. Finally, plates were incubated for 15 min at RT to cool down before performing BRET measurements.

Immediately prior to BRET measurements, 3X Complete NanoBRET Nano-Glo Substrate was prepared in OptiMEM without serum or phenol red (1:166

dilution of NanoBRET Nano-Glo Substrate plus a 1:500 dilution of Extracellular NanoLuc Inhibitor in OptiMEM without serum or phenol red) and mixed gently by inversion. 50 µl were added per well of 3X Complete NanoBRET Nano-Glo Substrate and incubated 2-3 min at RT. Measurements were done within 10 min of substrate activation. Following addition of NanoBRET Nano-Glo Substrate, donor emission (e.g. 450 nm) and acceptor emission (e.g. 610 nm or 630 nm) were measured using a NanoBRET-compatible luminometer. To generate raw BRET ratio values, acceptor emission values (e.g. 610 nm) were divided by the donor emission value (e.g. 450 nm) for each sample. Then, raw BRET units were converted to % inhibition for interpretation of the results.

2.2.7. Simulated ischaemia-reperfusion in H9c2 cells

H9c2 cells were seeded in 60 mm plates and grown for 24 h. Then, medium was replaced and NC-p38i compounds or p38α ATP-competitive inhibitors were added for 24 h pre-treatment.

For simulated ischaemia, the medium was changed to 3 ml of Ischemic Buffer (137 mM NaCl, 12 mM KCl, 0.5 mM $MgCl_2$, 0.9 mM $CaCl_2$, 4 mM HEPES, 10 mM 2-deoxy-glucose and 20 mM sodium lactate, pH 6.2) (Esumi et al. 1991) containing either DMSO, p38α ATP-competitive inhibitors or NC-p38i compounds. Cells were kept in H35-hypoxistation chamber flushed with 0.1% O_2 5% CO_2 and 95 % N_2 (65% HR) for 2 h. For simulated reperfusion, cells were switched back to the original medium and kept for 4 h in a normal incubator with 5% CO_2. Non-treated cells were maintained in a normal incubator with 5% CO_2 (normoxia).

After reperfusion, the media containing dead cells as well as the 1X DPBS from washing were collected. Cells were trypsinized and suspension was centrifuged at 1500 rpm for 5 min. Then, cell pellet was lysed in RIPA buffer.

2.2.8. Neonatal ventricular myocytes purification

Neonatal rat ventricular myocytes (NRVMs) were isolated from newborn (1-2 days) Wistar rats. Hearts (11-15 pups) were collected in ice-cold CBFHH buffer (137 mM NaCl, 20 mM HEPES, 0.81 mM Mg_2SO_4, 0.44 mM K_2PO_4, 0.33 mM Na_2HPO_4, 5.6 mM glucose, 5.4 mM KCl, pH 7.3) and atria, blood vessels and tissues from other organs were existed. Minced ventricles were put into a 100 ml Erlenmeyer flask and NRVMs were purified by serial enzymatic digestions of tissue with 0.6 mg/ml

of collagenase Type II and 0.4 mg/ml pancreatin in CBFHH buffer shaking at 37°C. First digestion (20 min) was discarded. After the second (20 min), third (25 min), fourth (25 min) and fifth (15 min) digestions, the cell suspension was placed into 4 ml Premium FBS at 37°C. After all digestions, cells were centrifuged at 900 rpm for 5 min and the pellet was resuspended in 10 ml of high-glucose DMEM:M199 (4:1) supplemented with 10% Horse Serum, 5% Premium FBS and 1 μg/ml AraC. The suspension was passed through a 40 μm nylon filter and pre-plated for 90 min on a 10 cm plate at 37°C, to allowing the attachment of fibroblasts. The remaining cell suspension was collected, cardiomyocytes were counted automatically, and cell survival was determined by Trypan Blue exclusion. Then, NRVMs were seeded onto 1% gelatin-coated 96-well plates. After 24 h, media was changed, and cells were kept at 37°C and 5% CO_2 for 3 days, when a confluent monolayer of spontaneously beating myocytes was observed.

After pre-plating, primary cardiac fibroblasts were maintained with DMEM medium, supplemented with 10% FBS, 1% Penicillin/Streptomycin and 1% L-glutamine. After 48 h, cells were trypsinized and split 1:2 for 3 days allowing them to proliferate.

2.2.9. Cell death analysis by DAPI staining

The media containing dead cells as well as the 1X DPBS from washing were collected. Then, cells were trypsinized and suspension, including media and washing 1X DPBS, was centrifuged at 1500 rpm for 5 min. Supernatant was aspirated and cell pellet was resuspended in 300-500 μl 1X DPBS. Next, 3 μl of DAPI (10 ug/ml) was added and cell death was analysed by Gallios Flow Cytometer (Beckman Coulter) and FlowJo software.

2.2.10. Gene expression analysis by qRT-PCR

RNA extraction

Cells were washed twice with 1X PBS and resuspended in TRIzol (500 μl). Then, chloroform (100 μl) was added and tubes were centrifuged 15000 ×g for 10 min at RT. The fraction with less density was transferred into new tubes and samples were mixed with 70° ethanol (200 μl). The RNA was extracted using PureLink RNA mini kit. DNAse treatment was performed using on-column DNase treatment

following manufacturer's instructions.

cDNA synthesis

RNA samples were quantified using Nano Drop, and 1 µg was used for cDNA synthesis with SuperScript IV reverse transcriptase, RNAsin and random primers following manufacturer's instructions.

qRT-PCR

cDNA (25 ng) was mixed with 5.5 µl of SYBR green reagent and 0.25 µl of gene specific Fw and Rv primers in a 10 µl final volume. The plate was sealed, centrifuged for 1 min at 200 ×g and run as follows: 50°C for 2 min, 95°C for 10 min, 60° for 1 min, 40 cycles of denaturation at 95°C for 15 s, annealing and elongation at 60°C for 1min, and three final steps of 95°C for 15 s, 60°C for 1 min and 95°C for 15 s. Samples were analysed in triplicates.

Primers for H9c2 cells (Rattus Norvecigus) are shown in Table 6.

Table 6. Primers used in qRT-PCR

Gene	Fw sequence 5'-3'	Rv sequence 5'-3'
MAPK14	GCATCATGGCTGAGCTGTTG	TGTAGTTTCTTGCCTCATGGC
TAB1	CCTACTCTCACTAACCAGAGCC	AGGTGGAAGTGAGTGAGCCG
MKK3	GTGCGACTTTGGCATCAGTG	TTGATCCTCTCAGGGGCCAT
MKK4	GCCCAGCGGCGAGAAAAA	CCCTGCTTGTAGCTGTACTCC
MKK6	GTCTGGGCATCACCATGATTG	AACTTGTCCGCTGGGAGTTG

2.2.11. Cell viability assays

Cells were seeded in duplicates onto 96-well plates. Next day, the media was replaced and NC-p38i were added. Compounds were prepared by serial dilutions in 100% DMSO at 100X or 10X final concentration. Then, 1:100 or 1:10 dilutions (0.1 or 1% final DMSO) were performed in media to obtain the indicated concentrations.

Cell viability was determined after 24, 48 and 72 h using an MTT kit (Roche), by adding first 10 μl of reagent A to every well and 4 h later 100 μl of reagent B. Next day, absorbance was read at 570 nm using the spectrophotometer Epoch 2 (BioTek). Absorbance was proportional to the viable number of cells and values were normalized to the DMSO control.

2.2.12. Colony formation assay

BBL358 cells (Canovas et al., 2018) were trypsinized, counted and plated in 60 mm plates. After 24h, cells were treated with NC-p38i and p38α ATP-competitive inhibitors. Media and compounds were replaced every 2-3 days. After 10 days, when colonies were visible, cells were fixed with 4% PFA for 15 min at RT. Plates were washed with water, stained for 10 min with crystal violet, and finally wells washed again with water. Images of the colonies were quantified by using Fiji software.

2.2.13. Doxorubicin-induced toxicity in human iPSC-CM

Doxorubicin-induced toxicity in human iPSC-derived cardiomyocytes (hiPSC-CM) experiments were performed by NCardia as indicated in the following protocol.

hiPSC-CMs were seeded on fibronectin-coated CardioExcyte 96-well plates. Cell media was changed every 48h. After 7 days, cells were treated with doxorubicin (1 and 10 μM) and NC-p38i compounds for 72h. Cell responses, including viability, contractility and electrophysiology, were evaluated in parallel by cell-induced electrical impedance and MEA (microelectrode array) technology using the xCELLigence RTCA CardioECR instrument at 4, 24, 48 and 72 h. Cardiac Troponin I release was also evaluated at 48 and 72h.

2.3. ADME-Tox assays

2.3.1. Kinase selectivity panel

NC-p38i compounds were tested in a panel of 97 human kinases using the Z´-LYTE technology by ThermoFisher. The assay is based on the measurement of proteolytic cleavage of peptide substrates labelled with two fluorophores that produce FRET signal. In the primary reaction, the active kinase phosphorylates a synthetic substrate FRET-peptide. In the secondary reaction, a site-specific

protease recognizes and cleaves non-phosphorylated FRET-peptides, thereby disrupting FRET signal between the donor and acceptor fluorophores. In this assay, peptide phosphorylation inhibits its cleavage. To quantify the reaction progress and correlate it with the inhibitory effect of NC-p38i, the Emission ratio between donor emission and acceptor emission after excitation of the donor fluorophore at 400 nm was calculated. The Emission ratio remains low if there is low kinase inhibition (FRET-peptide phosphorylation), whereas it is high if the kinase is inhibited (no phosphorylation of FRET-peptides).

2.3.2. Permeability in Caco-2 cells *in vitro*

The apparent permeability (Papp) for NC-p38i compounds was tested in Caco-2 cells as a model to study transport across the intestinal barrier. This experiment was performed by Draconis.

Caco-2 cells were grown as monolayers for 21 days in 96-well plates. NC-p38i were assayed in triplicates in HBSS-HEPES buffer pH 7.4 and added to the donor side, while the receiver side was filled only with HBSS-HEPES buffer pH 7.4. TEER and Lucifer yellow assay were used as markers of integrity of the cell monolayer. After incubation for 2 h at 37ºC, media was removed from the receiver side and samples were analysed by HPLC-MS to calculate the Papp values. Metoprolol was used as reference compound.

2.3.3. *In vitro* metabolic stability in human and rat liver microsomes

The *in vitro* metabolic stability of NC-p38i compounds was tested in human and rat liver microsomes by Cyprotex following this protocol.

Human and rat microsomes (0.5 mg protein/ml) were prepared in 0.1 M phosphate buffer pH 7.4 with NC-p38i compounds (1 μM and 0.25% final DMSO) and pre-incubated at 37 °C prior to the addition of NADPH (1 mM) to initiate the reaction.

A negative cofactor control was included for each compound tested where 0.1 M phosphate buffer pH 7.4 was added instead of NADPH. Two control compounds were included with each species. All incubations were performed singularly for each test compound at 0, 5, 15, 30 and 45 min. The negative control was incubated for 45 min only. The reactions were stopped by transferring into acetonitrile at the appropriate time points (1:3 ratio). The termination plates were centrifuged

for 20 min at 3000 rpm at 4 °C to precipitate the protein.

Following protein precipitation, the sample supernatants were combined in cassettes of up to 4 compounds, an internal standard was added, and samples were analysed using LC-MS/MS conditions. From a plot of ln peak area ratio (compound peak area/internal standard peak area) against time, the gradient of the line was determined. Subsequently, half-life and intrinsic clearance were calculated using the equations below:

- Elimination rate constant (k) = (- gradient)
- Half-life (t½, min) = 0.693/k
- Intrinsic clearance ($CL_{int,}$ µl/min/mg protein) = (V x 0.693)/t½; V = Incubation volume (µL)/Microsomal protein (mg)

2.3.4. Human hERG K^+ channel inhibition *in vitro*

The percentage of hERG K^+ channel inhibition of NC-p38i compounds was performed by Axxam Spa following this protocol.

CHO-hERG DUO cells were cultured in Ham's Nutrient Mixture F-12, supplemented with 10% FBS, 5% penicillin/streptomycin, G418 (1 ml of 50 mg/ml) and Hygromycine B (0.5 ml of 100 mg/ml) for 48 h before the experiment onto a T225 flask. Just before the experiment, cells were washed twice with DPBS and trypsinized. Then, cells were then re-suspended in 25 ml EX-CELL ACF CHO medium containing 0.25 ml of 100X Penicillin/Streptomycin and 0.1 ml of Soybean Trypsin Inhibitor 10 mg/ml and placed on the Qpatch 16X. NC-p38i compounds were tested at four concentrations starting from 10 µM with 1:5 dilution steps. (0.1% final DMSO). Verapamil was used as a reference agonist.

The following solutions were used for Patch clamp assay:

- Intracellular solution: 120 mM KCl, 5.37 mM $CaCl_2$, 1.75 mM $MgCl_2$, 10 mM EGTA, 10 mM HEPES, 4 mM Na_2-ATP (pH 7.2 adjusted with KOH).
- Extracellular solution: 145 mM NaCl, 4 mM KCl, 1 mM $MgCl_2$, 2 mM $CaCl_2$, 10 mM HEPES, 10 mM Glucose (pH 7.4 adjusted with NaOH).

Patch clamp experiments were sampled at 5 KHz. After establishment of the seal and the passage in the whole cell configuration, cells were held at -90 Mv and

the hERG current was performed by applying 200 ms step at -50 Mv; 2000 ms step at +20 Mv; 2000 ms step at -50 Mv; and back to -90 Mv; every 15 sec in the absence (vehicle period) and in the presence of increasing concentrations of the compounds.

The percentage of hERG K^+ channel inhibition NC-p38i compounds was assayed in duplicates. IC50 values indicated were only calculated when % inhibition was higher that 50% inhibition.

2.3.5. Plasmatic protein binding

The percentage of protein plasmatic binding was performed by Eurofins following the protocol below.

The protein matrix from human and rat plasma was spiked with NC-p38i compounds at 10 μM in duplicates (1% DMSO). The dialysate compartment of the plate was loaded with PBS (pH 7.4) and the sample side was loaded with equal volume of the spiked protein matrix. Then, the plate was sealed and incubated at 37 °C for 4 h. After the incubation, samples were taken from each compartment, diluted with the phosphate buffer followed by addition of acetonitrile and centrifugation. The supernatants were analysed by HPLC-MS/MS.

Acebutolol, quinidine, and warfarin were tested as reference compounds, which yield protein binding values that represent low, medium and high bindings to human plasma proteins, respectively. Additionally, control samples without dialysis were prepared from the spiked protein matrix, which served as basis for recovery determination.

The percent bound to proteins and the recovery were calculated using the equations below:

- Protein binding (%) = $[(Area_p - Area_b)/Area_p]*100$
- Recovery (%) = $[(Area_p - Area_b)/Area_c]*100$

$Area_p$, peak area of analyte in the protein matrix; $Area_b$, peak area of analyte in the assay buffer; $Area_c$, peak area of analyte in control sample.

2.4. *In vivo* experiments

2.4.1. Maximum tolerated dose in Zebrafish

The maximum tolerated dose of NC-p38i was tested in zebrafish embryos by Biobide following the protocol below.

Zebrafish embryos from BBD-T-010 at 3 hpf (hours post fertilization) were exposed to NC-p38i at different concentrations (10 embryos per condition, 5 embryos/well in a 24-well plate) for 72h at 28.5ºC. Control embryos were maintained in E3 media with 0.5% DMSO. Embryo lethality and developmental toxicity was evaluated using a stereoscope at the end of treatment.

2.4.2. Doxorubicin-induced cardiotoxicity in Zebrafish

A doxorubicin-induced cardiotoxicity study was performed by Biobide in zebrafish embryos following this protocol.

Zebrafish embryos from BBD-T-010 at 3 hpf (hours post fertilization) were exposed to doxorubicin (100 μM) in combination with NC-p38i at different concentrations (10 embryos per condition, 1 embryos/well in a 96-well plate) for 72h at 28.5ºC. Vehicle control embryos were maintained in E3 media with HEPES and 0.5% DMSO and positive control embryos were treated with doxorubicin alone. At the end of the treatment, embryos heart beat was counted during 15 s using a stereoscope and the presence of arrhythmia as well as the absence of heartbeat (death, fibrillation) was evaluated. Then, embryos were fixed, stained with ApopTtag In situ apoptosis detection kit (Millipore) and heart morphology was evaluated using Leica DMi8 inverted microscope (20X).

2.4.3. Maximum tolerated dose in rats

A maximum tolerated dose study was performed by Eurofins in male Sprague-Dawley rats following IV administrations of NC-p38i at 10, 30, 50, 65, 80 and 100 mg/kg.

NC-p38i compounds were formulated at 2, 6, 10, 13, 16 and 20 mg/ml in 10% DMA, 20% PG), 40% PEG 400 and 30% of 0.9% NaCl vehicle solution. A dosing volume of 5 ml/kg was applied through the lateral veins of the tail.

NC-p38i compounds were administered IV to animal cohorts of four Sprague-Dawley rats (2 males and 2 females). If animals survived for 72 h, the next cohort was tested with a higher dose. The testing stopped when all animals survived at the highest condition, or when all dose levels were tested. Full clinical examinations and animal death was analysed within 15 min, 1h and 72 h after dosing at each dose level.

Animal examination included a detailed analysis on the following profiles:

- Behavioural: body weight, alertness, passivity, stereotypy, vocalization, transfer reactivity, touch escape, tail-pinch, toe-pinch, pinna reflex, startle response, visual placing.

- Neurological: body elevation, limb position, tail elevation, limb tone, grip strength, body tone, abdominal tone, change in gait, catalepsy, righting reflex, twitches, convulsion.

- Autonomic: palpebral size, excretion (urination, diarrhoea), secretion (salivation, lacrimation), piloerection, body temperature, skin color, respiration, death.

2.4.4. Pharmacokinetic study in rats

A plasma pharmacokinetic study was performed by Eurofins in male Sprague-Dawley rats following IV administrations of NC-p38i at 30 mg/kg.

NC-p38i compounds were formulated at 6mg/ml in 10% DMA, 20% PG, 40% PEG 400, 30% of 0.9% NaCl. A dosing volume of 5 ml/kg was applied through the lateral veins of the tail. The plasma samples were collected at 3, 10, 30, 60, 120, 240, 360 and 1440 min post-treatment for each group of animals (3 rats/compound). The body weight of each animal was measured before dosing.

The exposure levels (ng/mL) of NC-p38i in plasma samples were then determined by LC-MS/MS. Then, plots of plasma concentrations versus time (mean ± SD) were constructed for each compound. The fundamental PK parameters (including $t_{1/2}$, C_0, AUC_{Inf}, MRT, V_{ss}, and CL) of each compound were obtained from the non-compartmental analysis (NCA) of the plasma data using WinNonlin.

2.5. Statistical analysis

Data are expressed as mean ± SD. Statistical analysis was performed by using a two-tailed Student's t-test for the comparison of two groups or ANOVA using Dunnet post-hoc correction for multiple groups using GraphPad Prism Software 9.0.0 (GraphPad Software, Inc., La Jolla CA). p-values are expressed as *P ≤ 0.05, **P ≤ 0.01 and ***P ≤ 0.001.

RESULTS

1. Identification of small molecules that inhibit p38α autophosphorylation

1.1. Screening for compounds that inhibit TAB1-induced p38α autophosphorylation

A computational strategy based on the combination of *in silico* virtual screening, docking and molecular dynamics techniques was applied to identify novel allosteric compounds that modulate the non-canonical activation of p38α. This work was performed by our collaborators Dr. Modesto Orozco (IRB Barcelona), Dr. Robert Soliva and Dr. Lucía Díaz (Nostrum Biodiscovery, NBD).

Given that many p38α interactors share the canonical docking site, we aimed to antagonize the non-canonical binding site using small molecules (Figure 9). First, a restrained high-throughput virtual screening (HTVS) aimed at mimicking the interaction between p38α and TAB1 (Figure 13) was run using Glide (version 6.1, Schrödinger, LLC, New York, NY, 2013) and the LEADS-LIKE-NOW database (2.419.472 compounds as of 2013-11-01). Then, the compounds were energetically ranked and a final selection of 35 compounds was made considering different criteria such as chemical structural diversity, drug-like properties, and favorable interactions.

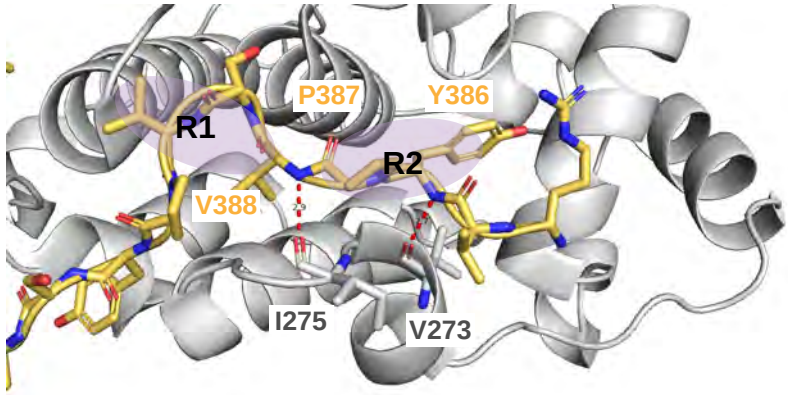

Figure 13. Constraints imposed for the high-throughput virtual screening with Glide. The restrained docking was run considering the key p38α-TAB1 interactions involving V273 and L275 residues and at least one of the two hydrophobic regions (R1 and R2, purple ellipsoids) on the non-canonical pocket of p38α. Dashed red lines represent the H-bonds that were sought to mimic by the screened compounds. p38α and TAB1 are coloured in grey and yellow, respectively (PDB:4LOO).

The 35 compounds were tested in an *in vitro* assay for TAB1-induced p38α autophosphorylation. We observed that recombinant non-phosphorylated

GST-p38α protein showed a basal autophosphorylation activity in the presence of ATP, which was enhanced by incubation with the $TAB1_{386-414}$ peptide (Figure 14A). We found that some compounds were able to inhibit TAB1-induced p38α autoactivation (Figure 14B), being compound 27 the most active one (Figure 14C).

Based on the chemical structure of compound 27, we selected commercially available analogues and ended up getting with 87 compounds, which were all tested *in vitro*. Exhaustive and detailed simulations were performed to design several analogues to complete SAR (structure-activity relationship) on the putative binding site. As a result, 46 additional compounds were synthesized and tested. Overall, only 23 out of the 133 tested compounds displayed greater than 80% inhibition of TAB1-induced p38α autophosphorylation (Figure 14D and Supplementary Figure 1). These biochemical studies allowed us to define the structural features associated with the compounds' ability to inhibit p38α autophosphorylation. We named the active compounds as NC-38i for non-canonical p38α inhibitors.

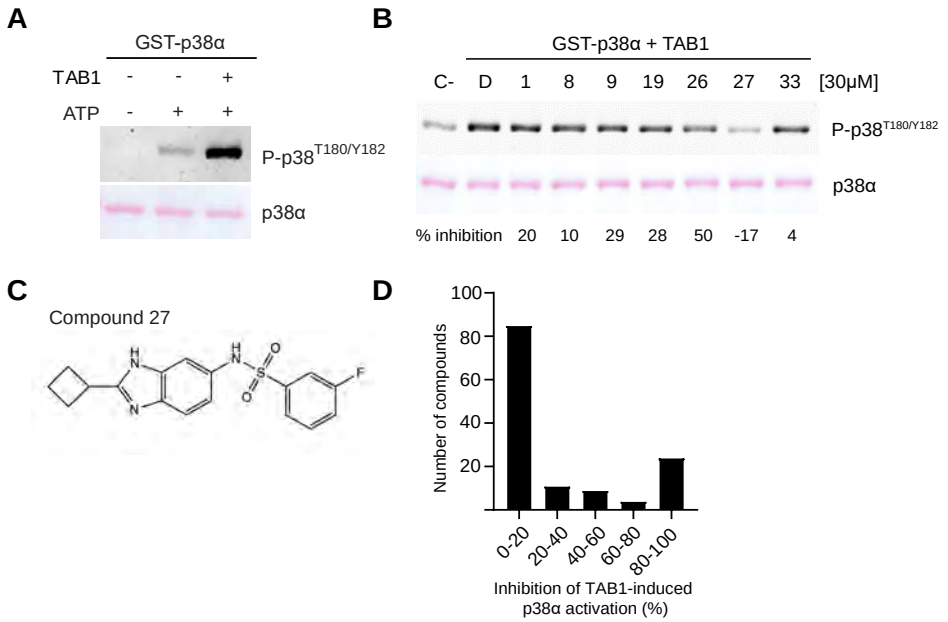

Figure 14. NC-p38i inhibit TAB1-induced p38α autophosphorylation *in vitro*. (**A**) Western blot of p38α autophosphorylation assays using recombinant non-phosphorylated GST-p38α (1,5 μM), $TAB1_{386-414}$ peptide (15 μM) and ATP (600 μM). (**B**) Western blot of TAB1-induced p38α autophosphorylation assays in the presence of the indicated compounds at 30 μM. C-, negative control containing GST-p38α and ATP. D, DMSO. Ponceau staining indicates total GST-p38α. (**C**) Structure of compound 27. (**D**) Histogram showing the inhibitory activity for the 133 compounds analysed at ≥10 μM in the TAB1-induced p38α autophosphorylation assay.

Next, we examined whether NC-p38i impaired non-canonical p38α activation in cells. Since previous results showed that co-transfection of TAB1 induces p38α autophosphorylation in cells (Ge et al., 2002), we co-transfected HEK293T cells with vectors encoding GFP-TAB1 or myc-p38α. Then, cells were treated with five of the most potent NC-p38i (Figure 15) and p38α phosphorylation was analysed by western blotting.

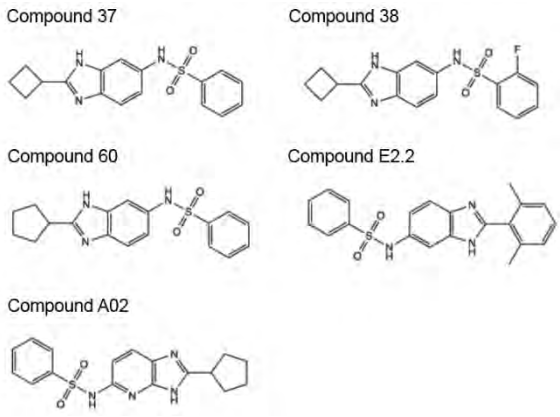

Figure 15. Structure of the most potent NC-p38i compounds *in vitro*.

As a control for p38α kinase activity inhibition, we used the ATP-competitor SB203580. We found that treatment with NC-p38i significantly decreased p38α phosphorylation levels as compared with cells treated with DMSO (Figure 16), supporting the results obtained in the *in vitro* autophosphorylation assays.

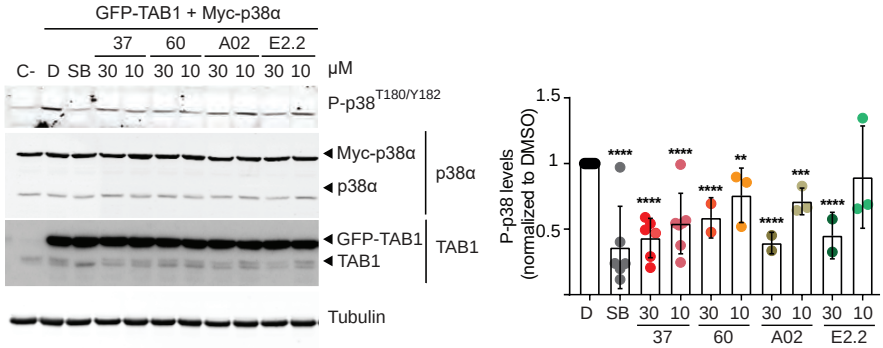

Figure 16. NC-p38i inhibit TAB1-induced p38α activation in cells. (**Left**) Western blot of HEK293T cells overexpressing GFP-TAB1 and myc-p38α and treated with the indicated NC-p38i compounds at 30 and 10 μM for 6 h. SB203580 was used at 10 μM. C-, HEK293T cells co-transfected with GFP and myc-p38α as negative control. D, DMSO used as the vehicle. (**Right**) Histogram showing the quantification of p38α phosphorylation levels normalized to the DMSO-treated cells. Data are shown as the mean ± SD normalized to DMSO-treated cells (n≥2 experiments).

1.2. NC-p38i also inhibit basal p38α autophosphorylation

Since GST-p38α possesses an intrinsic autophosphorylation activity independently of TAB1 (Figure 14A), we wondered whether it was inhibited by NC-p38i. We performed *in vitro* assays using non-phosphorylated recombinant GST-p38α in the presence of ATP and found that NC-p38i inhibited basal p38α autophosphorylation, thereby suggesting that NC-p38i might interfere with the p38α conformational change that triggers its autoactivation (Figure 17).

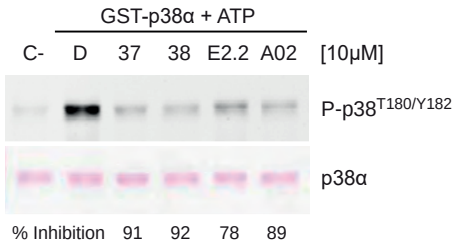

Figure 17. Effect of NC-p38i on basal p38α autophosphorylation activity. Western blot of GST-p38α *in vitro* autophosphorylation assays in the presence of the indicated NC-p38i compounds at 10 μM. C-, negative control containing GST-p38α without ATP. D, DMSO. Ponceau staining indicates total GST-p38α protein levels. Results are representative from n≥3.

1.3. NC-p38i do not interfere with canonical MAP2K-dependent p38α activation

Since NC-p38i inhibit p38α autophosphorylation, we examined whether they might also interfere with the canonical MAP2K-dependent p38α activation. *In vitro* kinase assays using recombinant MBP-MKK6^{DD}, which is a constitutively active form of MKK6 containing S207D and T221D mutations in the activation loop (Alonso et al., 2000), and GST-p38α showed that the NC-p38i did not affect canonical p38α phosphorylation by MKK6 (Figure 18A).

We also measured the effect of NC-p38i on the ability of MKK6-activated p38α to phosphorylate substrates. We performed *in vitro* kinase assays with active GST-p38α and either GST-MK2 or GST-ATF2 as substrates in presence of NC-p38i. We observed that NC-p38i at 10 μM weakly reduced the phosphorylation of MK2 an ATF2 compared with the ATP-competitive inhibitor PH797804 at 2 μM (Figure 18B and 18C).

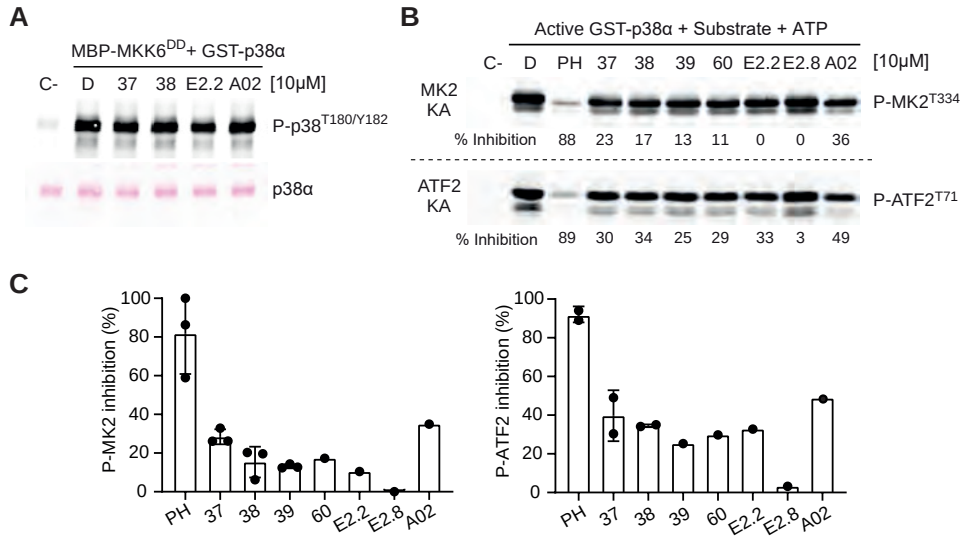

Figure 18. Effect of NC-p38i on canonical p38α activation and its kinase activity *in vitro*. Western blot of *in vitro* kinase assays showing the effect of the indicated NC-p38i compounds on (**A**) canonical MKK6-induced p38α phosphorylation and (**B**) GST-p38α kinase activity on the substrates GST-MK2 and GST-ATF2. The blots were developed with antibodies against the indicated phosphorylation sites. MBP-MKK6^{DD}, constitutively active MKK6. C-, negative control, GST-p38α in (A) and GST-MK2 or GST-ATF2 in (B). D, DMSO. PH, ATP-competitor PH797804. Ponceau staining indicates total GST-p38α levels. (**C**) Graphs showing the percentage of inhibition of GST-MK2 and GST-ATF2 by active GST-p38α incubated with NC-p38i at 10 μM or PH797804 at 2 μM. Results are shown as mean ± SD from n≥2 experiments.

Altogether, these results support the notion that NC-p38i may act as specific inhibitors of the non-canonical p38α activation mediated by autophosphorylation.

2. Characterization of the mechanism of action of NC-p38i

Since we found that NC-p38i can effectively inhibit p38α autophosphorylation both *in vitro* and in cells, we sought to determine their mechanism of action.

2.1. NC-p38i form a transient and fast complex with p38α

The efficacy of drugs is usually related with the lifetime of the ligand-protein complex (Lu and Tonge, 2010; Tonge, 2018).

As a first approach to monitor the binding between NC-p38i and p38α, we performed Surface Plasmon Resonance (SPR) assays. SPR technology allows to measure the affinity and kinetics for ligands to an immobilized target protein, including the equilibrium binding affinity constant (K_D) and the rates of association (k_a) and dissociation (k_d) (Renaud et al 2016).

Previous SPR studies analysing the binding of p38α inhibitors to its ATP-site were performed with the p38α protein immobilized through amine coupling chemistry (Casper et al., 2004; Thurmond et al., 2001). We considered that this strategy might induce random conformational changes in p38α that could impair proper binding of allosteric NC-p38i compounds. Consequently, we used biotin-streptavidin binding to favour the exposure of the non-canonical binding site of p38α (Hutsell et al., 2010; Papalia et al., 2008).

First, biotin-labelled non-phosphorylated p38α was homogeneously immobilized on the chip and SB203580 was tested as a positive control (Casper et al., 2004; Thurmond et al., 2001; Zhu et al., 2016). We observed dose-response sensograms (Figure 19A, upper panel) with a binding profile that allowed the instrument to calculate its associated K_D, as well as the k_a and k_d rates (Figure 19B).

NC-p38i also exhibited dose-dependent sensograms with a steady state plateau at all concentrations tested (Figure 19A, lower panel). These data indicated direct binding of NC-p38i to p38α and allowed the instrument to calculate a K_D for each compound. However, the compounds formed a very fast and transient complex with p38α that did not allow to measure NC-p38i kinetic parameters, as the values were out of the resolving power of the Biacore T200 instrument (Figure 19B). These results indicate a different mechanism of action for NC-p38i compared to an orthosteric ATP-competitive inhibitor.

It has been described that the phosphorylation state of p38α does not affect its binding to TAB1 (De Nicola et al., 2018). To evaluate whether p38α phosphorylation might interfere with NC-p38i binding, we performed *in vitro* kinase assays using recombinant MBP-MKK6^{DD} and biotinylated p38α. Then, we repeated the SPR experiment with phosphorylated p38α protein, and obtained sensograms and binding affinities that were comparable to the data obtained using non-phosphorylated p38α protein (Figure 19B). These results confirm that the activation state of p38α does not affect NC-p38i binding.

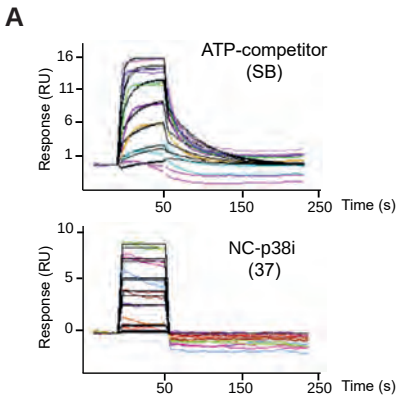

B

	Sample	K_D (μM)	k_a (1/Ms)	k_d (1/s)
ATP competitor	**SB***	0.036 (I) 0.016 (A)	5.76E+5 (I) 8.33E+5 (A)	2.09E-2 (I) 1.32E-2 (A)
NC-p38i	**37**	5.66 (I) 2.25 (A)	-	-
	60	2.29 (I) 1.82 (A)	-	-
	E2.2	4.10 (I) 9.65 (A)	-	-
	A02	9.19 (I) 4.24 (A)	-	-

Figure 19. SPR experiment showing NC-p38i binding to p38α protein. (**A**) Sensograms showing the binding of SB203580 and NC-p38i compound 37 at different concentrations (different colour lines) on biotinylated non-phosphorylated p38α. RU, response units. (**B**) Detailed binding analysis between NC-p38i and biotinylated p38α. The binding model 1:1 was used to perform binding analysis. The ATP-competitor SB203580 was used as a control. I, inactive, non-phosphorylated p38α; A, active, phosphorylated p38α; *SB203580 binding parameters were analysed by kinetics. K_D, binding affinity constant; k_a, association rate; k_d, dissociation rate.

2.2. NC-p38i compounds 37 and 38 inhibit simulated ischaemia-reperfusion induced cell death

As mentioned above, NC-p38i inhibit p38α activation induced by TAB1 overexpression in HEK293T cells (Figure 16). This non-canonical mechanism of p38α activation has been proposed to be relevant during myocardial ischaemia-reperfusion injury (IRI) and play an important role in triggering cardiomyocyte cell death *in vitro* and *in vivo* (Kumphune et al., 2012; Li et al., 2005a; Tanno et al., 2003; Wang et al., 2013). In this context, inhibition of non-canonical p38α activation was postulated to be therapeutically useful to reduce cardiomyocyte death upon IRI. Indeed, pharmacological inhibition of p38α with SB203580 has been reported to improve myocardial function (Clark et al., 2007; Kumphune et

al., 2015; Surinkaew et al., 2013).

We investigated whether NC-p38i could interfere with cardiomyocyte death in an *in vitro* model of ischaemia-reperfusion. We used the H9c2 rat cardiac myoblast cell line as a well-established cell culture model of simulated ischaemia-reperfusion (SIR) (Chen and Vunjak-Novakovic, 2018; Du et al., 2010). H9c2 cells treated for 2 h with simulated ischaemia (0,1% O_2) followed by 4 h of reperfusion (normoxia) underwent apoptotic cell death, as indicated by cleaved caspase-3 detection (Figure 20). As previously reported, we found that preincubation of H9c2 cells with SB203580 inhibited SIR-induced H9c2 cell death. Intriguingly, the ATP competitive inhibitor LY222880 was less potent than SB203580 at inhibiting SIR-induced H9c2 cell death. We also tested several NC-p38i and found that compounds 37 and 38 potently decreased cleaved caspase-3 levels in H9c2 cells, supporting that were able to inhibit SIR-triggered cell death, whereas compounds 60, E2.2 and A02 showed smaller effects.

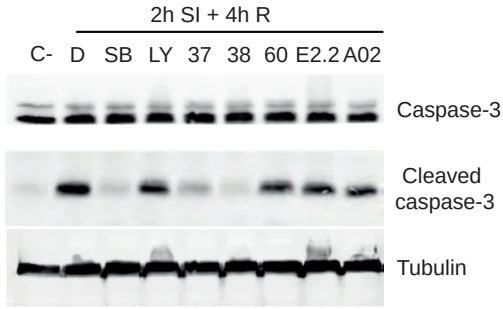

Figure 20. NC-p38i compounds 37 and 38 inhibit SIR-induced cell death. Western blot of H9c2 cells that were treated for 2 h with simulated ischaemia (0,1% O2, 5% CO2) followed by 4 h of reperfusion (normoxia) and incubated with ATP-competitive inhibitors SB203580 (10 μM) and LY2228820 (0.2 μM) or the indicated NC-p38i (30 μM). The compounds were added 24 h before and maintained during the treatments. Cleaved caspase-3 levels were quantified and normalized to DMSO-treated cells (D) to calculate the percentage of inhibition. Results are representative from n>3 experiments for compounds 37, 38 and 60, and n=1 for compounds E2.2 and A02.

Taken together, our results demonstrate that NC-p38i compounds 37 and 38 can protect H9c2 cells from SIR-induced damage. Therefore, we decided to focus on these two compounds to perform a detailed analysis of their mechanism of inhibition.

2.3. NC-p38i are allosteric inhibitors with low micromolar potencies

To determine the potency of NC-p38i compounds 37 and 38, we tested their ability to inhibit TAB1-induced p38α autophosphorylation *in vitro* at different concentrations. Our data showed that both compounds have IC50s within the low micromolar range for the inhibition of p38α autophosphorylation (Figure 21).

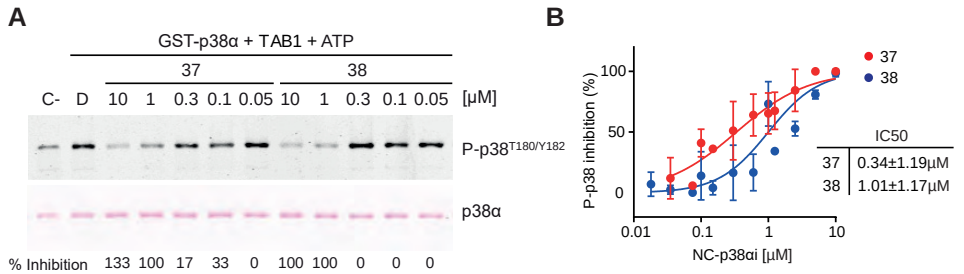

Figure 21. Dose-response inhibition of TAB1-induced p38α autophosphorylation by NC-p38i. (A) Western blots showing the percentage of p38α autophosphorylation that is inhibited by NC-p38i compounds at 0.05 to 10 μM in assays using non-phosphorylated GST-p38α, the peptide $TAB1_{386-414}$ and 600 μM ATP. Values were normalized to the phosphorylated p38α levels in the DMSO vehicle control (D). C-, negative control containing GST-p38α and ATP only. **(B)** Dose-response inhibition curves of TAB1-induced p38α autophosphorylation by compounds 37 and 38. Data were fitted using a nonlinear regression fit model (Graphpad Prism) to determine IC50s. Results are shown as mean ± SD from n>3 experiments.

The thermodynamic characterization of a ligand provides additional information beyond its binding affinity, on how the ligand associates with its target (Su and Xu 2018). Isothermal titration calorimetry (ITC) measures the heat flow of the ligand-target binding and determines the interaction thermodynamic parameters, such as enthalpy (ΔH), entropy (ΔS), the binding affinity constant (K_D) and the stoichiometry (n) of the reaction (Su and Xu 2018).

We performed ITC with NC-p38i compounds 37 and 38 and GST-p38α. The $TAB1_{386-414}$ peptide was used as a positive control for interaction with p38α. As previously described, $TAB1_{386-414}$ peptide was placed inside the sample cell and GST-p38α was serially injected from a syringe. In contrast, NC-p38i compounds were serially injected to the GST-p38α, which was placed inside the sample cell (DeNicola et al., 2013). In both cases, subsequent heat flow generated by binding was monitored.

ITC data showed significant heat changes upon $TAB1_{386-414}$ and NC-p38i binding to free GST-p38α (Figure 22). Results obtained with $TAB1_{386-414}$ were a bit lower

(n=0.528 and K_D=2.3 μM) but comparable to published data (n=0.8 and K_D=1.5 μM) (Figure 22, left) (de Nicola et al 2013). Indeed, we noticed that saturation of the system was rapidly reached, meaning that readjusting the concentrations of reagents would probably result in a better sigmoidal curve.

Importantly, the binding behaviour of NC-p38i appeared to be different from $TAB1_{386-414}$, as we observed flat curves that did not reach saturation (Figure 22, right). Lack of an inflection point did not allow to properly calculate stoichiometry and the associated thermodynamic parameters (Turnbull and Daranas, 2003). Therefore, NC-p38i thermodynamic parameters could not be conclusively estimated, and ITC was not considered suitable to measure binding of NC-p38i to p38α.

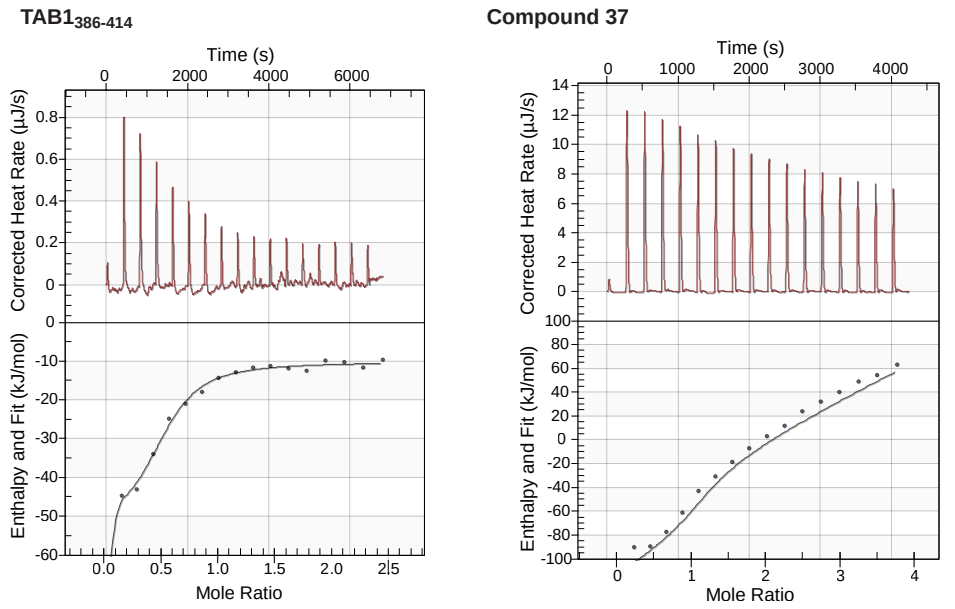

Figure 22. Characterization of NC-p38i interaction with p38α by ITC. ITC data for the interaction of $TAB1_{386-414}$ peptide (left) and compound 37 (right) to non-phosphorylated GST-p38α. Upper panels show the raw heat data from the titration of either GST-p38α into $TAB1_{386-414}$ or NC-p38i into GST-p38α. Lower panels show the integrated heat of injections, which was corrected for heats of dilutions and normalized to the molar amount of sample. Results from $TAB1_{386-414}$ represent n=1 experiment. Results for NC-p38i compounds 37 and 38 were similar and figure illustrate one of the n=2 experiments performed with compound 37.

In addition to SPR and ITC experiments, we performed fluorescent-based thermal shift assays (TSA) to further characterise the binding mechanism of

NC-p38i to p38α. In this assay, the inherent protein thermal stability is monitored by measuring its unfolding through SYPRO Orange dye fluorescence emission, which determines the protein melting temperature (T_m), when exposed to different ligands (Huynh and Partch, 2015; Lo et al., 2004). Importantly, it has been reported that T_m shift data can correlate with the IC50 values of kinase inhibitors. For example, an inhibitor that at 10 μM induces a ΔT_m of 4°C corresponds to a binding affinity <1 μM (Fedorov et al., 2007).

Graphical representation of non-phosphorylated GST-p38α protein denaturation revealed two distinct denaturation curves, which correspond to the unfolding of both p38α (first curve) and the GST tag (second curve) (Figure 23A).

As a positive control, we used the ATP competitive inhibitor SB203580. In agreement with published data, SB203580 strongly stabilized p38α (Casper et al., 2004; Shah et al., 2017), which was shown by a large shift of a single peak GST-p38α denaturation curve (ΔT_m at 10 μM = 13.35 ± 0.49 °C) (Figure 23). However, increasing concentrations of NC-p38i mildly stabilized p38α in a dose-dependent manner, as reflected by a moderate shift of the first portion of the GST-p38α curve (Figure 23A). We observed that compound 37 stabilized better p38α than compound 38 (ΔT_m at 10 μM = 2 ± 0.68 °C and 1.05 ± 0.74 °C, respectively) (Figure 23B).

Control experiments using GST protein were also performed to confirm the specificity of NC-p38i towards p38α, as the GST melting curves did not shift (Figure 23A).

Overall, the data from TSA highlight a different mechanism of action between high affinity (nanomolar range) orthosteric ATP binding inhibitors versus low affinity (low-micromolar range) allosteric NC-p38i compounds in terms of target protein stabilization.

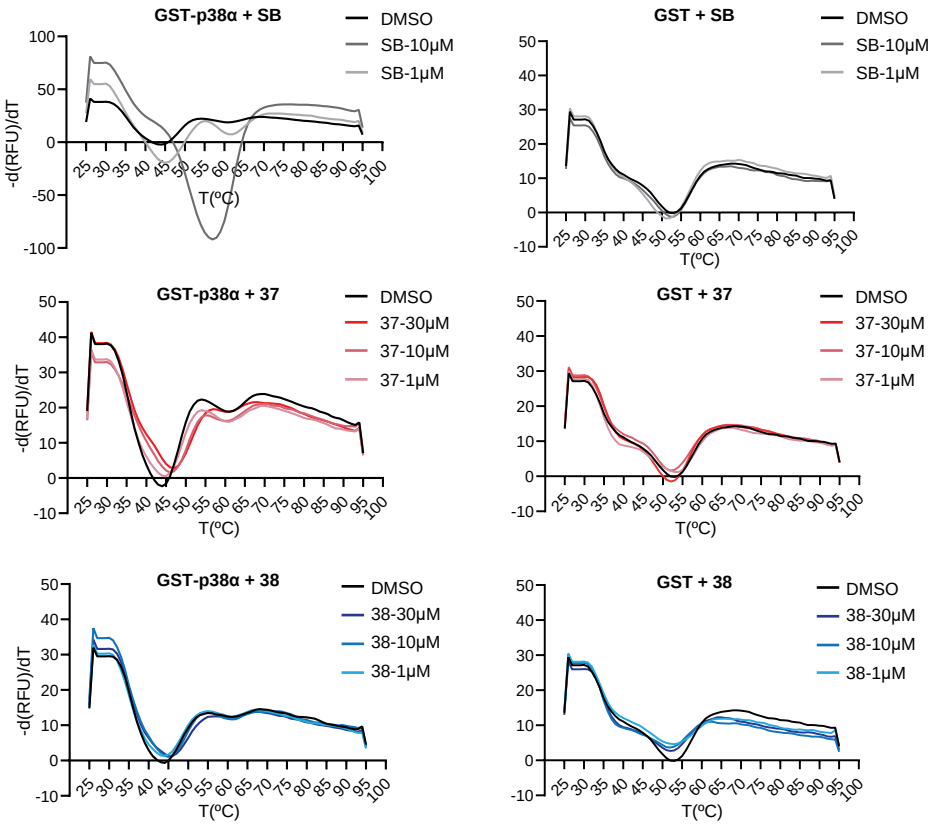

	[μM]	ΔTm (ºC)
SB	10	13.5 ± 0.7
	1	1.25 ± 1
37	30	3.44 ± 0.8
	10	1.9 ± 0.6
	1	0.25 ± 1
38	30	2.55 ± 1.2
	10	1.61 ± 1.1
	1	0.28 ± 1.1

Figure 23. NC-p38i increases thermal stability of p38α. (**A**) Representative denaturation curves of non-phosphorylated GST-p38α and GST proteins in the presence of SB203580 (SB) and NC-p38i compounds 37 and 38 at 30, 10 and 1 μM. DMSO was used as vehicle control. (**B**) Table indicating the ΔTm of GST-p38α upon binding to SB203580 or compounds 37 and 38 at the indicated concentrations (ΔTm = Tm inhibitor - Tm DMSO). SB203580 was used as a positive control for p38α stabilization. Results are shown as mean ± SD of n≥3 experiments done in triplicates.

2.4. NC-p38i do not interfere with TAB1 binding to p38α

NC-p38i inhibited p38α autophosphorylation induced by TAB1, presumably by binding to the non-canonical TAB1 binding site in p38α and directly competing with it. To examine whether NC-p38i compounds interfere with TAB1 binding to p38α, we used fluorescence polarization (FP) assays.

FP measures molecular interactions between a fluorescently labelled ligand and its target protein. Competition assays with non-labelled molecules allow to discover novel ligands for the same binding site, such as protein-protein interaction inhibitors (i.e. Bcl2 inhibitors) (Hall et al., 2016).

We used a $TAB1_{386-414}$ peptide N-terminally labelled with FITC that was incubated with increasing concentrations of non-phosphorylated GST-p38α and binding was monitored by measuring FP of FITC at different time points. We observed a dose-dependent increase in fluorescence 1 h after the addition of GST-p38α, which indicated the binding of FITC-$TAB1_{386-414}$ (K_D = 0.9889 ± 0.16 μM) (Figure 24A). To perform the following assays, we chose the GST-p38α concentration of 5.6 μM, which produced an 80% increase in FP. As a positive control, we used non-labelled $TAB1_{386-414}$ peptide for direct competition. We found that FITC-$TAB1_{386-414}$ was displaced by increasing concentrations of unlabelled $TAB1_{386-414}$ up to 1.5 μM (Figure 24B). Unexpectedly, we observed an increase in the fluorescence after adding 3.125 μM of $TAB1_{386-414}$, which could be due to peptide precipitation that causes light scattering interference with FP measurements (Moerke, 2009).

Next, the compounds 37 and 38 were incubated at increasing concentrations (0.75 to 100 μM) with FITC- $TAB1_{386-414}$ and GST-p38α. However, we found that neither compound 37 nor 38 decreased the FP signal, indicating that NC-p38i compounds do not interfere with the interaction between TAB1 and p38α (Figure 24C).

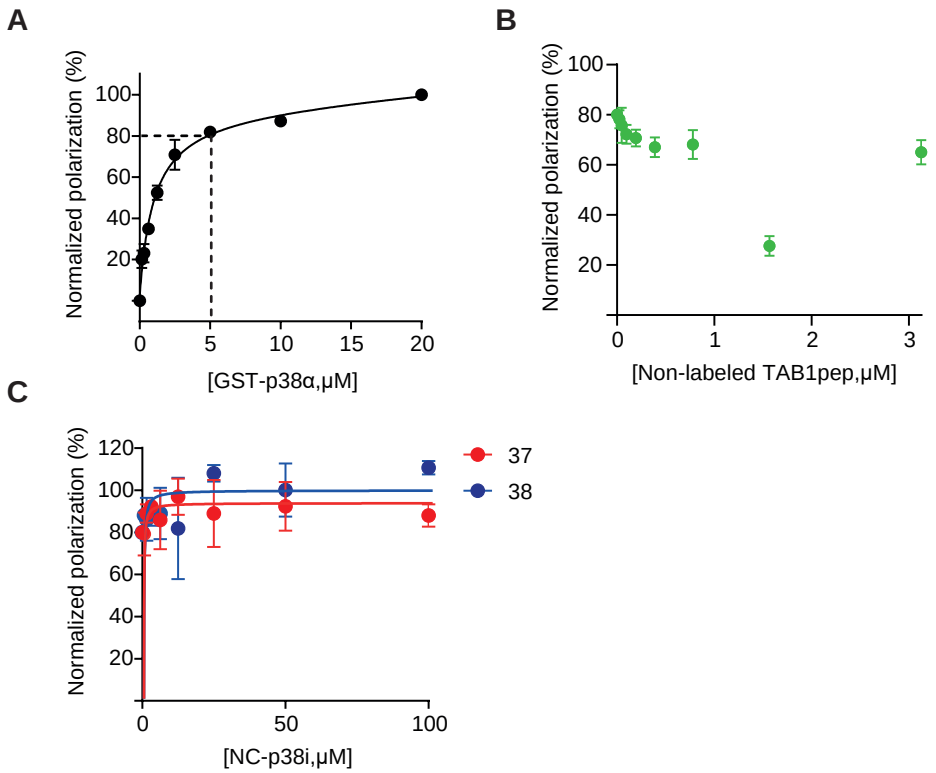

Figure 24. NC-p38i do not affect the interaction between TAB1 and p38α *in vitro*. (**A**) FITC-$TAB1_{386-414}$ peptide (10 nM) was incubated with increasing concentrations of non-phosphorylated GST-p38α for 1 h, and binding was monitored using a fluorescence polarization (FP) assay. Values were normalized as the percent of FP signal, and data were fitted using a nonlinear regression fit single site-binding model (Graphpad Prism) to determine K_D. Results are shown as mean ± SD of n=1 done in triplicates. (**B, C**) FITC-$TAB1_{386-414}$ peptide (10 nM) and non-phosphorylated GST-p38α (5.6 μM) were incubated with increasing concentrations of (**B**) non-labelled $TAB1_{386-414}$ peptide (0.024-100 μM) or (**C**) compounds 37 and 38 (0.75-100 μM) for 1 h. Binding of the compounds to GST-p38α was monitored using a FP assay as in (A). Results are shown as mean ± SD of n=1 done in triplicates for non-labelled $TAB1_{386-414}$ peptide and as mean ± SD of n=2-3 experiments done in triplicates for compounds 37 and 38.

Whereas TAB1 binds to p38α in a bipartite manner, NC-p38i were designed to bind only to the non-canonical binding site of p38α. Since our results showed that NC-p38i do not compete with TAB1, we wondered whether both ligands could bind simultaneously to p38α.

To address this possibility, we performed TSA and measured the T_m of GST-p38α incubated with NC-p38i alone or in combination with the $TAB1_{386-414}$ peptide. As expected, $TAB1_{386-414}$ increased the GST-p38α stability. Surprisingly, the

combination of NC-p38i and TAB1$_{386-414}$ significantly increased the T_m of GST-p38α compared to the NC-p38i alone (Figure 25). These observations indicate an additive effect of both ligands, thereby suggesting that NC-p38i and TAB1 might have independent binding sites p38α.

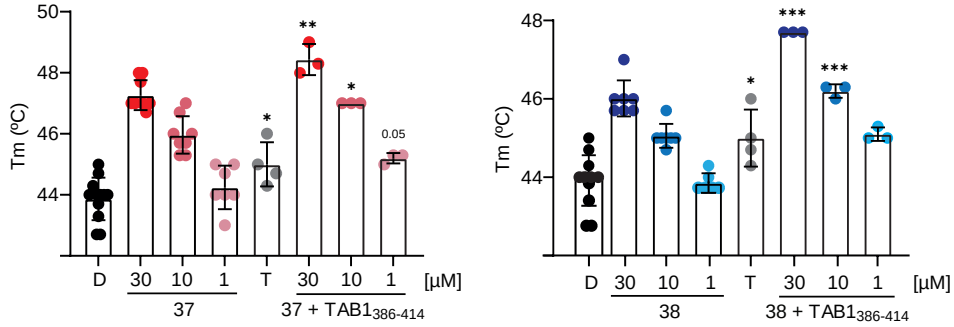

Figure 25. NC-p38i and TAB1 can bind simultaneously to p38α. Histograms showing the T_m of non-phosphorylated GST-p38α upon binding to compounds 37 (left) and 38 (right) alone or in combination with the TAB1$_{386-414}$ peptide (15 μM). Results are shown as mean ± SD of n≥3 experiments done in triplicates. Unpaired t-test was used to compare the T_m of GST-p38α incubated with TAB1$_{386-414}$ versus DMSO control, and NC-p38i alone versus NC-p38i combined with TAB1$_{386-414}$. D, DMSO. T, TAB1$_{386-414}$ peptide.

To further investigate whether NC-p38i might impair the TAB1-p38α interaction in cells, we performed proximity ligation assays (PLA). U2OS cells were co-transfected with GFP-TAB1 and Myc-p38α, treated with NC-p38i compounds and analysed by immunofluorescence and PLA.

Although cells transfected only with GFP-TAB1 showed some unspecific PLA signal, co-transfection with Myc-p38α significantly increased the PLA signal in cells, supporting that both proteins interacted (Figure 26A). We performed two independent experiments. We observed that treatment with NC-p38i decreased the PLA signal of co-transfected cells in the first experiment, but this result was not so clear in the second experiment (Figure 26B). Of note, the percentage of PLA positive cells was very low. (Figure 26C). Another technical problem was the low co-transfection efficiency, as GFP-TAB1 was expressed at lower levels compared to myc-p38α (Figure 26D). Taken together, the PLA results did not allow us to validate the effect NC-p38i on the interaction between TAB1 and p38α in cells.

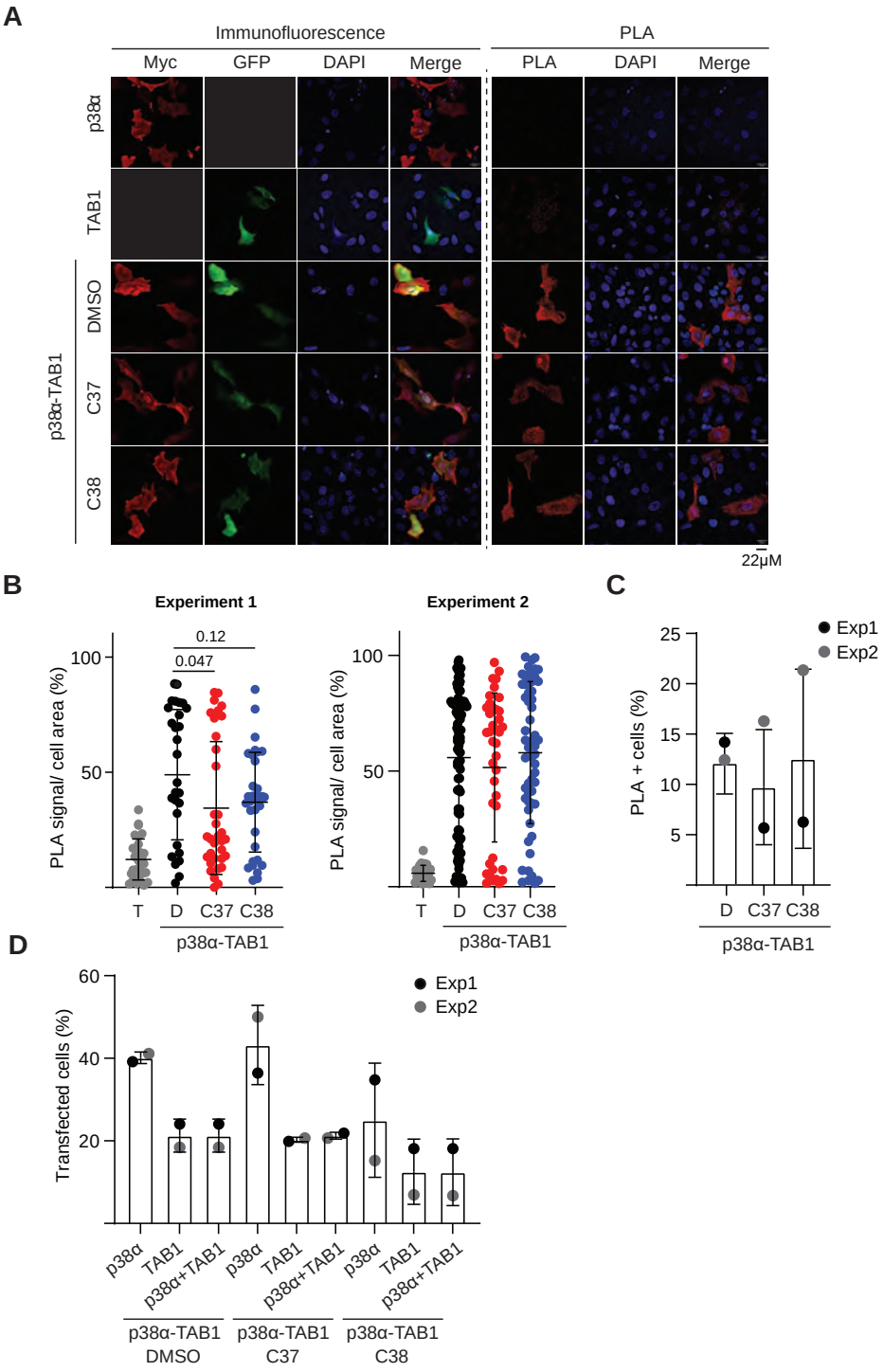
A
Immunofluorescence
PLA
Myc
GFP
DAPI
Merge
PLA
DAPI
Merge
p38α
TAB1
p38α-TAB1
DMSO
C37
C38
22μM
B
Experiment 1
Experiment 2
PLA signal/ cell area (%)
0.12
0.047
T
D
C37
C38
p38α-TAB1
C
PLA + cells (%)
Exp1
Exp2
D
Transfected cells (%)
p38α
TAB1
p38α+TAB1
p38α-TAB1
DMSO
C37
C38

Figure 26. PLA experiment showing the effect of NC-p38i on the TAB1-p38α interaction in cells. (**A**) Representative immunofluorescence (Left) and PLA (Right) images of U2OS cells transfected with GFP-TAB1 and/or Myc-p38α and then treated with compounds 37 and 38 (30 μM) for 6 h. DMSO was used as vehicle control treatment. Scale bar = 22 μm. (**B**) Quantification of PLA signal per cell area in two independent experiments. The percentage of PLA signal per cell area was plotted for all PLA positive cells in each case. Each dot represents an individual cell. Results are shown as mean ± SD. T, TAB1 alone; D, DMSO. (**C**) Quantification of the percentage of PLA^+ cells in each case. Results are shown as mean ± SD of n=2 experiments. (**D**) Quantification of the percentage of co-transfected cells overexpressing either myc-p38α, GFP-TAB1 or both, as determined by immunofluorescence. Results are shown as mean ± SD of n=2 experiments. Exp, experiment.

2.5. Structural characterization of NC-p38i binding to p38α

Our FP and TSA results were not consistent with the hypothesis that NC-p38i compounds bind to the non-canonical pocket of p38α. To elucidate the binding site of NC-p38i, we performed nuclear magnetic resonance (NMR) spectroscopy and X-ray crystallography experiments in collaboration with Dr. Maria Macías Lab and Dr. Joan Pous (IRB Barcelona). These techniques provide detailed information of the p38α structure at the amino acid level, and their combination reveals potential structural rearrangements, dynamics and high-resolution interactions induced by binding of different ligands. Similar studies have been performed in the past using the wild-type and mutated p38α proteins (DeNicola et al., 2013; Francis et al., 2011; Nielsen and Schwalbe, 2011; Vogtherr et al., 2006).

We performed two-dimensional (2D) $^{1}H,^{15}N$-TROSY-based titration experiments (Pervushin et al., 1997) to identify the residues potentially involved in the interaction between NC-p38i and p38α in solution. For this purpose, p38α was expressed in *E. Coli* using ^{2}H and ^{15}N labelled minimal medium. Next, a 2D $^{1}H,^{15}N$-TROSY spectrum of free [$^{2}H,^{15}N$]p38α was acquired and the signal was compared to the previously published data (DeNicola et al., 2013). We observed a great dispersion of the protein (Figure 27, green spectrum), indicating a well-folded p38α with a proper tertiary structure. The similarity of the amide resonances allowed us to use the published protein assignment.

As a positive control of the functional protein, we tested the binding of the $TAB1_{386-414}$ peptide to p38α. In this experiment, [$^{2}H,^{15}N$]p38α was incubated with unlabelled $TAB1_{386-414}$ (1:2). The chemical shift changes introduced upon binding were similar to those described in the literature (DeNicola et al., 2013), thereby validating our experimental settings (Figure 27, orange spectrum).

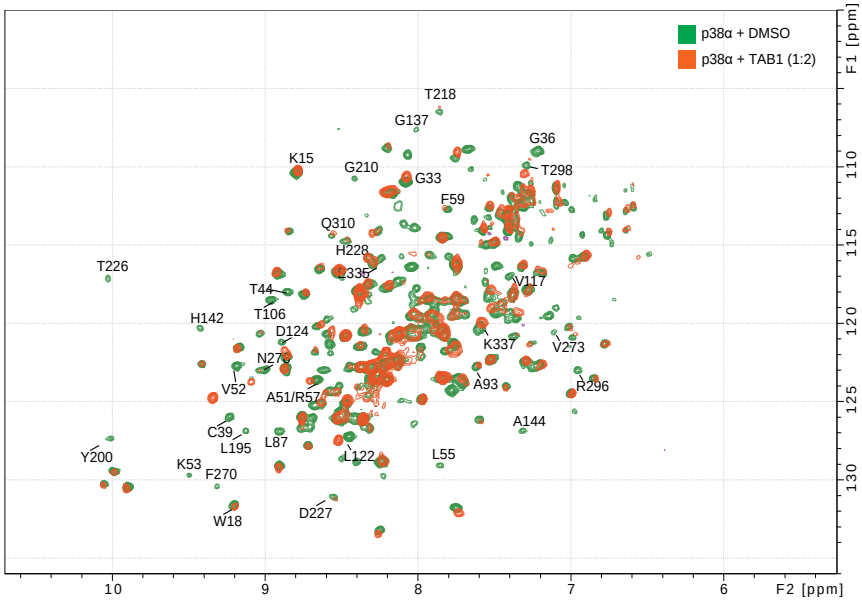

Figure 27. 2D $^{1}H,^{15}N$-TROSY of p38α in complex with TAB1$_{386-414}$. Overlay of 2D $^{1}H,^{15}N$-TROSY spectra of [$^{2}H,^{15}N$]p38α (green) and [$^{2}H,^{15}N$]p38α:TAB1$_{386-414}$ (1:2 ratio, orange). Acquisition time 3.25h. Unambiguously assigned residues affected by TAB1 binding are indicated.

Then, we tested the binding properties of NC-p38i compound 38 by NMR. Prior to perform the titration experiment, we measured the compound solubility in the protein buffer and found aggregation at concentrations higher than 0.5 mM (Figure 28). We acquired the 2D $^{1}H,^{15}N$-TROSY spectrum of labelled p38α with increasing amounts of compound 38 without exceeding the solubility limit (1:5). Substantial chemical shift changes were observed on p38α, many of which were similar to those induced by TAB1. However, we also observed changes that were not detected upon incubation with TAB1. These results suggested that the compound 38 could interact with a single site and induce allosteric changes of the protein backbone, or that it could bind at several locations (Figure 29).

TSA analysis suggested that NC-p38i and TAB1$_{386-414}$ could bind simultaneously to p38α (Figure 25). Thus, we decided to explore whether NMR also detected these interactions when both ligands were added to the protein solution. The TROSY spectrum of the mixture (Figure 30A) revealed similar alterations to those observed with each ligand separately (Figures 27 and 29). Of note, chemical shift changes that affect the amino acids E19, R23, S28, S32, T91 and A299, as well as others indicated with circles that could not be assigned, seem specific for compound 38 binding. These results suggest that compound 38 might bind to

the N-terminal domain (Figure 30B).

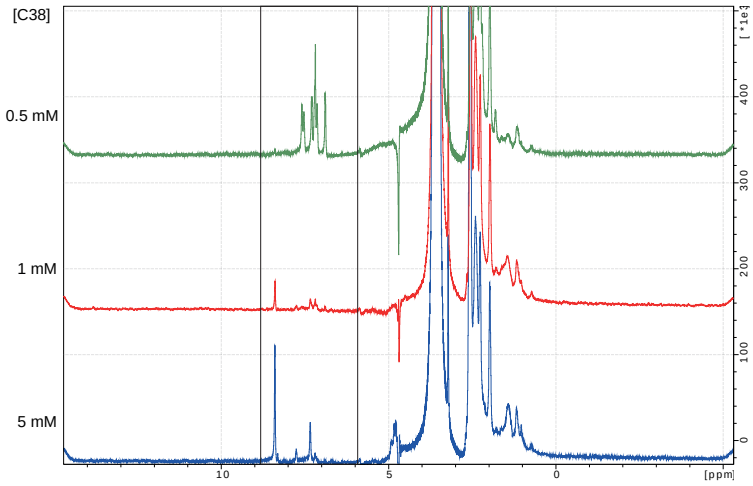

Figure 28. Solubility test of compound 38. NMR spectra of compound 38 (0.5-5 mM) diluted in buffer containing 20 mM Tris pH 7.5, 100 mM NaCl, 2 mM TCEP and 10 mM $MgCl_2$. The rectangle highlights the peaks corresponding to the compound.

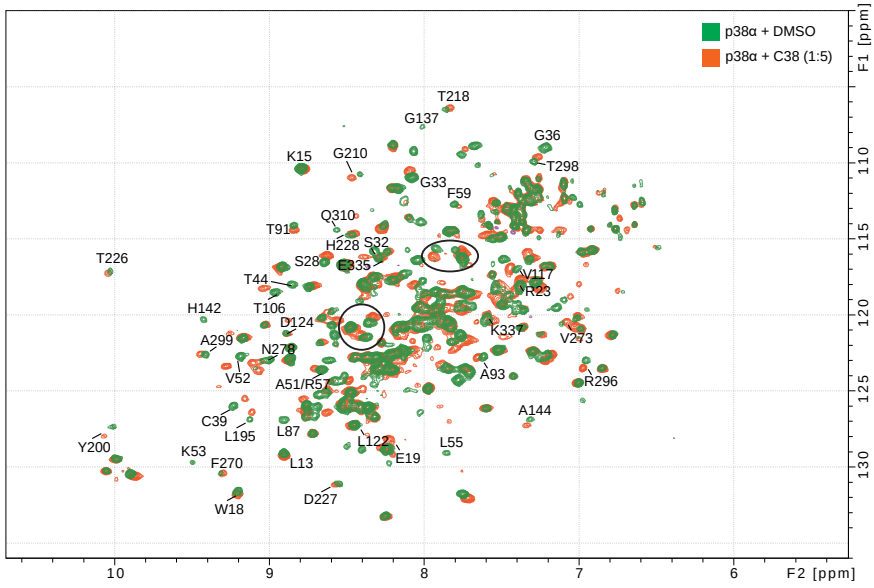

Figure 29. 2D [^{1}H-^{15}N] TROSY of p38α in complex with compound 38. Overlay of 2D ^{1}H,^{15}N-TROSY spectra of p38α (green) and p38α:C38 (1:5 ratio, orange). Acquisition time 3.25h. Unambiguously assigned residues affected upon binding are indicated. Circles indicate chemical shifts that could not be assigned.

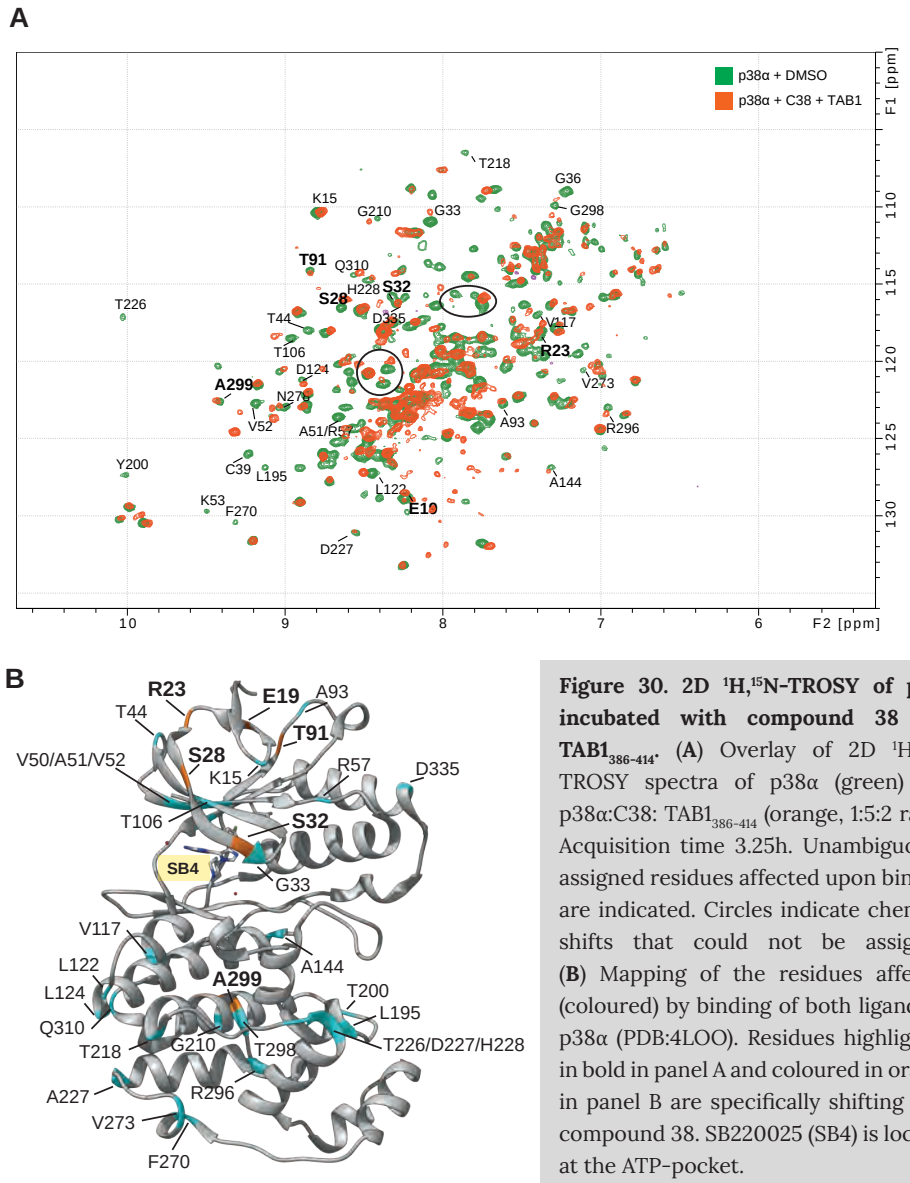

Figure 30. 2D $^{1}H,^{15}N$-TROSY of p38α incubated with compound 38 and TAB1$_{386-414}$. (**A**) Overlay of 2D $^{1}H,^{15}N$-TROSY spectra of p38α (green) and p38α:C38: TAB1$_{386-414}$ (orange, 1:5:2 ratio). Acquisition time 3.25h. Unambiguously assigned residues affected upon binding are indicated. Circles indicate chemical shifts that could not be assigned. (**B**) Mapping of the residues affected (coloured) by binding of both ligands to p38α (PDB:4LOO). Residues highlighted in bold in panel A and coloured in orange in panel B are specifically shifting with compound 38. SB220025 (SB4) is located at the ATP-pocket.

To obtain further structural insights into the NC-p38i mechanism of action, we attempted to determine co-crystal structures of the NC-p38i- p38α complex (Lee et al., 2006). In these experiments, the type-I inhibitor SB203580 was used to stabilize the kinase structure and facilitate the crystallization process through binding to the ATP-site of p38α (Pav et al., 1997).

We set up a co-crystallization screening using non-phosphorylated p38α mixed with SB203580 and different NC-p38i compounds and obtained crystals diffracting from 1.7 to 2.7 Å resolution. The electron density data unveiled two different crystal structures: p38α:SB203580 (Figure 31A, 1.9 Å resolution) and p38α:SB203580:C37 complexes (Figure 31B, 2.2 Å resolution). Of note, compound 37 was added to the crystallization mixture in both cases, together with p38α and SB. Initial docking experiments predicted that NC-p38i compounds could interact with the non-canonical binding site region. However, compound 37 was unexpectedly found at the active pocket above the SB203580 inhibitor (Supplementary figure 2B).

Comparison of both structures revealed a similar conformation for the traceable regions, suggesting that the presence of the NC-p38i compound 37 during the crystallization might induce comparable changes (Figure 31C).

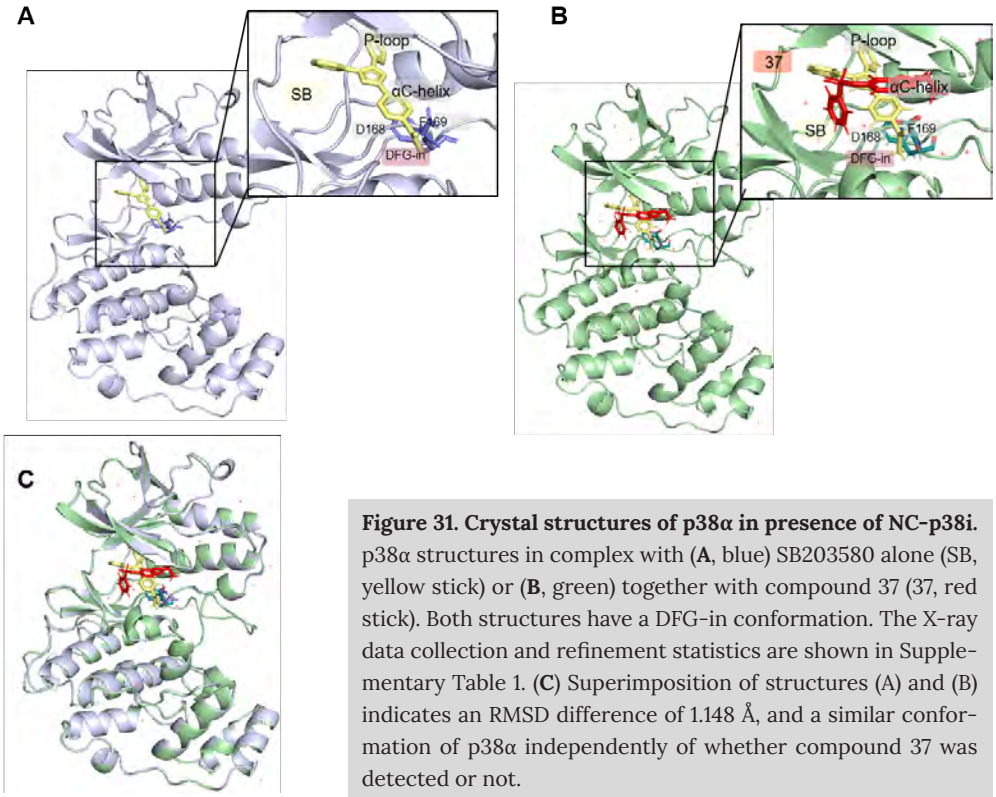

Figure 31. Crystal structures of p38α in presence of NC-p38i. p38α structures in complex with (**A**, blue) SB203580 alone (SB, yellow stick) or (**B**, green) together with compound 37 (37, red stick). Both structures have a DFG-in conformation. The X-ray data collection and refinement statistics are shown in Supplementary Table 1. (**C**) Superimposition of structures (A) and (B) indicates an RMSD difference of 1.148 Å, and a similar conformation of p38α independently of whether compound 37 was detected or not.

To address how NC-p38i could bind to the active site, we explored the residues from the ATP pocket and the P-loop in both structures. We noticed that Y35 displayed two different orientations. It is known that in presence of SB203580, Y35 orients

its aromatic ring towards the methylsulfinylphenyl ring of SB203580 (Wang et al., 1998). This "Y35-in" orientation was also observed in our p38α:SB203580 crystal (Figure 32A). Conversely, in the p38α:SB203580:C37 complex, there was not a strong electron density signal corresponding to the Y35 residue, indicating its high mobility (Supplementary Figure 2C and D). However, the "Y35-out" conformation appeared to be the most favourable (Figure 32B), suggesting that this movement might enable access of the compound 37 to the active site even if it is occupied by a ligand (Figure 32C). In addition, the compound 37 did not form any H-bond within this region, thereby corroborating the weak binding mode of NC-p38i.

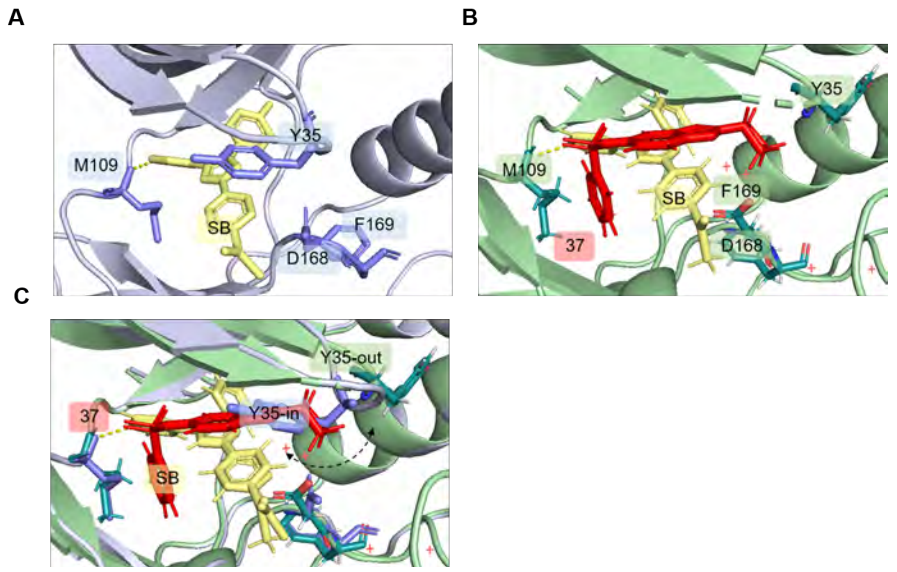

Figure 32. Y35 residue can adopt different conformations. (**A**) p38α:SB203580 structure containing Y35-in residue. (**B**) p38α:SB203580:37 complex showing a Y35-out conformation. Note that the P-loop of this structure lacks the A35 residue. SB203580, like ATP, forms a H-bond with M109 from the hinge in both structures (Wang et al., 1998). (**C**) Superimposition of both structures illustrating how Y35-in may restrict the accessibility of compound 37 at the active site.

Subsequently, we performed a comparative analysis with a p38α:SB203580 control structure (PDB 1A9U) to dissect the allosteric effects induced by NC-p38i. In agreement with our NMR data (Figure 29), the incubation with compound 37, either visible or not in the structure, produces notable rearrangements at different regions of p38α. At the N-terminal domain, the β1L0-β2L0 strands (L13, K15, W18, E19) (Figure 33A) and the P-loop (β1-β2 loop, G32-G36) (Figure 33B) bent down, thus displacing the SB203580 molecule 6.1 Å and the hinge 2.3 Å (M109) (Figure 33D). In the presented structures, the electron density signal of the

A-loop amino acids was partially observed. The strongest signal was observed in the p38α:SB203580:37 structure, allowing for the placement of some of the amino acid residues (Supplementary Figure 2E), and modelling others, such as T180 and Y182, with high degree of certainty (Figure 33C). Available data strongly suggests their displacement in comparison to the control p38α:SB203580 structure (PDB:1A9U).

Furthermore, displacements were also found at the C-terminal domain, including the canonical ED site (β7-β8 turn) (Figure 33E) and helix αD (Figure 33F), which exhibited a significant shift (6.7 Å), as well as helices αE, αF and αH (Figure 33G).

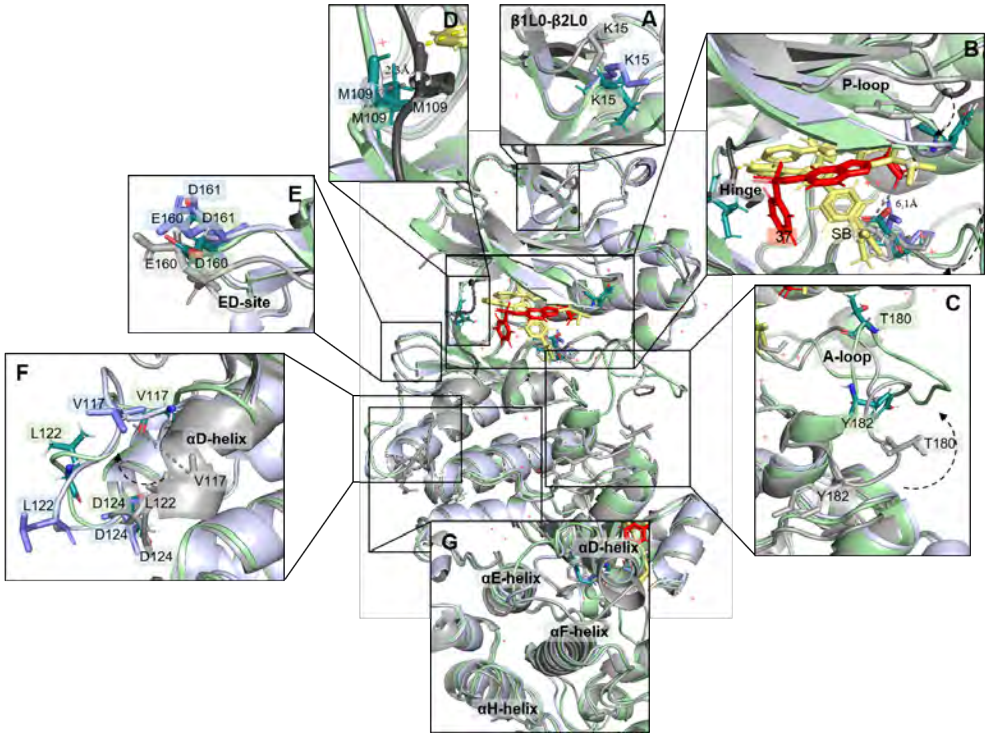

Figure 33. Overview of potential allosteric effects induced by compound 37 on p38α. Superimposition of p38α structures crystallized in presence of SB203580 and compound 37 with a p38α:SB203580 control complex (grey, PDB:1A9U) highlights the effects induced by NC-p38i binding on (**A**) β1L0-β2L0 strands, (**B**) P-loop, (**C**) A-loop, (**D**) hinge, (**E**) ED site, (**F**) αD-helix and (**G**) αE, αF and αH helices. SB203580 (SB, yellow sticks). Compound 37 (37, red stick). The RMSD difference of 1A9U structure aligned with p38α:SB (37 no visible, blue) and p38α:SB:37 (green) is 2.289 and 2.192 Å, respectively.

Given these observations, we next examined how NC-p38i could affect the conformational changes that TAB1 triggers on p38α. We noticed that compound 37 might interfere with the downward swing of P-loop (Figure 34A) and distort

the αD-helix position (Figure 34C), the correct positioning of C-terminal region of TAB1 at the canonical binding site without affecting its binding.

Collectively, these results demonstrate that NC-p38i binding to p38α may produce allosteric rearrangements that modulate its autoaphosphorylation capacity and catalytic activity.

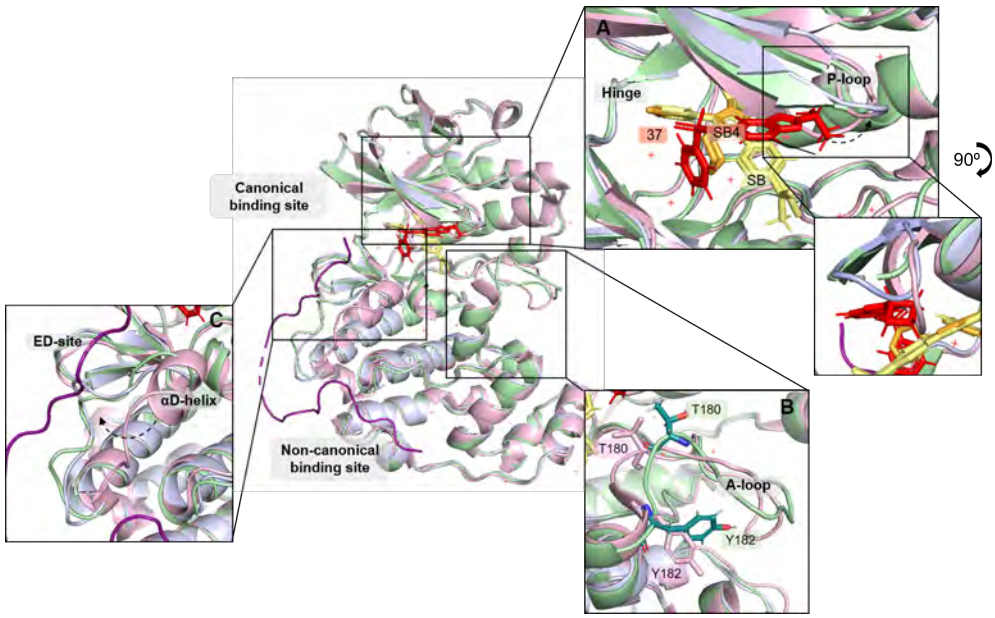

Figure 34. NC-p38i might impair the structural changes triggered by TAB1. Structural superimposition of p38α crystallized in the presence of compound 37 with a p38α:TAB1 structure (pink, PDB:4LOO) suggesting how NC-p38i might impair TAB1-induced p38α autoactivation (indicated with squares). The RMSD difference of 4LOO structure aligned with p38α:SB203580 (blue, C37 not visible) and p38α:SB203580:37 (green) is 1.843 and 1.543 Å, respectively. SB220025 (SB4, orange sticks). SB203580 (SB, yellow sticks). Compound 37 (37, red stick).

2.6. NC-p38i modulate ATP binding

In general, the potency of ATP-competitive kinase inhibitors greatly depends on the ATP concentration in the assay, so that increasing ATP levels will decrease the activity of the inhibitor. In contrast, allosteric inhibitors are less dependent on ATP levels (Knight and Shokat 2005). It has been reported that some allosteric compounds are also able to modify its active site (Leroux and Bondi 2020). In this case, the activity of these compounds might be affected by the assay conditions.

Crystallography data indicate that NC-p38i inhibit p38α autophosphorylation by inducing conformational changes that affect the ATP-pocket of the protein. Thus, we investigated whether the potency of NC-p38i was affected by the ATP concentration in the assay. We performed *in vitro* assays for both basal and TAB1-induced p38α autophosphorylation, and tested compounds 37 and 38 at different ATP concentrations. The IC50 values were calculated and compared with the potency determined at 600 μM ATP, being the standard concentration used for the *in vitro* autophosphorylation assays.

In basal p38α autoactivation assays, we observed that IC50s for both compounds remained stable at 100 and 600 μM ATP but increased at high concentrations of ATP (2000 μM) (Figure 35A). These data support that NC-p38i are not ATP-competitive inhibitors but they decrease the affinity for ATP by interfering with the spontaneously adopted p38α prone-to-autophosphorylate.

In contrast, this effect was not so clear in TAB1-induced p38α autoactivation assays (Figure 35B). Notably, TAB1 induces a conformational change in p38α that increases its affinity for ATP and enhances autophosphorylation (DeNicola et al., 2013). In these conditions, p38α might be less dependent on the levels of ATP and NC-p38i might impair the structural changes triggered by TAB1.

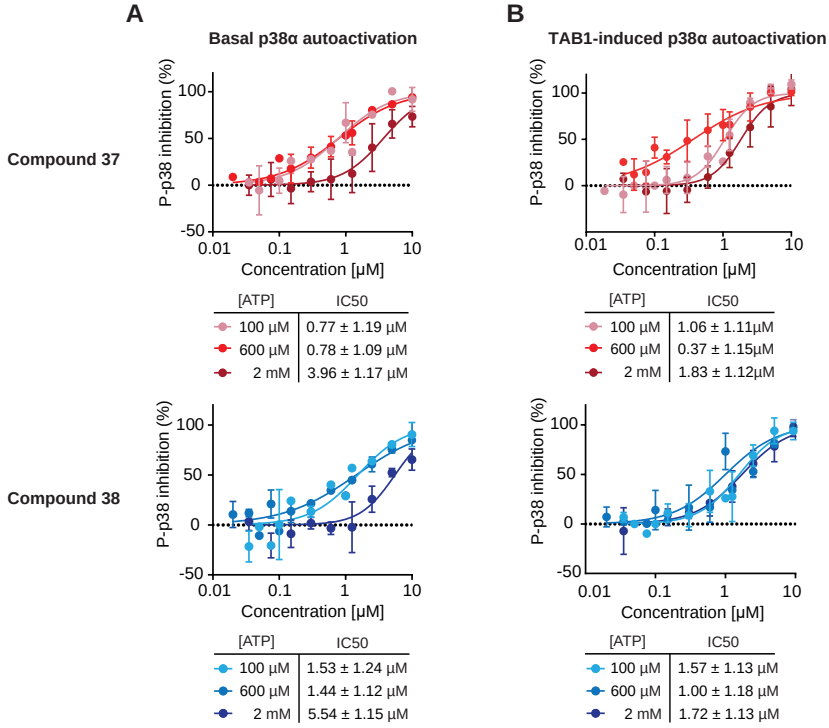

Figure 35. *In vitro* autophosphorylation assays at different concentrations of ATP. Dose-response inhibition curves of (**A**) basal and (**B**) TAB1-induced p38α autophosphorylation by compounds 37 and 38 (0.035 to 10 μM) at different ATP concentrations (100, 600 and 2000 μM). Data were fitted using a nonlinear regression fit model (Graphpad Prism) to determine IC50s. Results are shown as mean ± SD from n≥3 experiments.

To confirm these results, we performed NanoBRET kinase target engagement in HEK293T cells. This experiment is based on the emission of light (BRET) from the NLuc fusion protein when it is near an energy transfer probe that reversibly targets the kinase active site of the protein of interest. Changes in the BRET signal intensity reflect the binding of compounds to the kinase. Although this approach has been extensively used to test ATP-competitive inhibitors, it is also useful for certain allosteric compounds that induce rearrangements at the catalytic site of the kinase (Vasta et al., 2018) (Figure 36A).

For these assays, HEK293T cells were transfected with NLuc-p38α and incubated with a cell-permeable energy transfer probe, which generated a BRET signal in live cells. Then, cells were treated with the ATP-competitor VX-702, which that directly competed with the probe and efficiently decreased the BRET signal. Importantly, treatment with compound 37 was also able to lower the BRET signal in these cells but at higher concentrations (Figure 36B).

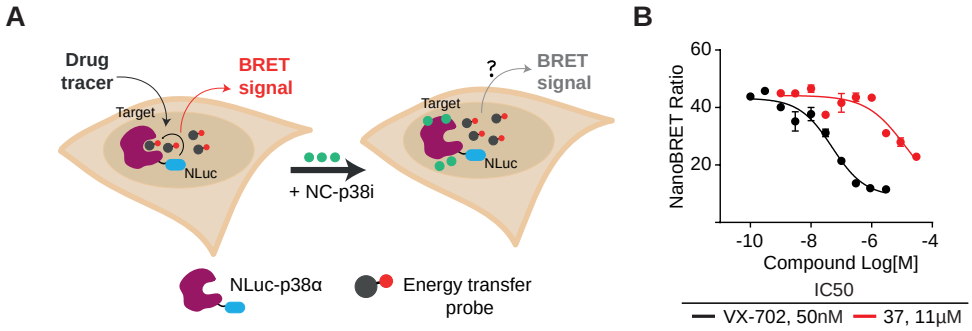

Figure 36. NC-p38i induce allosteric changes that affect the ATP-binding site. (**A**) Scheme showing the NanoBRET Target engagement experiment in HEK293T cells overexpressing NLuc-p38α and treated with NC-p38i. Adapted from Vasta et al. 2018. (**B**) Graph showing the effect of compound 37 in displacing the energy transfer probe from the ATP-binding site of p38α. The ATP-competitive inhibitor VX-702 was used as a positive control. NLuc, NanoLuc™ Luciferase. Results are shown as mean ± SD from n=1 experiment done in duplicates and are representative for 2 experiments.

These results validate that NC-p38i interaction with p38α induces changes in the ATP-site reducing its accessibility and thereby its affinity.

3. Assessment of the NC-p38i efficacy in models of non-canonical p38α activation-associated diseases

3.1. NC-p38i reduce SIR-induced cell death under prophylactic and therapeutic conditions

Non-canonical p38α activation induced by TAB1 has been proposed to trigger cardiomyocyte death upon myocardial ischaemia-reperfusion injury *in vitro* and *in vivo* (Kumphune et al., 2012; Li et al., 2005a; Tanno et al., 2003). Pharmacological inhibition of p38α with SB203580 either before or during ischaemia, but not during reperfusion, reduces heart damage by reducing myocardial cell death (Kumphune et al., 2015; Surinkaew et al., 2013). These results emphasize that the timing of p38α inhibition could be crucial to determine the efficacy of the treatment.

To evaluate the therapeutic potential of compounds 37 and 38 in this setting, H9c2 cells were treated with NC-p38i at different time points and subjected to *in vitro* SIR protocol. First, we observed that treatment with 10 μM SB203580 during ischaemia with or without cell pre-treatment reduced SIR-induced cell death, thereby recapitulating published data (Figure 37A). Similarly, treatment with compounds 37 and 38 during ischaemia reduced cell death in a concentration-dependent manner. In contrast, treatment with wither SB203580 or NC-p38i during reperfusion did not protect from cell death triggered by SIR (Figure 37A). These results suggest that NC-p38i compounds 37 and 38 have a cardioprotective effect both under prophylactic and therapeutic conditions when applied only during the ischemic insult.

Little is known about the substrates downstream of non-canonically activated p38α in response to myocardial ischaemia-reperfusion injury. TAB1 and HSP27 phosphorylation can be regulated by p38α, either directly (TAB1) or through MK2 (HSP27). Reduced phosphorylation of these two proteins has been correlated with both reduced myocardial infarct size and improved cardiac function *in vivo* (De Nicola et al., 2018; Jacquet et al., 2007; Kumphune et al., 2012; Kumphune et al., 2015; Surinkaew et al., 2013).

To investigate whether compounds 37 and 38 inhibited endogenous p38α autoactivation upon SIR, the phosphorylation levels of p38α pathway substrates were assessed in H9c2 cells after 2 h of simulated ischaemia followed by 15 min of reperfusion. We observed that while SB203580 strongly reduced both phospho-TAB1 and phospho-HSP27 levels, compounds 37 and 38 only partially reduced the phosphorylation of both proteins, with compound 37 having a

stronger effect that compound 38 (Figure 37B).

In contrast, we did not observe any differences in the p38α phosphorylation levels of SIR-stimulated H9c2 cells treated either with SB203580 or with NC-p38i. This observation could be accounted by the existence of feedback loop mechanisms that compensate for the inhibition of p38α autophosphorylation (De Nicola et al., 2018). To elucidate which MAP2K might contribute to this compensatory mechanism, we measured the mRNA levels of MKK3, MKK6 and MKK4 in H9c2 cells. We observed that MKK3 mRNA was highly expressed in H9c2 cells whereas MKK6 and MKK4 mRNAs were not detectable (Figure 37C). These data suggest that MKK3 might be responsible for p38α phosphorylation in these cells.

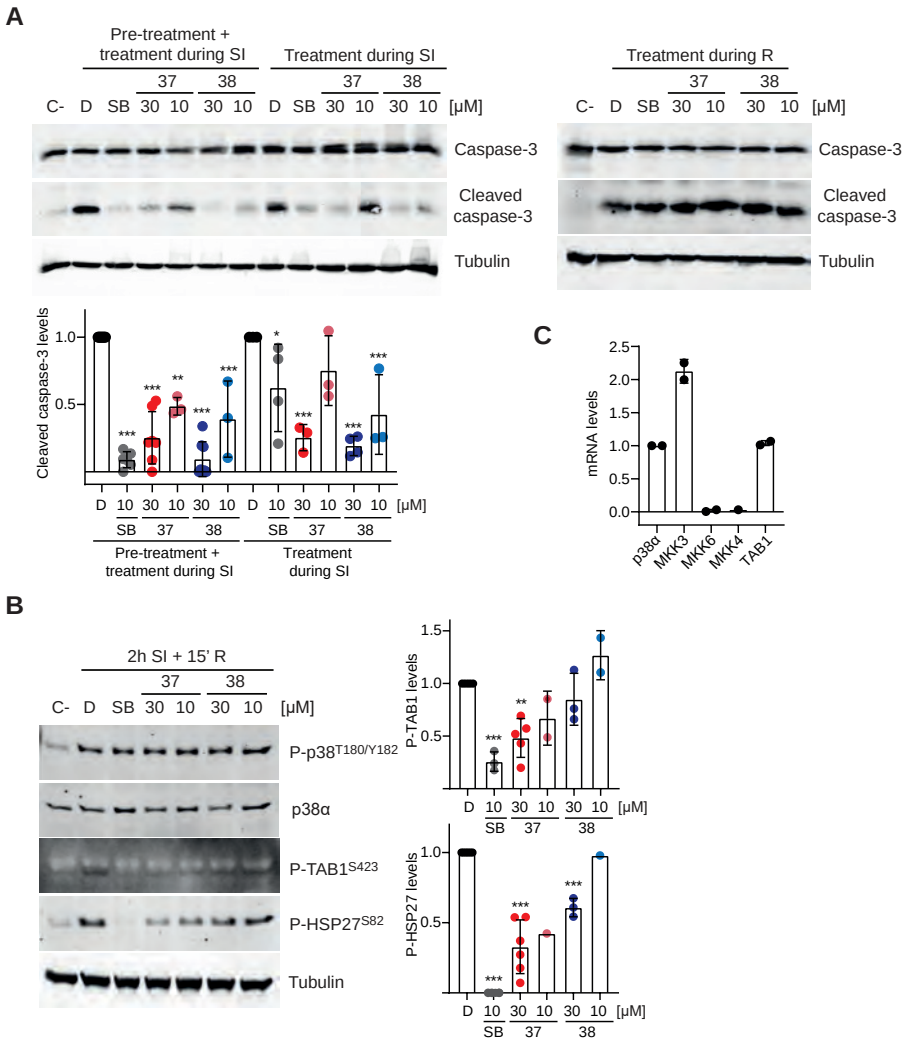

Figure 37. NC-p38i protect against SIR-induced death of H9c2 cells. (**A**) Western blot of H9c2 cells treated with SB203580 (SB, 10 μM) or compounds 37 and 38 (30 and 10 μM) for the indicated times and exposed for 2 h to simulated ischaemia (0,1% O2, 5% CO2) followed by 4 h of reperfusion (normoxia). Histogram shows the mean ± SD normalized to the DMSO-treated cells of n≥3 experiments. (**B**) Western blot of H9c2 cells pre-treated for 24 h and then treated with SB203580 (SB, 10 μM) or compounds 37 and 38 (30 and 10 μM) during 2 h of simulated ischaemia (0,1% O2, 5% CO2) followed by 15 min of reperfusion (normoxia). DMSO was used as vehicle control. Histograms show the mean ± SD normalized to the DMSO-treated cells of n≥2 experiments. (**C**) qRT-PCR analysis of MAPK14 (p38α), TAB1, MKK3, MKK4 and MKK6 mRNAs in H9c2 cells. Levels of mRNAs are referred to MAPK14 expression.

3.2. NC-p38i partially impair stress-induced p38α signalling

We observed that compounds 37 and 38 at 30 μM were able to decrease HSP27 phosphorylation in H9c2 cells stimulated with SIR. Therefore, we wondered whether NC-p38i could affect the stress-activated canonical p38α signalling pathway.

We selected three cell lines (H9c2, U2OS and BBL358), which were treated with the stress stimuli UV, anisomycin and NaCl (Figure 38A). The three stimuli were able to induce the activation of canonical p38α signalling in the three cell lines, as shown by the increased phosphorylation of MKK3/6, together with p38α and MK2.

Cells were pre-treated with either SB203580 or compounds 37 and 38, and subjected to the same stresses (Figure 38B). We noticed that SB203580 partially reduced p38α activation, an observation that was previously reported in some cell lines (Franz et al 1998) probably due to its binding to inactive p38α, which interferes with its activation by upstream MAP2Ks (Munoz et al., 2010). Similarly, we also observed reduced p38α activation with NC-p38i compounds in some of the treatments and cell lines.

Moreover, SB203580 completely inhibited the phosphorylation of MK2 in the three cell lines, whereas compounds 37 and 38 only partially inhibited it in some cases. Interestingly, H9c2 cells seemed to be more sensitive to NC-p38i compounds than U2OS and BBL358 cells, especially in the case of compound 37. In addition, we noticed that NC-p38i compounds significantly affected p38α signalling in BBL358 cells stimulated with NaCl (Figure 38B).

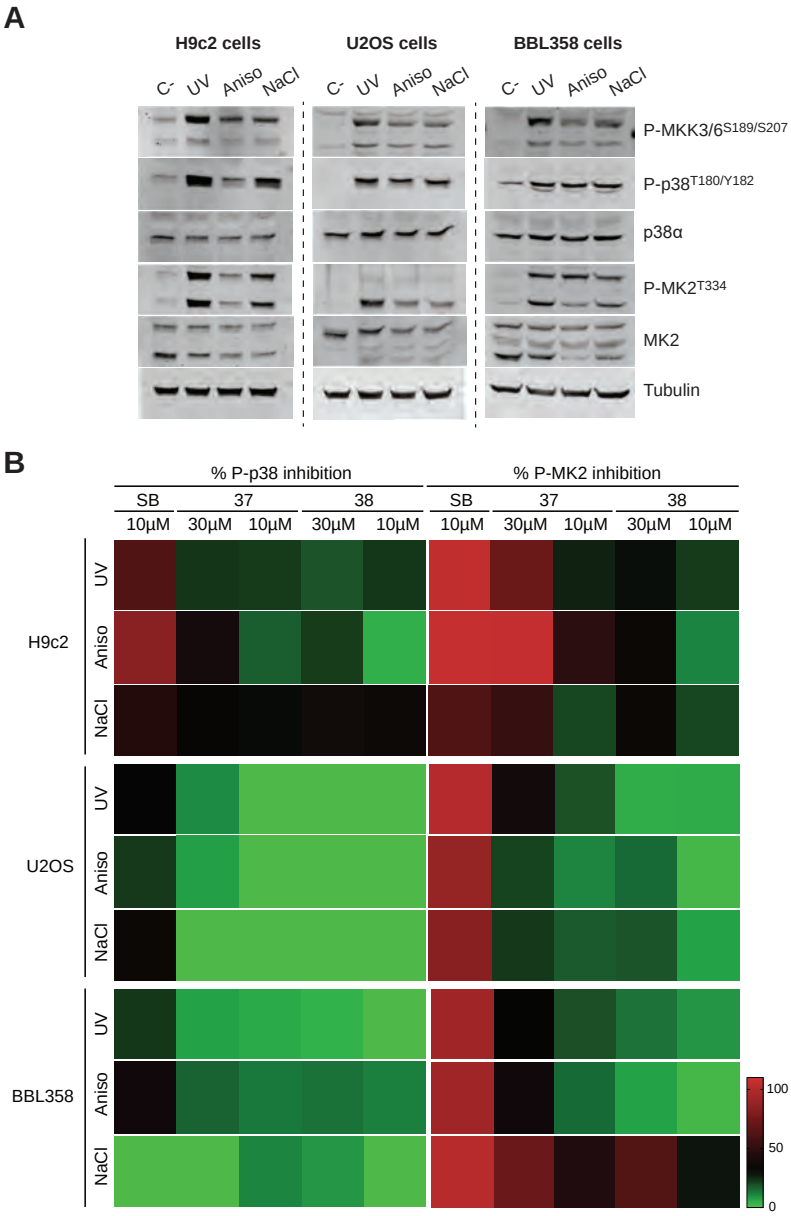

Figure 38. NC-p38i interfere with stress-induced p38 signalling in cells. (**A**) Western blot of H9c2, U2OS and BBL358 cells stimulated with UV irradiation (80 J/m^2, 45 min), anisomycin (20 μM, 4 h) and NaCl (200 mM, 4 h). (**B**) Heatmap showing the percentage of inhibition of p38α and MK2 phosphorylation in H9c2, U2OS and BBL358 cells pre-treated with SB203580 (SB, 10 μM) or compounds 37 and 38 (30 and 10 μM) for 2 h and then stimulated with UV, anisomycin or NaCl as in (A). Data represent the mean ± SD normalized to the DMSO-treated cells of n≥2 experiments for each cell line.

Taken together, these data show that NC-p38i mitigate the kinase activity of p38α in cells, thereby supporting the notion that NC-p38i may allosterically modulate the affinity for ATP.

3.3. NC-p38i protect against doxorubicin-induced cardiac toxicity

Cardiomyocyte death triggered by ischaemia-reperfusion injury involves AMPK activation followed by TAB1-mediated p38α autophosphorylation (Bairwa et al 2016). Similarly, anthracycline-induced cardiomyocyte death also involves oxidative stress production, AMPK and p38α activation, and treatment with the p38α inhibitor SB203580 reduces doxorubicin-induced cardiomyocyte death (Guo et al., 2013; Wold et al., 2005). Therefore, we speculated that specifically targeting the non-canonical p38α activation pathway mediated by autophosphorylation could be useful to ameliorate anthracycline-induced cardiotoxicity without affecting the cancer cell toxicity of the chemotherapeutic drug.

To evaluate whether NC-p38i compounds impair anthracycline-induced cardiotoxicity, we initially used rat myocardial H9c2 cells that were treated with 250 and 500 nM of doxorubicin in combination with either DMSO, SB203580 or compounds 37 and 38. After 24 and 48 h, cell viability and death were measured by MTT, DAPI staining and cleaved caspase-3 immunoblotting. We also performed cell cycle analysis to determine the cell population in G0 as an additional of cell death, and measured doxorubicin accumulation in the death cells. The results show no differences in cell death between H9c2 cells treated with doxorubicin alone or combined either with NC-p38i or with classical ATP-competitive p38α inhibitors (Figure 39).

A

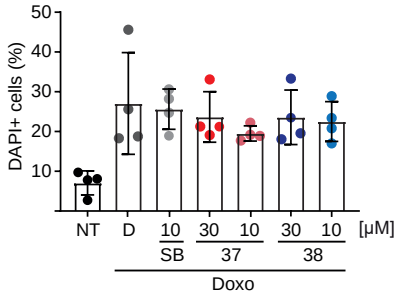

B

	H9c2
MTTs	No differences
DAPI	No differences
Cleaved caspase-3	No differences
SubG0	No differences
Doxorubicin accumulation	No differences

Figure 39. NC-p38i do not mitigate doxorubicin-induced death of H9c2 cells. (**A**) Graph showing the percentage of DAPI positive H9c2 cells after being treated with 500 nM doxorubicin in combination with DMSO (D), SB203580 (SB, 10 μM) or compounds 37 and 38 (30 and 10 μM) for 48h. Data are shown mean ± SD of n=4 experiments. (**B**) Summary of experiments performed in H9c2 cells treated with 250 and 500 nM doxorubicin in combination with DMSO, SB203580 or compounds 37 and 38 for 24 and 48 h.

H9c2 cells are probably not the best model for this type of studies, as anthracycline-induced cytotoxicity has been reported to vary greatly depending on the experimental conditions and number of passages (Witek et al., 2016). As an alternative, use human hiPSC-CMs have been reported to recapitulate the patients' response to doxorubicin-induced cardiotoxicity at the cellular and molecular level (Burridge et al., 2016). Therefore, we decided to use these human cardiomyocytes as a pre-clinical *in vitro* model to investigate the cardioprotective role of NC-p38i compounds 37 and 38.

Before evaluating the effect of combining doxorubicin and NC-p38i in these cells, we tested them separately and measured cell viability and contractility by recording the cellular attachment impedance and the electrical field potential in parallel after 24, 48 and 72 h. As expected, doxorubicin significantly decreased cell viability and beat rate in a dose- and time-dependent manner (Adamcova et al., 2019). Notably, 10 μM doxorubicin had such a strong effect on the attachment and viability of hiPSC-CMs that their beat rate was not properly recorded at 48 and 72 h. Conversely, compounds 37 and 38 did not impair these parameters except at the highest concentration (100 μM), which had a negative effect (Figure 40). In addition, the release to the media of cardiac troponin I (cTnI), a well-known biomarker of cardiomyocyte damage (Herman et al., 1998), was measured at 48 and 72 h. In agreement with the impedance data, cTnI levels significantly increased in doxorubicin treated cells in a dose- and time-dependent manner. Treatment with NC-p38i did not induce the release of cTnI at any concentration, indicating that they do not have a strong cytotoxic effect although the viability and contractility of cardiomyocytes was affected at 100 μM (Figure 41).

Then, hiPSC-CMs were treated with 1 μM doxorubicin in combination with either DMSO or compounds 37 and 38 at different concentrations and followed for 72h. After 24 h, compound 37 improved neither the cell viability nor the beat rate of cardiomyocytes treated with doxorubicin, but compound 38 significantly ameliorated hiPSC-CMs viability at 30, 3 and 1 μM, which was accompanied by an increased beat rate tendency. At 48 h of treatment, we did not observe that NC-p38i increased the cell viability. However, both compounds increased the

beat rate of hiPSC-CMs, suggesting that these compounds might help cells to recover beating but were unable to overcome the irreversible damage induced by doxorubicin at longer time points (Figure 42A). In this line, NC-p38i did not affect the doxorubicin-induced cTnI release. Remarkably, a significant increase of cTnI levels was observed at 100 μM of NC-p38i, suggesting that the damage induced at this high concentration might synergize with the deleterious effect of doxorubicin (Figure 42B). After 72 h treatment, cells were so damaged by doxorubicin that no electrophysiological parameter could be measured.

In summary, these results suggest that compound 38, but not 37, might have a cardioprotective role against doxorubicin-induced toxicity in hiPSC-CMs at short time points.

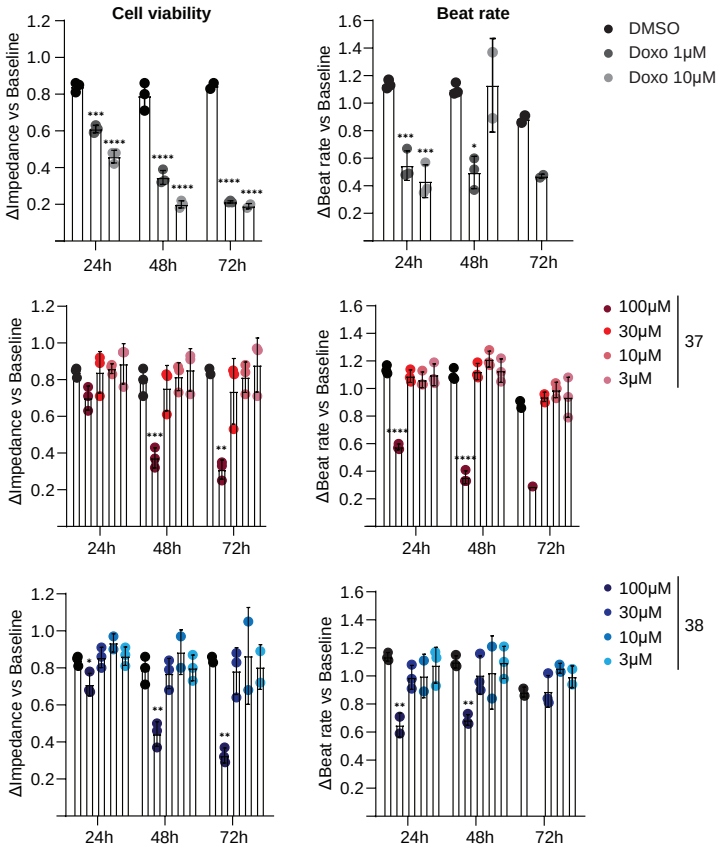

Figure 40. Doxorubicin affects hiPSC-CM viability and beat rate in a time and dose dependent manner. Histograms showing the normalized cell viability and beat rate values of hiPSC-CMs treated with DMSO (0.1%), doxorubicin (1 and 10 μM) or compounds 37 and 38 (100, 30, 10 and 3 μM) for 24, 48 and 72h. DMSO controls are the same in the 3 graphics. Data are shown as mean ± SD of n=1 experiment done in triplicates.

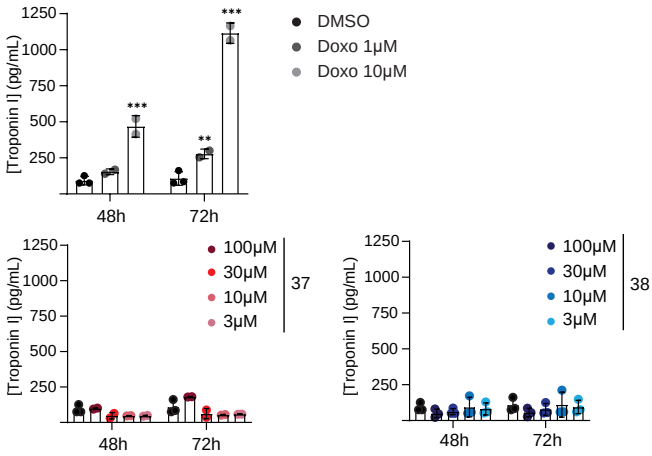

Figure 41. Doxorubicin but no NC-p38i induces Troponin I release. Cardiac Troponin I levels (pg/ml) in the media of hiPSC-CMs treated with DMSO (0.1%), doxorubicin (1 and 10 µM) or compounds 37 and 38 (100, 30, 10 and 3 µM) for 48 and 72h. Data are shown mean ± SD of n=1 experiment done in triplicates.

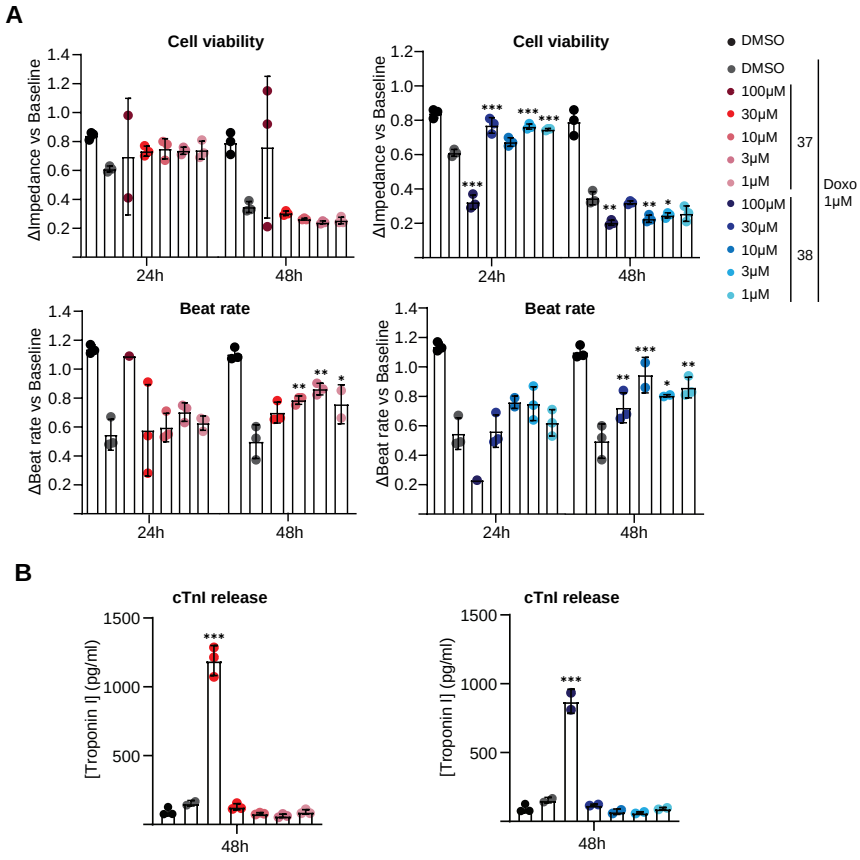

Figure 42. Compound 38 might have a cardioprotective role in hiPSC-CMs treated with doxorubicin. (**A**) Histograms representing the normalized cell viability and beat rate values of hiPSC-CMs treated with 1 μM doxorubicin in combination with either DMSO (0.1%) or compounds 37 and 38 (100, 30, 10 and 3 μM) for 24 and 48h. (**B**) Histograms representing the cardiac troponin I (cTnI) (pg/ml) in the cell media of cells treated with 1 μM doxorubicin in combination with 37 and 38 (100, 30, 10 and 3 μM) for 48h. Symbols are the same as in (**A**). Data are shown as mean ± SD of n=1 experiment done in triplicates.

To further characterise the possible application of NC-p38i compounds for the cardioprotection to chemotherapy, we analysed their effect on the cytotoxic effect of anthracyclines on cancer cells, which is essential for chemotherapy success. Human MDA-MB-231 and MCF7 breast cancer cell lines and murine cells derived from PyMT-induced mammary tumours (BBL358) were treated with doxorubicin in combination with either DMSO, SB203580 or compounds 37 and 38 and cell death was measured by DAPI staining. The results indicated similar levels of cell death in human breast cancer cells treated with doxorubicin alone or combined with NC-p38i compounds. Curiously, we observed that treatment with compounds 37 and 38, but not with SB203580, reduced doxorubicin-induced death in BBL358 cells (Figure 43). Additional studies should explore whether compounds 37 and 38 protect murine BBL358 cells from doxorubicin by reducing their proliferation.

In conclusion, NC-p38i compounds do not seem to have a major effect in the chemotherapeutic effect of anthracyclines in human breast cancer cells.

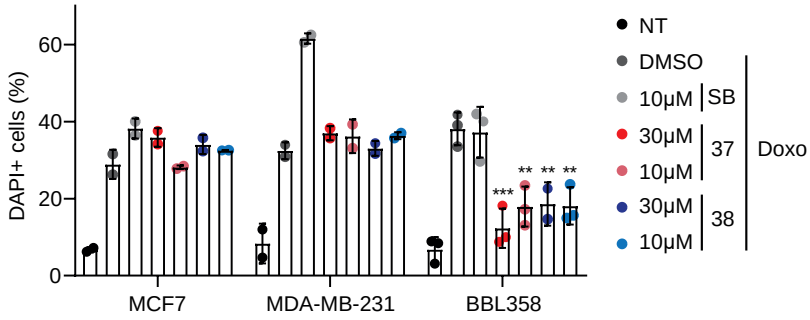

Figure 43. NC-p38i do not impair doxorubicin-induced death in human breast cancer cells. (**A**) Histogram showing the percentage of DAPI positive MCF7, MDA-MB-231 and BBL358 cells after treatment with 2 μM doxorubicin in combination with DMSO (D), SB203580 (SB, 10 μM) or compounds 37 and 38 (30 and 10 μM) for 48 h. Data are shown as mean ± SD of n≥2 experiments.

To investigate whether NC-p38i ameliorate anthracycline-induced cardiotoxicity *in vivo*, experiments using zebrafish embryos were performed (Calienni et al., 2018; Chang et al., 2014). First, we evaluated the maximum tolerated dose (MTD) in zebrafish embryos for compounds 37 and 38 and observed no significant toxicity up to a concentration of 1000 μM. However, it should be noted that NC-p38i precipitated at 1000 μM (Figure 44A).

Therefore, both compounds were tested at 10, 30 and 100 μM in combination with 100 μM doxorubicin, and after 72 h of exposure, the heart rate of zebrafish embryos was manually counted. Doxorubicin alone induced bradycardia, which was not recovered by compound 37. In contrast, compound 38 improved the heart rate at the three concentrations tested, although it was only significant at 10 μM compared to animals treated with doxorubicin alone (Figure 44B).

Additionally, morphology was analysed. Hearts from embryos treated with the vehicle control all contained two chambers, whereas hearts from doxorubicin-treated embryos were dimmer and contained only one smaller chamber. The positioning of some embryos treated with compounds 37 and 38 made it not possible to detect the heart, and those were classified as uncertain. In agreement with the heart rate results, we observed that compound 38 interfered with doxorubicin-induced heart malformations. The morphologic improvement of hearts treated with compound 38 was observed at 10 and 30 μM but was strongest at 100 μM. Of note, despite compound 37 at 100 μM also improved heart morphology, it did not seem to improve the heart rate (Figure 44C).

Altogether, these results support previous data in hiPSC-CMs and suggest that NC-p38i compound 38 can ameliorate heart damage induced by doxorubicin treatment, thereby suggesting a potential cardioprotective role against anthracycline-induced cardiac toxicity.

A

	Embryos phenotype (x, y, z)	
	37	38
1000 µM	10/0/0 **P**	10/0/0 **P**
100 µM	10/0/0	9/1/0
10 µM	10/0/0	9/1/0
1 µM	10/0/0	10/0/0
0.1 µM	9/1/0	10/0/0
DMSO	9/1/0	

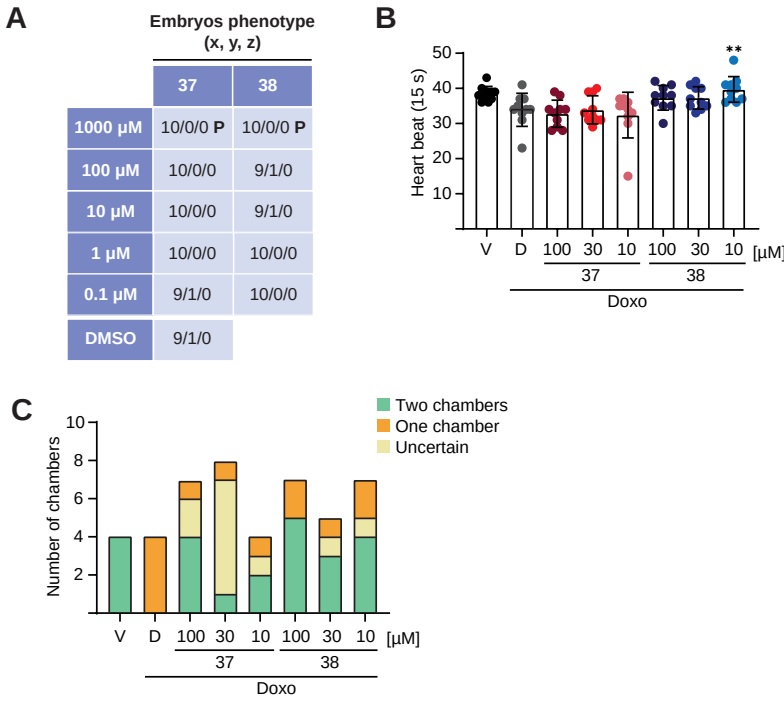

Figure 44. NC-p38i protect zebrafish embryos against doxorubicin-induced cardiac toxicity. (**A**) Results from the maximum tolerated dose experiment performed in embryos (3 hpf) incubated with compounds 37 and 38 (0.1, 1, 10, 100 and 1000 µM) for 72 h. Embryos phenotype: x, not affected; y, affected but not dead; z, dead. 10 embryos were used per condition. hpf, hours post-fertilization. (**B**) Histogram showing the heart beat (number of beats counted in 15 sec) of zebrafish embryos after treatment with vehicle and doxorubicin (D, 100 µM) alone or in combination with compounds 37 and 38 (10, 30 and 100 µM) for 72 h. V, vehicle, 0.5% DMSO. Data are shown as mean ± SD. (**C**) Histogram showing the heart morphology of zebrafish embryos from panel (B) and classified as indicated.

4. NC-p38i possess promising drug-like and ADME-Tox properties

4.1. NC-p38i are highly specific for p38α

To assess the selectivity of NC-p38i compounds 37 and 38, a kinase profiling study against 97 different human protein kinases was performed. Both compounds mainly inhibited the activity p38α, and to a lesser extent also inhibited p38β and COT (Figure 45).

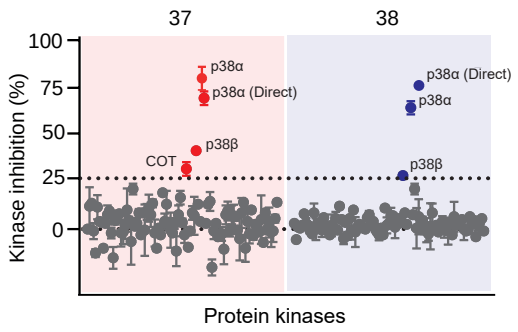

Figure 45. Kinase selectivity profile of NC-p38i. Graph showing kinase selectivity of compounds 37 and 38 (10 μM) against a panel of 97 human kinases (Supplementary Table 2). Data show the percentage of inhibition in the presence of the indicated compound. Particular kinases were assayed at a concentration of ATP at or below their apparent Km. Results are shown as mean ± SD from n=1 experiment done in duplicates.

These results support the high-selectivity of compounds 37 and 38, and suggest that they do not function as general inhibitors of protein kinase activity.

p38α and p38β are 74% identical in amino acid sequence (Jiang et al., 1996). To evaluate whether the p38α amino acids affected by the binding of NC-p38i compounds were conserved in p38β, we compared the sequences of both proteins. Interestingly, we observed that most residues affected by NC-p38i binding to p38α (Figure 29) were conserved in p38β except for S28, T44, T218, H228 and F270 (Figure 46), suggesting that they might be important for NC-p38i binding and/or activity.

Interestingly, p38β strongly autophosphorylates *in vitro* independently of TAB1 (Beenstock et al., 2016; Zhou et al., 2006). To investigate whether NC-p38i inhibit p38β autophosphorylation, we performed *in vitro* assays using non-phosphorylated recombinant GST-p38β protein in presence of ATP and NC-p38i. The results indicated that NC-p38i also inhibit p38β autophosphorylation, but with much less potency than for p38α (Figure 47).

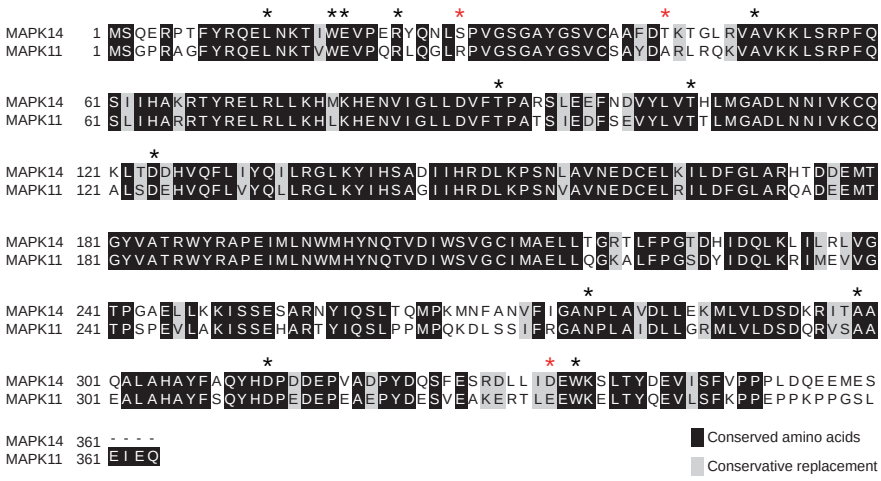

Figure 46. Comparison of potential NC-p38i binding residues in p38α and p38β. Amino acid sequence comparison of human p38α (MAPK14) and p38β (MAPK11) generated using T-Coffee. Conserved amino acids and conservative replacements for amino acids with similar charges, are highlighted in black and grey, respectively. Asterisks indicate amino acids affected by NC-p38i binding to p38α that are conserved (black) or non-conserved (red) in p38β.

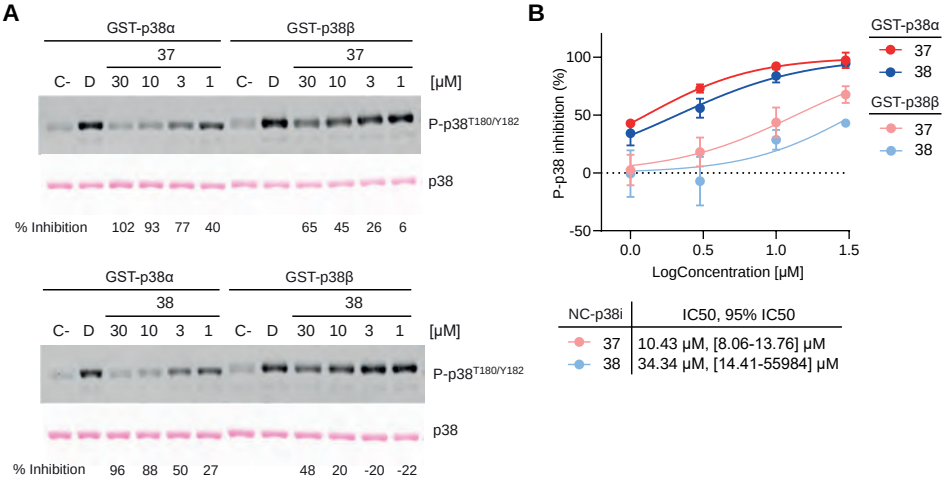

Figure 47. Effect of NC-p38i on the spontaneous p38β autophosphorylation activity. (**A**) Western blots of GST-p38α and GST-p38β *in vitro* autophosphorylation assays in the presence of compounds 37 and 38 at the indicated concentrations. C-, negative control containing GST-p38α or GST-p38β without ATP. D, DMSO. Ponceau staining indicates total GST-p38α or GST-p38β proteins. Results are representative from n=2. (**B**) Dose-response inhibition curves of basal p38α and p38β autophosphorylation by compounds 37 and 38. Data were fitted using a nonlinear regression fit model (Graphpad Prism) to determine IC50s. Results are shown as mean ± SD from n=2 experiments. CI, confidence interval.

4.2. NC-p38i have cytostatic but not cytotoxic effects at high concentrations

A potential use of NC-p38i compounds would be to treat cardiovascular diseases, being cardiomyocytes their target cells. Therefore, we measured whether compounds 37 and 38 could affect cell viability of different cardiac-related cells, including H9c2 cells, primary neonatal rat ventricular myocytes (NRVMs) and cardiac fibroblasts, and hiPSC-CMs.

As differentiated cardiomyocytes do not proliferate, cells were seeded at high confluency and treated with different concentrations of compounds 37 and 38. After 24 and 48 h, NC-p38i did not induce significantly decreased cell viability at any concentration, as measured by MTT assays (Figure 48A). Interestingly, primary neonatal rat cardiomyocytes were a bit more sensitive to both compounds at 100 and 30 μM after 24 h of treatment. In addition, we did not observe increased death in H9c2 cells treated with NC-p38i, in line with the MTT results. However, human cardiomyocytes treated with compounds 37 and 38 at 100 μM showed an increase in apoptotic cell death compared to H9c2 cells (Figure 48B), thus correlating with previous impedance data (Figure 40).

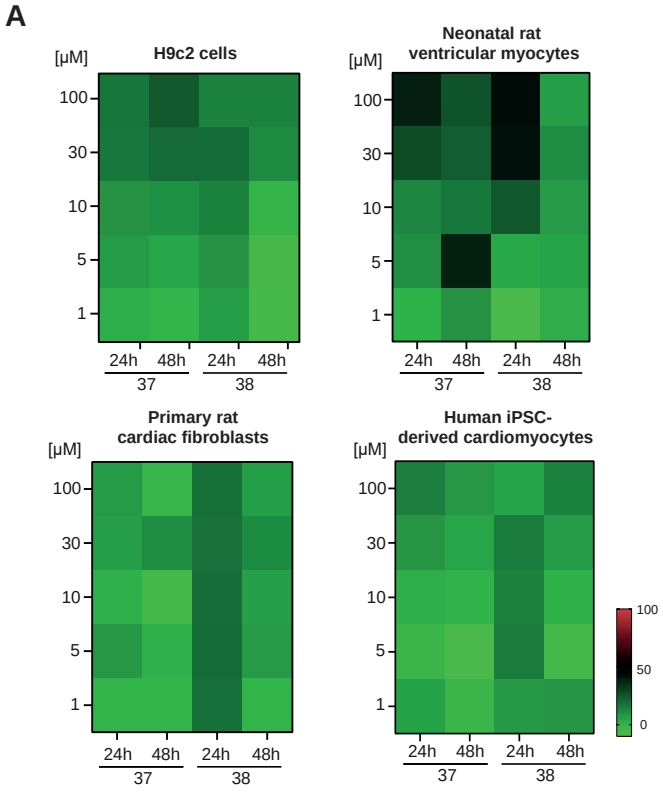

B

H9c2 cells (DAPI+, %)

	37		38	
	24h	48h	24h	48h
100 µM	8.2	21	7.8	7.2
30 µM	6.3	12.2	8.6	5.3
10 µM	6.7	5.5	7.5	3.9
1 µM	7.5	12.1	7.7	4.8
DMSO	6.1	3.2		

Human iPSC-derived cardiomyocytes (DAPI+, %)

	37		38	
	24h	48h	24h	48h
100 µM	26.5	25.5	16.3	27.9
30 µM	10.2	16.5	14	25.4
10 µM	13.6	18.6	13.2	21.2
1 µM	15	22	17.4	25.9
DMSO	14.4	17		

Figure 48. NC-p38i are not cytotoxic in non-proliferating cells. (A) Heatmaps showing the effect of treatment for 24 and 48 h with compounds 37 and 38 (100, 30, 10, 5 and 1 µM) on the viability of H9c2 cells (n=3), neonatal rat ventricular myocytes (37, n=2; 38, n=1), primary cardiac fibroblasts (37, n=2; 38, n=1) and hiPSC-CMs (n=1) seeded at high confluency conditions. Percentage of the reduced cell viability was measured by MTT and normalized to DMSO-treated cells. Data represent the mean ± SD of n=2-3 experiments or mean of n=1 done in duplicates. (**B**) Effect of treatment for 24 and 48 h with compounds 37 and 38 (100, 30, 10 and 1 µM) on the death of H9c2 cells and hiPSC-CMs seeded at high confluency. The percentage of cell death was measured by DAPI staining and analysed by FACS. Data represent the mean ± SD of n=2 experiments for H9c2 cells and n=1 for hiPSC-CMs.

Interfering with p38α activity has been shown to reduce the proliferation of some cancer cells (Canovas et al., 2018). Since NC-p38i compounds were not cytotoxic, we wondered whether they might affect cell proliferation. We performed MTT assays using different cancer cell lines (BBL358, MCF7 and BT549 cells) seeded at low confluency conditions and treated with the compounds 37 and 38 at different concentrations for 48 and 72 h. We observed a slightly reduced of proliferation in BBL358 and MCF7 cells treated with NC-p38i at 30 µM (Figure 49A).

Moreover, we performed colony formation assays to further study the effect of NC-p38i compounds on cell proliferation. We observed that compounds 37 and 38 significantly reduced colony formation by BBL358 cells at 30 µM, which is consistent with a cytostatic effect of these compounds at high concentrations (Figure 49B).

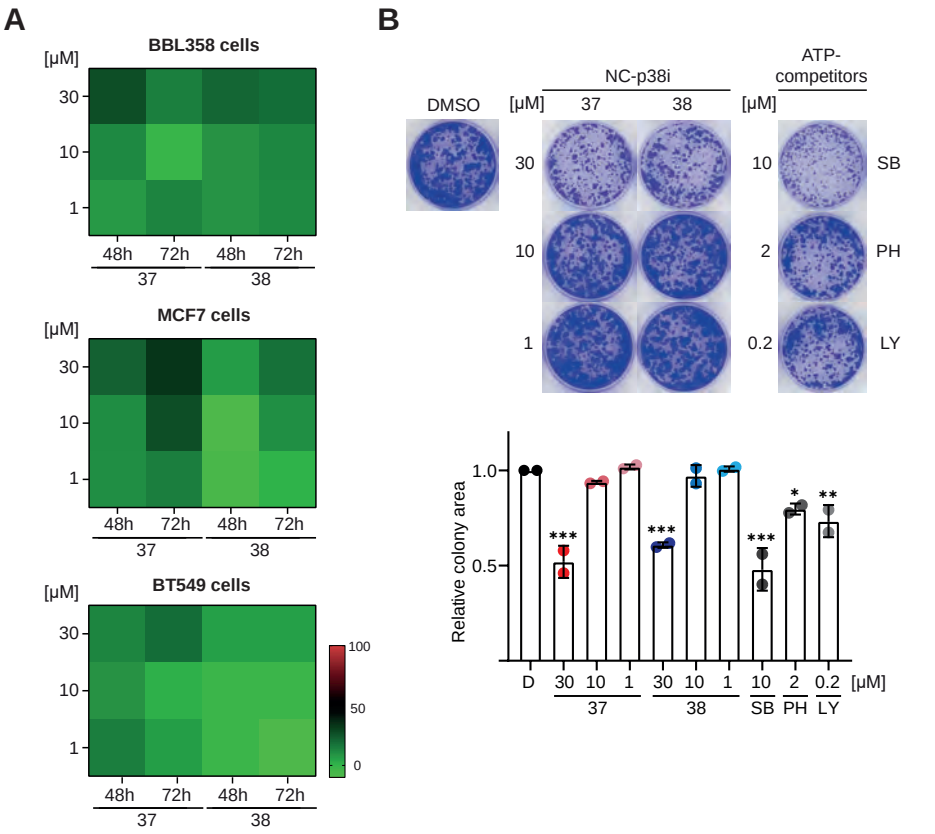

Figure 49. NC-p38i are cytostatic in proliferating cancer cells. (A) Heatmaps showing the effect of treatment for 48 and 72 h with compounds 37 and 38 (30, 10 and 1 μM) on the viability of BBL358, MCF7 and BT549 breast cancer cells seeded at low confluency. The percentage of the reduced cell viability was measured by MTT and normalized to DMSO-treated cells. Data represent the mean ± SD of n=2 experiments in duplicates. **(B)** Colony formation assays of BBL358 cancer cells treated with compounds 37 and 38 (30 and 10 μM) or ATP-competitors (SB203580, 10 μM; PH797804, 2 μM; and LY2228820, 0.2 μM) for 10 days. Dare shown as mean ± SD of n=2 experiments.

4.3. NC-p38i posess good drug-like properties

As a first approach to predict the physicochemical and ADME-Tox properties of compounds 37 and 38, we used the QikProp software (Schrödinger Release 2019-1: QikProp, Schrödinger, LLC, New York, NY, 2019). The parameters analysed were aqueous polar-surface area (PSA), solubility and lipophilicity, Caco-2 cell permeability, metabolic stability, IC50 for inhibition of hERG K^+ cardiac channel and binding to human serum albumin (Figure 50). Based on the predicted

parameters, compounds 37 and 38 appear to be promising hits as they are small molecules (MW 300-400) with good solubility and polarity values, which correlate with high permeability, low metabolic profiles and binding to plasmatic proteins. However, we observed that the logIC50 values (QPlogHERG) for hERG K^+ channel blockage were below -5, which were concerning.

	37	38
Molecular weight	327.4	345.4
Polar surface area (PSA)	75.6	74.9
Solubility (QPlogS)	-4.8	-5.0
Lipophilcity (QPlogPo/w)	2.8	3.0
Caco-2 permeability (QPPCaco)	898.8	959.4
Metabolism	1	1
IC50 hERG K^+ channel inhibition (QPlogHERG)	-6.2	-6.1
Binding human serum albumin (QPlogKhsa)	0.14	0.17

Figure 50. Predicted physicochemical and ADME-Tox properties of NC-p38i. Summary of the predicted PSA (7 to 200), solubility (QPlogS, -6.5 to 0.5), lipophilicity (QPlogPo/w, octanol/water partition coefficient; -2.0 to 6.5); number of expected primary metabolites (1-8); Caco-2 cells permeability (>500 nm/sec), IC50 for human hERG K^+ blockage (QPlogHERG, concern below -5); and binding to human serum albumin (-1.5 to 1.5) were calculated for compounds 37 and 38.

Some of these properties were experimentally validated (Figure 51). We observed that both compounds exhibited high permeability in intestinal Caco-2 cells and showed weak inhibition of hERG channel at 10 μM. These data suggest that NC-p38i compounds 37 and 38 might be highly absorbed *in vivo* and might not induce undesired cardiac toxicity.

In addition, to assess the *in vitro* metabolic stability of compound 37 and 38, we determined their degradation rate in the presence of human and rat liver microsomes. The estimated $t_{1/2}$ suggested that both compounds were much more stable in human microsomes than in rat microsomes.

On the other hand, both compounds exhibited high binding to plasmatic proteins, 92-94% approximately, indicating that only 6-8% of NC-p38i would be free in the plasma.

	Caco-2 permeability (P_{app} A-B*10^{-6}cm/s)	hERG K^+ channel inhibition (%)	Human/rat microsomal stability (t1/2, min)	Human/rat plasmatic protein binding (%)
37	13.17	20.51 ± 1.24	45.3 / 1.13	92 / 93
38	15.52	27.25 ± 2.73	49.0 / 1.34	93 / 94

Figure 51. Determination of ADME properties of NC-p38i. Compounds 37 and 38 at 10 μM were tested in the CacoReady™ intestinal barrier permeability system (P_{app} A-B), inhibition of hERG K^+ channel, human and rat liver microsomes and binding to human and rat plasmatic proteins, respectively. P_{app} > 10*10^{-6}cm/s predicts high (70-100%) *in vivo* intestinal absorption. hERG K^+ channel inhibition data are shown as mean ± SEM of n=1 experiment in duplicates.

Fluorination of compounds has been linked to enhanced biological potency by improving metabolic stability, bioavailability and ligand-protein binding affinity (Purser et al., 2008; Shah and Westwell, 2007). Indeed, compound 38 is a fluorinate derivative of compound 37. However, both compounds had similar metabolic stability in rat microsomes. Therefore, we decided to synthesize two additional derivates of compound 38, IRB-111 and IRB-112 (Figure 52A) and test their metabolic stability in human and rat microsomes (Figure 52B). We concluded that these modifications were not sufficient to increase the compounds' metabolic stability in rat microsomes. Indeed, we even observed some decreased stability in human microsomes. Therefore, we continued with compounds 37 and 38 for the *in vivo* ADME-Tox characterization.

A

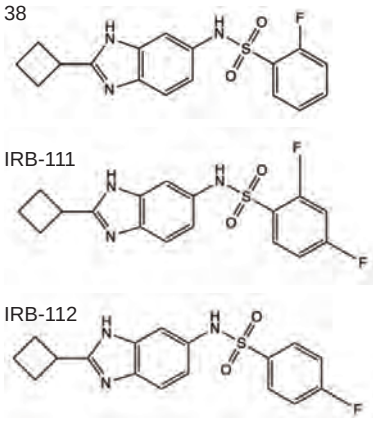

B

	Human microsomal stability (t1/2, min)	Rat microsomal stability (t1/2, min)
IRB-111	18.1	0.9
IRB-112	22.5	-

Figure 52. Fluorinate derivatives of NC-p38i do no improve the metabolic stability. (**A**) Structure of the fluorinate derivatives of compound 38 IRB-111 and IRB-112. (**B**) Summary of the compounds' associated metabolic stability in human and rat microsomes ($t_{1/2}$).

Before testing NC-p38i compounds *in vivo*, we performed a solubility study to select a proper vehicle for intravenous (IV) administration. Compound 38 was prepared in seven vehicles at 20 mg/ml and the solubility was measured by laser nephelometry. The results indicated that compound 38 was only soluble in vehicle-4, but insoluble in the other tested vehicles (Figure 53). Therefore, vehicle-4 was selected for *in vivo* experiments.

Veh #1	5% DMSO, 5% Solbutol HS-15, 90% PBS	Insoluble
Veh #2	10% Cremophor EL, 10% ethanol, 80% of 0.9% NaCl	Insoluble
Veh #3	10% DMA, 10% ethanol, 20% PG, 60% of 0.9% NaCl	Insoluble
Veh #4	10% DMA, 20% PG, 40% PEG 400, 30% of 0.9% NaCl	Soluble
Veh #5	40% PEG 400, 10% ethanol, 50% of 0.9% NaCl	Insoluble
Veh #6	40% PEG 400, 10% Cremophor EL, 70% of 0.9% NaCl	Insoluble
Veh #7	0.5% Tween 80, 99.5% of 0.9% NaCl	Insoluble

Figure 53. Solubility study of NC-p38i in different vehicles suitable for intravenous administration. DMA, dimethylacetamide; PG, propylene glycol; PEG, polyethylene glycol.

Next, we performed an MTD study in Sprague-Dawley rats. Compounds 37 and 38 were administered to four animals (two males and two females) at concentrations ranging from 10 to 100 mg/kg. The compounds' associated toxicity was assessed during the first 15 and 60 min and animal survival was evaluated up to 72 h. At each dose level, animals were observed for the presence of acute toxic symptoms (i.e. mortality, convulsions, tremors, muscle relaxation and sedation) and autonomic effects (i.e. diarrhoea, salivation, lacrimation, vasodilation and piloerection) (Figure 54).

No relevant associated toxicity was observed at doses ≤ 30 mg/kg in both male and female rats, and no body weight changes were noted, suggesting that these concentrations are non-toxic. However, decreased limb and abdominal tone as well as deeper respirations were noted at 15 min and 1 h after administration of compound 37 at 30 mg/kg.

At 50 mg/kg, rats had a slight decrease in the body tone after 60 min of dosing. No other significant side effects were observed within the 72 h of examination period, thereby considering this concentration as well tolerated.

At dose levels ≥ 65 mg/kg, moderate to severe decrease in alertness; touch scape; grip strength; limb, abdominal and body and abdominal tone; as well as

laboured respiration and gait changes were observed at 15 min after administration. These adverse effects decreased at 60 min, and animals neither die nor changed in body weight.

Importantly, animals treated with 100 mg/kg showed 25% and 50% mortality within a few minutes of administration of both compounds, indicating that this concentration is highly toxic.

	37	38
10 mg/kg	No toxicity	No toxicity
30 mg/kg	No toxicity	No toxicity
50 mg/kg	N.D.	Very low toxicity
65 mg/kg	N.D.	Mild toxicity
85 mg/kg	N.D.	Mild toxicity
100 mg/kg	1/4 deaths	2/4 deaths

Figure 54. Maximum tolerated dose of NC-p38i in Sprague-Dawley rats. Compounds 37 and 38 were formulated in 10% DMA, 20% PG, 40% PEG 400, 30% of 0.9% NaCl at 2, 6, 10, 13, 16 and 20 mg/ml for IV administration of 10 to 100 mg/Kg. A dosing volume at 5 ml/kg was applied. Full clinical examination was assessed during the first 15 and 60 min, and animal survival was evaluated at 24, 48 and 72h. N.D., not determined.

Based on the observed toxicity, we chose compounds 37 and 38 at 30 mg/kg to evaluate their pharmacokinetic properties in rats (Figure 55A). Both compounds exhibited good PK properties with high terminal half-life ($t_{1/2}$) and plasma exposure (AUC), reasonable mean residence time (MRT), high systemic clearance (Cl) and high volume of distribution (V_{ss}). For instance, compounds 37 and 38 demonstrated $t_{1/2}$ of 4.67 and 5.22 h, plasma exposure of 74.3 ± 19.4 and 50.7 ± 9.5 µM/ml, and clearance values of 21 ± 6 and 29 ± 6, respectively.

However, given the observed binding of NC-p38i to plasmatic proteins (Figure 51R), we calculated the concentration of free compound as an estimation of the concentration of drug that could directly arrive to the target cell (i.e. cardiomyocytes) (Figure 55B). Considering that *in vitro* IC50 values of both compounds 37 and 38 is approximately 1 µM, these data indicate that free plasma levels NC-p38i would be around 10 times greater than the *in vitro* IC50 at 3 min after administration.

Together, these results suggest that the *in vivo* administration of NC-p38i should be performed just prior or during the damaging insult (i.e. ischaemia-reperfusion injury).

A

	PK rat, IV, 30 mg/kg	
	37	38
C_0 [µM]	114.6 ± 5.5	113.2 ± 18.4
$t_{1/2}$ (h)	4.69 ± 1.22	5.27 ± 0.86
AUC_{Inf} (µM/ml)	74.6 ± 19.4	50.7 ± 9.5
MRT (h)	1.29 ± 0.51	0.87 ± 0.23
V_{ss} (l/kg)	2 ± 1	2 ± 1
CL (ml/min/kg)	21 ± 6	29 ± 6

B

	37		38	
	[µM]	[µM]*[%37_{free}]	[µM]	[µM]*[%38_{free}]
3 min	98.3 ± 40.3	6.9 ± 2.8	97.8 ± 13.7	5.9 ± 0.8
10 min	69.2 ± 14.8	4.8 ± 1.0	69.6 ± 7.2	4.2 ± 0.4
30 min	37.1 ± 10.3	2.6 ± 0.7	27.2 ± 5.6	1.6 ± 0.3
1 h	21.3 ± 9.4	1.5 ± 0.7	9.9 ± 2.7	0.6 ± 0.2
2 h	8.3 ± 4.3	0.6 ± 0.3	1.7 ± 0.8	0.1 ± 0.05
4 h	0.9 ± 0.3	0.06 ± 0.02	0.3 ± 0.1	0.02 ± 0.005
6 h	0.3 ± 0.2	0.02 ± 0.01	0.2 ± 0.07	0.01 ± 0.004
24 h	0.06 ± 0.01	0.004 ± 0.001	0.02 ± 0.02	0.001 ± 0.001

Figure 55. Single dose plasma pharmacokinetics of NC-p38i administered intravenously in rats. (**A**) PK profile of compounds 37 and 38 formulated at 6 mg/ml in 10% DMA, 20% PG, 40% PEG 400, 30% of 0.9% NaCl. Dosing volumes of 5 ml/kg were administered IV to reach a concentration of 30 mg/kg. PK parameters of each compound were obtained from the non-compartmental analysis (NCA) of the plasma data in (**B**) using WinNonlin. Results are shown as mean ± SD of n=3 rats per compound. The concentration of 37 and 38 in plasma samples was determined by LC-MS/MS in [ng/ml] and converted to [µM]. C_0, initial concentration; $t_{1/2}$, terminal half time; AUC, area under the concentration-time curve; AUC_{inf}, AUC curve to infinite time; MRT, mean residence time; V_{ss}, volume of distribution at steady state; CL, total body clearance. (**B**) Plasmatic compounds 37 and 38 levels corrected with rat plasmatic protein binding (%) data.

DISCUSSION

For the last decades, p38α has been an attractive druggable target to treat inflammation, cardiovascular diseases and cancer (Canovas and Nebreda, 2021). The availability of potent p38α inhibitors has allowed to study the role of this kinase in pathophysiology, but traditional pharmacologic approaches using ATP-competitors have not succeeded in clinical trials yet. Systemic inhibition of p38α by targeting its active site may lead to the upregulation of feedback loops, which together with potential off-target effects may result in toxicity that undermines the beneficial effect of the compounds. Therefore, efforts to discover novel p38α inhibitors are key to tackle this bottleneck (Haller et al., 2020).

Allosteric modulators have been proposed as a new generation of kinase inhibitors (Wu et al., 2015). *In silico* 3D structure-based drug design strategies offer a rational approach for the generation of candidate compounds (Batool et al., 2019). Integration of these computational tools with structural and molecular biology assays provide the basis for discovering novel kinase inhibitors (He et al., 2019).

Here, we present a comprehensive biochemical and structural characterization of a novel class of p38α inhibitors that includes testing in models of non-canonical p38α associated diseases and assessing their drug-like properties.

1. Discovery and characterization of novel allosteric inhibitors of p38α

Current p38α inhibition strategies include tailor-made molecules (mainly type-II) for treating lung or skin diseases by local application (Haller et al., 2020), acute p38α inhibition in combination with other drugs for short-term treatments (Patnaik et al., 2016; Vergote et al., 2020) and inhibitors of specific substrates, such as MK2 (Davidson et al., 2004; Gomez-Gutierrez et al., 2016). Although showing increased specificity, these compounds may interfere with the canonical p38α activation pathway.

Emerging evidence highlights that targeting the non-canonical p38α pathway could be an alternative approach with greater specificity, given that this activation mechanism is restricted to a subset of functions in certain cell types (Arabacilar and Marber, 2015). For example, small-molecule derivates from admantanes have been proposed as type-IV p38α-TAB1 complex inhibitors, which reduce TAB1 phosphorylation *in vitro* but not p38α autoactivation (De Nicola et al., 2018; Nichols et al., 2020). While the *in vivo* potency of these compounds has

not been addressed yet, these studies emphasize the importance to find novel modulators of non-canonical p38α signalling to treat myocardial infarction and other TAB1-induced p38α activation-associated diseases.

In this work, we run an *in silico* small molecule drug discovery program to discover novel inhibitors of non-canonical p38α activation. Then, we performed *in vitro* autophosphorylation assays allowed us to identify several candidate compounds, named NC-p38i, that inhibit TAB1-induced (Figure 14) and spontaneous p38α autophosphorylation (Figure 17) *in vitro* within the low micromolar range (Figure 21).

Using SPR and ITC experiments, we have shown that NC-p38i can form a fast complex with p38α (Figures 19 and 22). Although we cannot measure their associated kinetic and thermodynamic parameters, NC-p38i are able to increase the thermal stability of p38α in a concentration-dependent manner (Figure 23). Hence, these data indicate that NC-p38i have a low residence time.

NC-p38i were initially designed to target the non-canonical TAB1 binding site on p38α. However, FP competitive experiments showed that NC-p38i do not appear to interfere with $TAB1_{386-414}$ binding to p38α (Figure 24). Moreover, we observed an additive effect on thermal stability when p38α was incubated with both ligands (Figure 25), suggesting that NC-p38i and TAB1 can both simultaneously bind to p38α.

To characterize the mechanism of NC-p38i binding to p38α, we performed NMR and X-ray co-crystallization experiments. These assays show that NC-p38i can induce multiple changes on the entire p38α protein structure, suggesting a high plasticity in the modulation of p38α autophosphorylation activity.

The analysis of several p38α crystals seeded in the presence of NC-p38i allowed us to determine two structures. Intriguingly, an extra electron density corresponding to NC-p38i was only observed in one of them. This could be attributed to the low residence time of these compounds, suggesting that NC-p38i can diffuse in and out of the crystallized protein. Unexpectedly, the compound 37 was found above SB203580 in the ATP-site, which indicates that p38α may adopt certain conformations that restrict its accessibility there (Figure 31). Indeed, we observed that this binding mode is enabled by the dynamic position of the Y35 residue (Figure 32). Moreover, this observation is supported by *in vitro* autophosphorylation assays showing that NC-p38i potency decreases at high concentrations of ATP, as well as NanoBRET experiments indicating that NC-p38i can displace an ATP-competitive ligand from the p38α active site in cells (Figures 35 and 36).

SPR binding assays show that NC-p38i associates to both inactive non-phosphorylated (DFG-out) and active phosphorylated (DFG-in) forms of p38α (Figure 19). Notably, NC-p38i might inhibit p38α autophosphorylation *in vitro* by binding to inactive non-phosphorylated kinase first. Our p38α crystal structures exhibit a typical DFG-in conformation that allows SB203580 binding (Young et al., 1997). Hence, additional *in silico* molecular dynamics and crystallography experiments should be performed to explore whether NC-p38i can also enter into the ATP-site of the DFG-out p38α. For example, the type-II inhibitor BIRB796 could be used instead of SB203580 to fix the inactive form of the protein.

We found that compound 37 induces significant allosteric changes in the N-terminal domain and the active site of p38α, which decrease its affinity for ATP. In addition, alterations of the canonical ED site and the αD-helix (Figure 33 and 34) may impair the optimal occupancy of the C-terminal part of TAB1. Bi-partite binding of TAB1 to p38α stabilizes the active conformation of the protein and induces the rearrangement of the activation loop that triggers autophosphorylation in *cis* (DeNicola et al., 2013). However, this loop is poorly visible in our crystal structures due to its high mobility, which prevents the proper observation of the TGY motif (Supplementary Figure 2E). Overall, we consider that in addition to modify the affinity for ATP, NC-p38i may impair the acquisition of the p38α prone-to-autoactivate conformation, reducing both TAB1-induced and spontaneous autophosphorylation.

The amino acids comprising the ED site (E160 and D161) and the CD domain (D313, D315 and D316) of p38α form a docking groove behind the hinge region that is essential for interactions with activators, substrates, and phosphatases such as MKK6, MK2 and DUSP10/MKP5 (Tanoue et al., 2000). While compound 37 affects the ED site, the CD domain is not altered. Notably, our in vitro kinase assays show that NC-p38i do not reduce canonical activation of p38α by MKK6 but weakly decrease the phosphorylation of MK2 *in vitro* and in H9c2 cells (Figures 18 and 38). Nevertheless, compounds 37 and 38 can inhibit around 75 % of the p38α catalytic activity at 10 μM according to the *in vitro* kinase selectivity panel assays (Figure 45). These results suggest that while NC-p38i may affect the catalytic activity of p38α, they do not influence its docking interactions. In line with this idea, the ability of these compounds to decrease the kinase activity of p38α differs depending on the experimental conditions of the assay, which may impact on the p38α conformation.

Allosteric regulation of protein kinases is a bidirectional process. On the one hand, interaction of ligands at the regulatory sites usually affects the active site. On the other hand, several studies emphasize that ligands or compounds

interacting with the ATP-binding site regulate not only the kinase function *per se* but also control protein-protein interactions (so-called reverse allostery) (Leroux and Biondi, 2020). For example, ATP-competitive inhibitors PS653 and MLN8237 inhibit the AGC kinases PDK1 and Aurora kinase, respectively, and affect their PIF-pocket, a hydrophobic pocket located in the N-lobe between helices αB and αC and β4 and β5 strands (Schulze et al., 2016). Additional examples illustrating this process are the pseudokinase KSR2 and the endoplasmic reticulum transmembrane kinase/endoRNase IRE-1a. The compound APS-2-79 stabilizes KSR2 and antagonizes the oncogenic Ras signalling by decreasing its interaction with RAF and subsequent phosphorylation of MEK (Dhawan et al., 2016). APY29, sunitinib and compound 3 inhibit the oligomerization and RNase activity of IRE-1a (Wang et al., 2012). Furthermore, there is evidence that JNK (Lombard et al., 2018), ERK2 (Hari et al., 2014) and p38 MAPKs (Kumar et al., 2018; Kuzmanic et al., 2017) also undergo reverse allosteric modulation and ATP-competitors can enhanced or block docking interactions.

Mechanistically, we have found no evidence in our crystal structures supporting that NC-p38i bind to additional sites other than the ATP-pocket. In fact, the above examples would support the rearrangements observed in p38α. Nevertheless, comparison of our two structures suggests that compound 37 induces similar changes independently of whether it is bound below the P-loop or not (Figure 33). These findings led us to speculate that the observed changes may not be only caused by this binding mode, and we favour the idea that NC-p38i might bind to other sites.

Several examples in the literature show that targeting the N-terminal domain of a kinase also affects its active site and further its activity. This inhibitory mechanism is observed in compounds binding to the PIF-pocket of AGC kinases such as of PDK1 (Engel et al., 2006b), PLK1 (Raab et al., 2018) and PKCζ (Lopez-Garcia et al., 2011). Another study shows that the MAP2K protein MKK7, an upstream activator of JNK, contains an allosteric site located at the top of the N-lobe where the type-I inhibitor ibrutinib can bind (Schroder et al 2020). Interestingly, recent data show that small-molecules intended to bind to the non-canonical site of p38α, which were obtained from a fragment-based crystal screening, can also bind to its N-terminal region (Nichols et al., 2020). For instance, an admantanol-derived fragment (KCL615) binds to three different sites on p38α, including (1) the non-canonical site (L243 and L222) but also (2) the ED site (D161), and (3) the β2-strand (N26 and S28) (PDB:6SPL). On the other hand, the fragment KCL802 binds to two pockets: (1) the non-canonical site (T218 through a DMSO molecule) and (2) a pocket between β2L0 and β1- β4 (D88 and T91) (PDB:6SP9).

The 2D $^{1}H,^{15}N$-TROSY spectrum of [$^{2}H,^{15}N$]p38α incubated with compound 38 shows that amino acids E19, R23, S28, S32, T91 at the N-lobe are specifically affected by its binding (Figure 29). Although the crystal structure of p38α:TAB1 complex shows some displacements of these residues, specially S28 and S32, we hypothesise that NC-p38i might bind to this N-terminal region and block the allosteric effect triggered by TAB1 (Figure 30). We are currently performing a global analysis combining different *in silico* approaches such as Fpocket (Le Guilloux et al., 2009) and SiteMap (Halgren, 2009) in order to determine the most likely sites of NC-p38i binding and further understand their mechanism of action. Importantly, preliminary analysis has identified a putative binding site at the N-terminal domain similar to that described for the KCL802 fragment (Figure 56). Additional simulations also suggest that amino acids K15, R23, K45 and R94 could be involved in the binding of NC-p38i to the N-terminal domain of p38α, which would correlate with the chemical shifts observed by NMR.

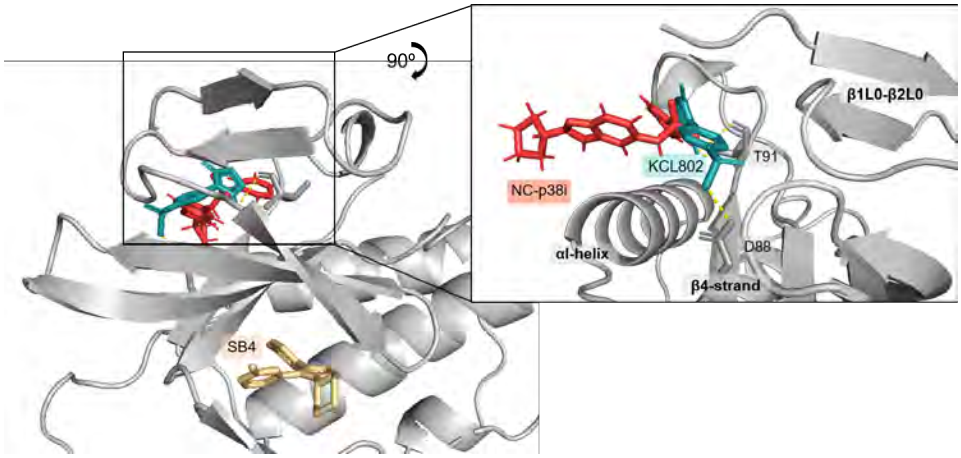

Figure 56. Putative binding site of NC-p38i at the N-terminal domain of p38α. Figure showing one of the predicted binding sites of NC-p38i at the N-lobe of p38α obtained from a computational ligand-binding method (Colizzi *et al.* 2021, *manuscript in preparation*) exploring the configurational space with enhanced-sampling molecular dynamics simulations in explicit water. p38α structures used in this study come from (Kuzmanic et al., 2017). Ligands and important residues are indicated in sticks and different colours: p38α (grey), NC-p38i (red), KCL802 (green), and SB220025 (SB4, orange).

We have shown that NC-p38i are able to inhibit at high concentrations the spontaneous p38β autophosphorylation. We propose that S28R, T44A, T218Q, H228Y and F270L may be responsible for the dramatic decrease of NC-p38i activity towards p38β (Figure 46). To decipher the importance of these residues, we plan to perform *in vitro* autophosphorylation assays using proteins in which those amino acids have been swapped between p38α and p38β by site-directed

mutagenesis.

The observation that compound 37 can access the active site of p38α, raises the question of what type of kinase inhibitors NC-p38i are. Based on their binding properties and biophysical data, they do not behave as type-I orthosteric inhibitors. Conversely, structural data show that they do not bind to the deep allosteric pocket near the ATP-site, meaning that they cannot be classified as type-II or type-III inhibitors. Ongoing experiments will validate whether NC-p38i are type-IV inhibitors.

In summary, our data identify NC-p38i as allosteric inhibitors of p38α that can modulate its conformation and interfere with its kinase catalytic activity. More research is clearly needed to better understand the binding mode of NC-p38i, but our results provide an initial framework into the molecular basis of a novel type of p38α inhibitors.

2. Therapeutic relevance of targeting p38α with NC-p38i

Non-canonical TAB1-induced p38α activation has been described to be restricted to specific stimuli, mainly in cardiomyocytes and endothelial cells. Inhibition of this pathway could be useful to treat cardiovascular diseases, by precisely targeting cardiomyocyte death and vascular leakage. We first observed NC-p38i compounds can inhibit non-canonical p38α activation in cells overexpressing myc-p38α and GFP-TAB1 (Figure 16). We also determined the compounds 37 and 38 significantly decrease SIR-induced H9c2 cell death both under prophylactic and therapeutic conditions (Figure 37A). These results are promising but *in vivo* experiments in rodents are critical to evaluate the clinical potential of NC-p38i.

The effect of NC-p38i in H9c2 cells was compared with the activity of SB203580, a commonly used p38α inhibitor in cell-based to address the role p38α in cardiomyocyte death (Kumphune et al., 2012). However, the beneficial effect of this ATP-competitor does not have a straight-forward interpretation due to its well-known off-target effects (Karaman et al., 2008). In contrast, compounds 37 and 38 mainly inhibit p38α (Figure 45). Hence, our results support that specific inhibition of p38α protects cardiomyocytes against SIR stimuli. Unfortunately, we had difficulties detecting p38α phosphorylation in H9c2 cells treated with only simulated ischaemia. Thus, following the ischaemic period, cells were subjected to additional 15 min of reperfusion under normoxic conditions. Whereas treatment with NC-p38i reduced the phosphorylation of TAB1 and HSP27, we do

not observe a reduction of p38α phosphorylation in these cells (Figure 37B). This could be explained by the upregulation of feedback loops during reperfusion, which mitigates p38α inhibition (De Nicola et al., 2018). On the other hand, there is evidence implicating ROS-induced ASK1 activation in the canonical activation of p38α during ischaemia-reperfusion (Meijles et al., 2020). In fact, we cannot rule out that the two mechanisms might cooperate in the phenotype observed in H9c2 cells. This could be analysed by using siRNAs to MKK3, the major p38α canonical activator in these cells (Figure 37C), and then test the effect of NC-p38i on p38α autophosphorylation.

Cardiotoxicity is a major side effect of cancer patients treated with anthracyclines (Brown et al., 2015). To further expand possible uses of NC-p38i, we investigated whether NC-p38i could impair doxorubicin-induced cardiomyocyte death. We observed that compound 38 might have a cardioprotective role against doxorubicin-induced toxicity in hiPSC-CM cells (Figure 42). The results suggest that NC-p38i may be active for short time points in cultured cells, as the effect was only observed at 24 h. Therefore, it would be interesting to repeat these experiments adding fresh NC-p38i every day and investigate if they protect cells against sustained doxorubicin damage. Importantly, the beneficial effect of the compound 38 was confirmed *in vivo* using zebrafish embryos (Figures 44).

These promising data support the interest in performing additional experiments to address the implication of p38α autophosphorylation in anthracycline-induced cardiomyocyte death. We hypothesise that both the canonical and non-canonical pathways may coexist in the same cell, and understanding their individual relevance would help to mitigate cardiomyocyte irreversible damage. In addition to p38α activation, doxorubicin also induces mitochondrial damage, dysregulation of Ca^{2+} metabolism and formation of double-strand DNA breaks in cardiomyocytes (Ma et al., 2020). To further validate the cardioprotective effect of NC-p38i on anthracycline-induced toxicity, the mitochondrial transmembrane potential can be measured by TMRE staining in hiPSC-CMs treated with doxorubicin (Crowley et al., 2016) as a read out of mitochondrial dysfunction. In addition, calcium-sensitive fluorescent probes such as Fluo-4 AM and γ-H2AX staining can be used to monitor the changes in the intracellular Ca^{2+} levels and in DNA damage, respectively (Maillet et al., 2016).

We have shown that NC-p38i efficiently inhibit *in vitro* spontaneous p38α autophosphorylation, in addition to that induced by TAB1. Hence, we hypothesize that these compounds may impair p38α autophosphorylation in other settings such as in T-cells. The TCR stimulation promotes p38α phosphorylation on Y323 by ZAP70, which leads to p38α autoactivation. This activation mechanism has

been reported to disrupt the hydrophobic core formed by Y69, F327, and W337 (Avitzour et al., 2007; Canagarajah et al., 1997; Diskin et al., 2007). We have not observed any change in the conformation of the aforementioned residues in our crystal structures (Figure 57), suggesting that NC-p38i might alter neither Y323 phosphorylation nor the subsequent conformational changes. Regardless, NC-p38i might impair the subsequent autoactivation of p38α by effecting the ATP-site. We posit that NC-p38i compounds may diminish the hyperactivation of this pathway in specific scenarios such us in tumours highly infiltrated with p38α-Y323^{+} CD4^{+} T-cells (Alam et al., 2015). Additional *in vitro* experiments should be performed in cultured CD4^{+} T lymphocytes to investigate the impact of NC-p38i in ZAP70-induced p38α activation and in the production of proinflammatory cytokines. As a control, the combination of PMA plus ionomycin could be used to activate the canonical MAP2K dependent pathway on these cells (Ai et al., 2013; Alam et al., 2014). Interestingly, a differential substrate specificity has been reported between the two pathways (Mittelstadt et al., 2009).

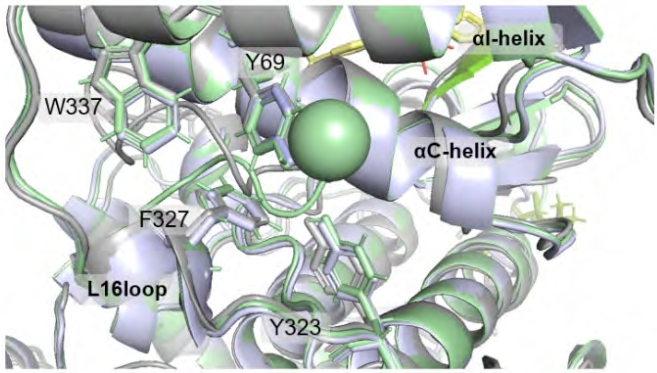

Figure 57. NC-p38i might not impair p38α phosphorylation by ZAP70 in T-cells. Superimposition of p38α structures crystallized in presence of SB203580 and compound 37 (Figure 30) with a p38α:SB203580 control complex (grey, PDB:1A9U).

3. Future perspectives of NC-p38i

As novel therapeutic candidates, a potential drawback of NC-p38i lies in their low residence time. Importantly, the target residence time associated with a kinase inhibitor is a predictor of its biological activity in terms of the target engagement *in vivo* rather than correlating with its inhibitory potency (Lu et al., 2018; Willemsen-Seegers et al., 2017). Additional *in silico* studies are key to figure out the binding mode of NC-p38i and optimize the binding affinity of these compounds,

so the life-time of the NC-p38i:p38α complex can be improved.

The lack of selectivity of many p38α inhibitors tested in clinical trials has been associated to random interference with other signalling pathways (Kumar et al., 2018). It appears that allosteric NC-p38i compounds might overcome this issue. The kinase selectivity panel that we used only contains 97 out the 518 human kinases reported. It has been recently shown that p38 inhibitors such as SB220025, VX-702 and SFK-86002 can efficiently inhibit NLK *in vitro* (Wang et al., 2021). Since this protein was not present in our screening, it would be important to investigate the NC-p38i effect on NLK.

Emerging evidence suggest that a kinase selectivity profiling is not sufficient to predict *in vivo* toxicity. In fact, the majority of human kinases still lack selective inhibitors. Thus, chemical proteomic approaches have been proposed to overcome this problem and obtain a detailed profile of drug targets in complex proteomes (Lanning et al., 2014). For instance, activity-based protein profiling (ABPP) is a great technique to understand the interaction mechanisms between chemical compounds and their targets in a genome wide scale in specific physiological and pathological processes. This approach uses small-molecule probes consisting on the compound of interest linked to a reporter group, either fluorescent groups or other components (biotin, alkynes or azide) that can be modified to be visualized. The probe then used to identify target proteins by gel-based or quantitative approaches (label-free, iTRAQ, SILAC). These experiments allow to study many other enzymes, in addition to kinases (Wang et al 2018), which might provide better correlation with the side effects that systemic administration of a kinase inhibitor may cause. These methods are used for covalent or high-affinity inhibitors, and we would need to optimize the binding affinity of NC-p38i to be able to perform proteome-wide experiments.

Treatment with NC-p38i for 72h do not show significant acute toxicity neither in cultured cells up to 30 μM nor in rats up to 50 mg/kg (Figure 54). Therefore, we extrapolate that NC-p38i have a safety profile as a single dose regimen. *In vivo* repetitive dosing experiments followed by histological examination of the tissues from treated animals should be performed to further validate these observations.

Another potential disadvantage of NC-p38i lies in their *in vitro* metabolism. Surprisingly, they are more rapidly metabolized by rat microsomes than in the human counterparts (Figure 51). Since the two synthesized fluorinated derivatives of compound 38 do not have not increased stability in rat microsomes (Figure 52), elucidation of the generated metabolites would give us novel chemical structures, which could be synthesized and tested *in vitro* to calculate their remaining

inhibitory activity. This information is of great importance for planning further experiments in rodents and choosing the administration route in order to delay the hepatic metabolism of NC-p38i.

Overall, our results support the notion that NC-p38i compounds are novel and specific p38α inhibitors, which serve as a good starting point to develop clinical candidates for treating non-canonical p38α signalling associated diseases.

CONCLUSIONS

1. We have identified new chemical compounds (NC-p38i) that inhibit TAB1-induced and spontaneous p38α autophosphorylation *in vitro*.

2. NC-p38i do not inhibit canonical MAP2K-dependent p38α activation but partially impair the ability of p38α to phosphorylate substrates.

3. NC-p38i probably bind to several sites on p38α but do not interfere with its interaction with TAB1.

4. NC-p38i interaction disturbs the ATP-binding site of p38α and its prone-to-autophosphorylate conformation.

5. NC-p38i reduce ischaemia-reperfusion-induced cardiomyocyte death, and doxorubicin-induced cardiac toxicity in several models, suggesting a cardio-protective effect.

SUPPLEMENTARY MATERIAL

Supplementary Figure 1. Structure of compounds that inhibit >80% TAB1-induced p38α autophosphorylation at ≥10 μM.

Compound 27

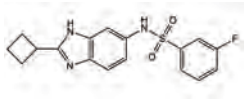

Compound E2.8

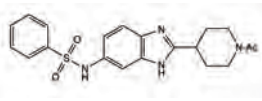

Compound IRB-001

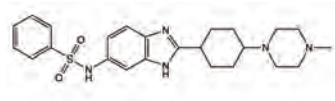

Compound 37

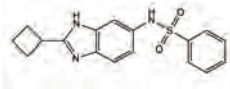

Compound A01

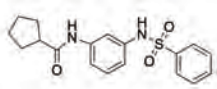

Compound IRB-002

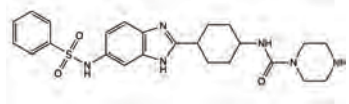

Compound 38

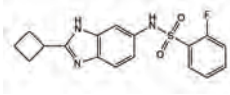

Compound A02

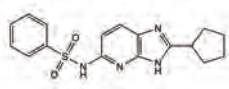

Compound IRB-003

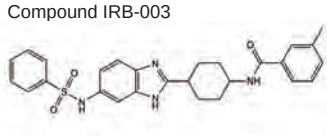

Compound 39

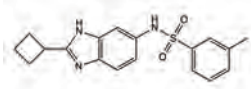

Compound A06

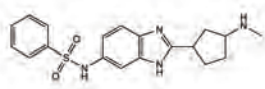

Compound IRB-4.3

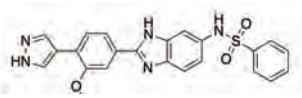

Compound 42

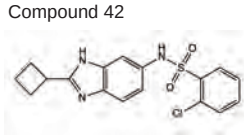

Compound A06a

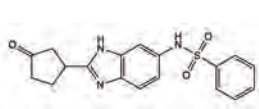

Compound IRB-111

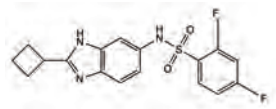

Compound 60

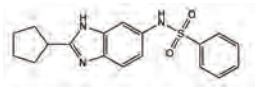

Compound A07

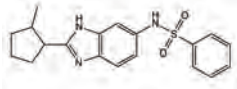

Compound IRB-112

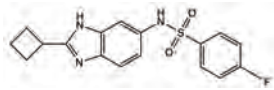

Compound E2.2

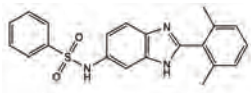

Compound A08

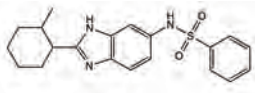

Compound IRB-004_2

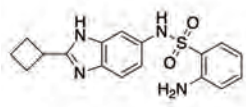

Compound E2.3

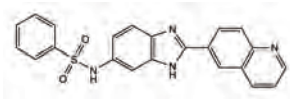

Compound A10

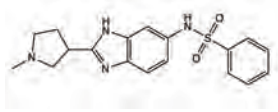

Supplementary Table 1. Crystallization, data collection and refinement statistics.

	Crystal B2X4_03	Crystal B2X14_07
Crystallization conditions		
Protein content	p38α + compound 37 + SB203580 (1mM)	p38α + compound 37 + SB203580 (1mM)
Screening	Proplex B11	TOP96 E2
Ratio p38α:C37	1:1.5	1:1.5
Crystallization condition	0.1 M HEPES pH 7, 15% w/v PEG400	25% w/v PEG350
Temperature	15 days at 4°C, then moved to 20°C	15 days at 4°C, then moved to 20°C
Cryobuffer	10% glycerol	10% glycerol
Data collection		
Beamline	BL13-Xaloc (Alba)	BL13-Xaloc (Alba)
Wavelenght	0.9792 Å	0.9792 Å
Detector	Pilatus 6M	Pilatus 6M
Temperature	100K	100K
Images	900	1200
Oscillation angle	0.2°/image	0.15°/image
Exposure	0.1s	0.09s
Distance	432.06 mm	359.69 mm
Resolution	2.2 Å	1.9 Å
Structure process, resolution and refinement (highest resolution shell in parentheses)		
Indexing program	Imosflm (CCP4)	AutoPROC
Resolution range	78.02-2.60 (2.74-2.60) Å	41.5-1.71 (1.771- 1.71) Å
Multiplicity	5.7 (5.9)	2.0
Rmerge	0.108 (0.495)	0.01584 (0.1962)
Completeness	100% (100%)	99.96 (99.95)
Mosaicity	0.75°	?

I/σ(I)	78.02 - 2.60 (2.74 - 2.60) Å	41.5 - 1.71 (1.771 - 1.71)
Wilson B factor ($Å^{-2}$)	5.7 (5.9)	2.0
Spacegroup	$P2_12_12_1$	$P2_12_12_1$
Cell (α=β=γ=90°)	a=65.41Å b=74.49Å c=78.02Å	a=65.0583 b=74.5683 c=77.9394
Solution Method	Molecular replacement	Molecular replacement
Program	Phaser (CCP4)	Phenix and Phaser
Model	4LOO	4LOO
LLG, TFZ	1822, 38.9	2095, 37.6
Refinement program	Refmac5	Phenix.refine, PDB-REDO
R, RF	0.22, 0.34	0.20, 0.23
RMS bonds	0.006	0.017
RMS angles	1.625°	2.618°
RMS chiral	0.122°	0.232°
<B>	53.3 $Å^2$	35.90 $Å^2$
Ramachandran		
Favoured	300 (86.21%)	95.47%
Outliers	17 (4.89%)	0%
Number of residues refined	314	335
Number of water molecules	31	232
Other molecules	SB203580, C37	SB203580
Presence of disulfide bond C119-C162	Yes	Yes

Supplementary Figure 2. |Fo|-|Fc| omitted electron density maps of p38α:SB203580 (B2X14_07) and p38α:SB203580:C37 (B2X4_03) crystals. (**A**) Manual fit of SB203580 ligand in the p38α:SB203580 (B2X14_07) crystal after molecular refinement. (**B**) Density map corresponding to compound 37 (green density) around SB203580 in the p38α:SB203580:C37 (B2X4_03) crystal. Note that the P-loop formed by β1-β2 strands is highly mobile (red and absence of density). (**C**) Difference map corresponding to the "in" conformation of the Y35 residue in the p38α:SB203580 (B2X14_07) crystal. (**D**) Difference map corresponding to the mobile Y35 residue in the p38α:SB203580:C37 (B2X14_07) crystal suggesting an "out" conformation. (**E**) Difference map of the mobile A-loop from the p38α:SB203580:C37 (B2X14_07) crystal. Note that there is a strong signal right after the D168 and F169. Then, the following residues are poorly visible.

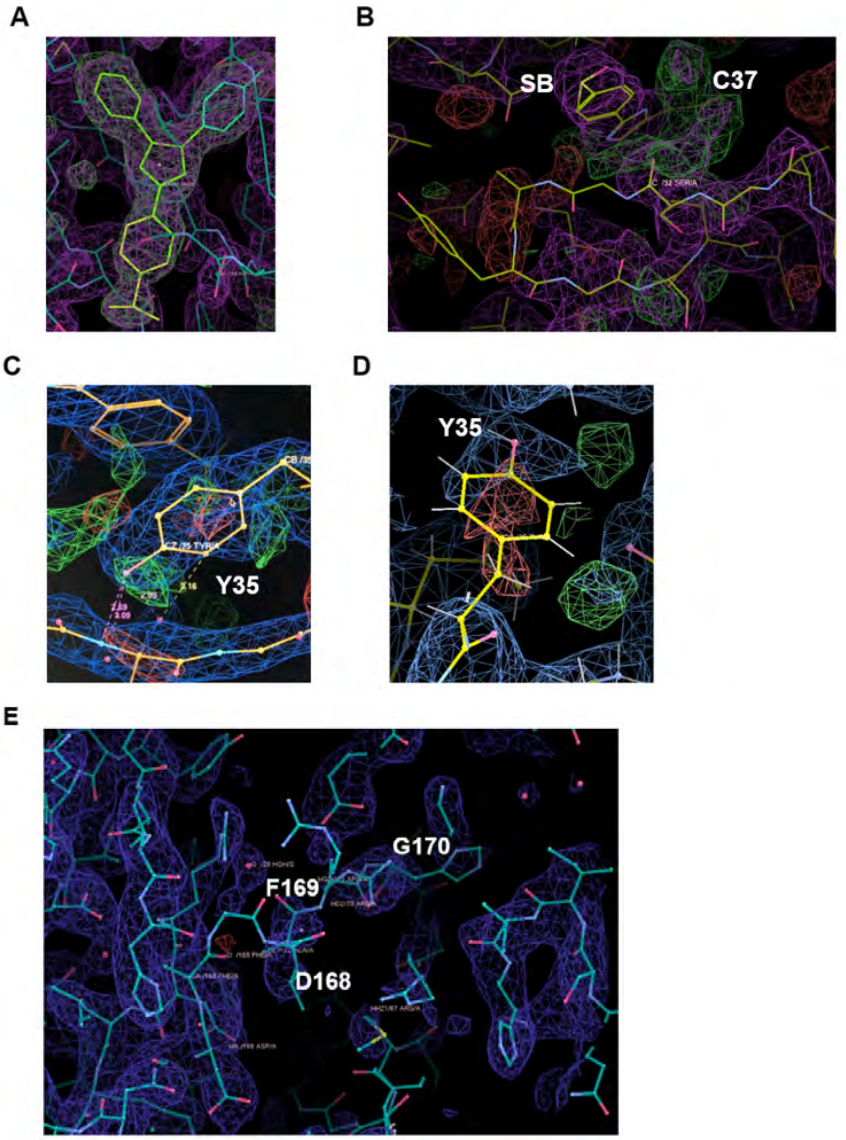

Supplementary Table 2. Kinase selectivity of compounds 37 and 38. Compounds 37 and 38 were tested on a panel of 97 human kinases. Results are shown as the mean of n=1 experiment in duplicates. Kinases inhibited >25% are in bold.

Protein kinase	Compound 37 (10 μM)	Compound 38 (10 μM)
ABL1	0	3
ACVR1B (ALK4)	12	-6
ADRBK1 (GRK2)	13	1
AKT1 (PKB alpha)	-1	0
AKT2 (PKB beta)	-13	2
ALK	12	8
AMPK (A1/B2/G2)	4	3
AURKA (Aurora A)	3	2
AURKB (Aurora B)	-10	-1
AXL	3	-2
BRAF	7	9
BTK	10	0
CAMK2A (CaMKII alpha)	-2	2
CDC42 BPA (MRCKA)	-15	1
CDK1/cyclin B	5	0
CDK17/cyclin Y	8	6
CDK2/cyclin A	8	2
CDK5/p25	-2	1
CHEK1 (CHK1)	-2	-3
CHEK2 (CHK2)	2	2
CSF1R (FMS)	10	1
CSNK1D (CK1 delta)	4	5
DCAMKL1 (DCLK1)	-7	0
DNA-PK	21	12
DYRK1B	1	5
EGFR (ErbB1)	3	-5
EPHA2	8	3

ERBB2 (HER2)	-3	-3
ERBB4 (HER4)	8	6
FGFR1	0	0
FGFR2	9	10
FGFR3	11	-2
FLT1 (VEGFR1)	7	1
FLT3	13	3
FRAP1 (mTOR)	-2	2
GRK4	-10	0
GSK3B (GSK3 beta)	0	0
HIPK3 (YAK1)	-3	6
IGF1R	19	7
IKBKB (IKK beta)	4	2
IKBKE (IKK epsilon)	13	4
INSR	2	0
IRAK4	0	-2
JAK1	-2	-3
KDR (VEGFR2)	3	0
KIT	-11	-3
LCK	8	11
MAP2K1 (MEK1)	17	2
MAP2K2 (MEK2)	4	3
MAP2K6 (MKK6)	-3	7
MAP3K8 (COT)	31	7
MAP3K9 (MLK1)	-9	1
MAP4K2 (GCK)	-1	5
MAPK1 (ERK2)	9	3
MAPK10 (JNK3)	7	5
MAPK11 (p38 beta)	41	28
MAPK12 (p38 gamma)	13	8
MAPK13 (p38 delta)	4	2

MAPK14 (p38 alpha) Direct	68	52
MAPK14 (p38 alpha)	78	64
MAPK3 (ERK1)	3	8
MAPK7 (ERK5)	13	21
MAPK8 (JNK1)	15	0
MAPK9 (JNK2)	-20	6
MAPKAPK2	-1	2
MAPKAPK5 (PRAK)	3	5
MARK3	-4	0
MET (cMet)	-3	-1
MKNK1 (MNK1)	-2	-3
NEK1	-10	2
NTRK1 (TRKA)	8	8
PAK1	10	0
PAK4	-1	2
PDGFRA (PDGFR alpha)	8	-1
PDGFRB (PDGFR beta)	7	0
PDK1	7	4
PIM1	0	0
PIM2	-5	-1
PIM3	8	-1
PLK1	14	3
PRKACA (PKA)	-10	-3
PRKCA (PKC alpha)	4	6
PRKCE (PKC epsilon)	-3	2
PTK2 (FAK)	10	4
RAF1 (cRAF) Y340D Y341D	-3	4
RET	3	5
ROCK1	0	0
RPS6KA2 (RSK3)	-2	-1
RPS6KA5 (MSK1)	5	0

RPS6KB1 (p70S6K)	-7	6
SRC	9	3
SRPK1	0	5
TAOK2 (TAO1)	4	-4
TEK (Tie2)	-2	2
TYK2	-1	3
YES1	6	6
ZAP70	14	-1

REFERENCES

Berridge, M.J. (2014) Cell Signalling Biology; doi:10.1042/csb0001002

Adam, K., and Hunter, T. Histidine kinases and the missing phosphoproteome from prokaryotes to eukaryotes. Lab Invest. 2018 Feb;98(2):233-247.

Adamcova, M., Skarkova, V., Seifertova, J., and Rudolf, E. Cardiac Troponins are Among Targets of Doxorubicin-Induced Cardiotoxicity in hiPCS-CMs. Int J Mol Sci. 2019 May 29;20(11):2638

Adams, R.H., Porras, A., Alonso, G., Jones, M., Vintersten, K., Panelli, S., Valladares, A., Perez, L., Klein, R., and Nebreda, A.R. Essential role of p38alpha MAP kinase in placental but not embryonic cardiovascular development. Mol cell. 2000 Jul;6(1):109-16.

Ai, W., Li, H., Song, N., Li, L., and Chen, H. Optimal method to stimulate cytokine production and its use in immunotoxicity assessment. Int J Environ Res Public Health. 2013 Aug 27;10(9):3834-42.

Alam, M.S., Gaida, M.M., Bergmann, F., Lasitschka, F., Giese, T., Giese, N.A., Hackert, T., Hinz, U., Hussain, S.P., Kozlov, S.V., *et al.* Selective inhibition of the p38 alternative activation pathway in infiltrating T cells inhibits pancreatic cancer progression. Nat Med. 2015 Nov;21(11):1337-43.

Alam, M.S., Gaida, M.M., Ogawa, Y., Kolios, A.G., Lasitschka, F., and Ashwell, J.D. Counter-regulation of T cell effector function by differentially activated p38. J Exp Med. 2014 Jun 2;211(6):1257-70.

Alonso, G., Ambrosino, C., Jones, M., and Nebreda, A.R. Differential activation of p38 mitogen-activated protein kinase isoforms depending on signal strength. J Biol Chem. 2000 Dec 22;275(51):40641-8.

Allen, M., Svensson, L., Roach, M., Hambor, J., McNeish, J., and Gabel, C.A. Deficiency of the stress kinase p38alpha results in embryonic lethality: characterization of the kinase dependence of stress responses of enzyme-deficient embryonic stem cells. J Exp Med. 2000 Mar 6;191(5):859-70.

Andrews, C., Ho, P.D., Dillmann, W.H., Glembotski, C.C., and McDonough, P.M. The MKK6-p38 MAPK pathway prolongs the cardiac contractile calcium transient, downregulates SERCA2, and activates NF-AT. Cardiovasc Res. 2003 Jul 1;59(1):46-56.

Arabacilar, P., and Marber, M. The case for inhibiting p38 mitogen-activated protein kinase in heart failure. Front Pharmacol. 2015 May 12;6:102.

Ashraf, M.I., Ebner, M., Wallner, C., Haller, M., Khalid, S., Schwelberger, H., Koziel, K., Enthammer, M., Hermann, M., Sickinger, S., *et al.* A p38MAPK/MK2 signaling pathway leading to redox stress, cell death and ischemia/reperfusion injury. Cell Commun Signal. 2014 Jan 14;12:6.

Avitzour, M., Diskin, R., Raboy, B., Askari, N., Engelberg, D., and Livnah, O. Intrinsically active variants of all human p38 isoforms. FEBS J. 2007 Feb;274(4):963-75.

Bartels, C., Xia, T.H., Billeter, M., Guntert, P., and Wuthrich, K. The program XEASY for computer-supported NMR spectral analysis of biological macromolecules. J Biomol NMR. 1995 Jul;6(1):1-10.

Batool, M., Ahmad, B., and Choi, S. A Structure-Based Drug Discovery Paradigm. Int J Mol Sci. 2019 Jun 6;20(11):2783.

Battye, T.G., Kontogiannis, L., Johnson, O., Powell, H.R., and Leslie, A.G. iMOSFLM: a new graphical interface for diffraction-image processing with MOSFLM. Acta Crystallogr D Biol Crystallogr. 2011 Apr;67(Pt 4):271-81.

Beenstock, J., Mooshayef, N., and Engelberg, D. How Do Protein Kinases Take a Selfie (Autophosphorylate)? Trends Biochem Sci. 2016 Nov;41(11):938-953.

Ben-Levy, R., Leighton, I.A., Doza, Y.N., Attwood, P., Morrice, N., Marshall, C.J., and Cohen, P. Identification of novel phosphorylation sites required for activation of MAPKAP kinase-2. EMBO J. 1995 Dec 1;14(23):5920-30.

Brien, P., Pugazhendhi, D., Woodhouse, S., Oxley, D., and Pell, J.M. p38alpha MAPK regulates adult muscle stem cell fate by restricting progenitor proliferation during postnatal growth and repair. Stem Cells. 2013 Aug;31(8):1597-610.

Brown, S.A., Sandhu, N., and Herrmann, J. Systems biology approaches to adverse drug effects: the example of cardio-oncology. Nat Rev Clin Oncol. 2015 Dec;12(12):718-31.

Buja, L.M. Myocardial ischemia and reperfusion injury. Cardiovasc Pathol. 2005 Jul-Aug;14(4):170-5.

Burridge, P.W., Li, Y.F., Matsa, E., Wu, H., Ong, S.G., Sharma, A., Holmstrom, A., Chang, A.C., Coronado, M.J., Ebert, A.D., *et al.* Human induced pluripotent stem cell-derived cardiomyocytes recapitulate the predilection of breast cancer patients to doxorubicin-induced cardiotoxicity. Nat Med. 2016 May;22(5):547-56.

Calienni, M.N., Cagel, M., Montanari, J., Moretton, M.A., Prieto, M.J., Chiappetta, D.A., and Alonso, S.D.V. Zebrafish (Danio rerio) model as an early stage screening tool to study the biodistribution and toxicity profile of doxorubicin-loaded mixed micelles. Toxicol Appl Pharmacol. 2018 Oct 15;357:106-114.

Canagarajah, B.J., Khokhlatchev, A., Cobb, M.H., and Goldsmith, E.J. Activation mechanism of the MAP kinase ERK2 by dual phosphorylation. Cell. 1997 Sep 5;90(5):859-69.

Canovas, B., Igea, A., Sartori, A.A., Gomis, R.R., Paull, T.T., Isoda, M., Perez-Montoyo, H., Serra, V., Gonzalez-Suarez, E., Stracker, T.H., *et al.* Targeting p38alpha Increases DNA Damage, Chromosome Instability, and the Anti-tumoral Response to Taxanes in Breast Cancer Cells. Cancer Cell. 2018 Jun 11;33(6):1094-1110.e8.

Canovas, B., and Nebreda, A.R. Diversity and versatility of p38 kinase signalling in health and disease. Nat Rev Mol Cell Biol. 2021 May;22(5):346-366.

Cardin, S., Li, D., Thorin-Trescases, N., Leung, T.K., Thorin, E., and Nattel, S. Evolution of the atrial fibrillation substrate in experimental congestive heart failure: angiotensin-dependent and -independent pathways. Cardiovasc Res. 2003 Nov 1;60(2):315-25.

Cargnello, M., and Roux, P.P. Activation and function of the MAPKs and their substrates, the MAPK-activated protein kinases. Microbiol Mol Biol Rev. 2011 Mar;75(1):50-83.

Casar, B., Sanz-Moreno, V., Yazicioglu, M.N., Rodriguez, J., Berciano, M.T., Lafarga, M., Cobb, M.H., and Crespo, P. Mxi2 promotes stimulus-independent ERK nuclear translocation. EMBO J. 2007 Feb 7;26(3):635-46.

Casper, D., Bukhtiyarova, M., and Springman, E.B. A Biacore biosensor method for detailed kinetic binding analysis of small molecule inhibitors of p38alpha mitogen-activated protein kinase. Anal Biochem. 2004 Feb 1;325(1):126-36.

Clark, J.E., Sarafraz, N., and Marber, M.S. Potential of p38-MAPK inhibitors in the treatment of ischaemic heart disease. Pharmacol Ther. 2007 Nov;116(2):192-206.

Comess, K.M., Sun, C., Abad-Zapatero, C., Goedken, E.R., Gum, R.J., Borhani, D.W., Argiriadi, M., Groebe, D.R., Jia, Y., Clampit, J.E., *et al.* Discovery and characterization of non-ATP site inhibitors of the mitogen activated protein (MAP) kinases. ACS Chem Biol. 2011 Mar 18;6(3):234-44.

Conner, S.H., Kular, G., Peggie, M., Shepherd, S., Schuttelkopf, A.W., Cohen, P., and Van Aalten, D.M. TAK1-binding protein 1 is a pseudophosphatase. Biochem J. 2006 Nov 1;399(3):427-34.

Coulombe, P., and Meloche, S. Atypical mitogen-activated protein kinases: structure, regulation and functions. Biochim Biophys Acta. 2007 Aug;1773(8):1376-87.

Coulthard, L.R., White, D.E., Jones, D.L., McDermott, M.F., and Burchill, S.A. p38(MAPK): stress responses from molecular mechanisms to therapeutics. Trends Mol Med. 2009 Aug;15(8):369-79.

Crowley, L.C., Christensen, M.E., and Waterhouse, N.J. Measuring Mitochondrial Transmembrane Potential by TMRE Staining. Cold Spring Harb Protoc. 2016 Dec 1;2016(12).

Cuadrado, A., and Nebreda, A.R. Mechanisms and functions of p38 MAPK signalling. Biochem J. 2010 Aug 1;429(3):403-17.

Chang, C., Wu, S.L., Zhao, X.D., Zhao, C.T., and Li, Y.H. Developmental toxicity of doxorubicin hydrochloride in embryo-larval stages of zebrafish. Biomed Mater Eng. 2014;24(1):909-16.

Chen, M.J., Dixon, J.E., and Manning, G. Genomics and evolution of protein phosphatases. Sci Signal. 2017 Apr 11;10(474):eaag1796.

Chen, T., and Vunjak-Novakovic, G. In vitro Models of Ischemia-Reperfusion Injury. Regen Eng Transl Med. 2018 Sep;4(3):142-153.

Cheng, X., and Jiang, H. Allostery in Drug Development. Adv Exp Med Biol. 2019;1163:1-23.

Cheung, P.C., Campbell, D.G., Nebreda, A.R., and Cohen, P. Feedback control of the protein kinase TAK1 by SAPK2a/p38alpha. EMBO J. 2003 Nov 3;22(21):5793-805.

Davidson, W., Frego, L., Peet, G.W., Kroe, R.R., Labadia, M.E., Lukas, S.M., Snow, R.J., Jakes, S., Grygon, C.A., Pargellis, C., *et al.* Discovery and characterization of a substrate selective p38alpha inhibitor. Biochemistry. 2004 Sep 21;43(37):11658-71.

De Nicola, G.F., Bassi, R., Nichols, C., Fernandez-Caggiano, M., Golforoush, P.A., Thapa, D., Anderson, R., Martin, E.D., Verma, S., Kleinjung, J., *et al.* The TAB1-p38alpha complex aggravates myocardial injury and can be targeted by small molecules. JCI Insight. 2018 Aug 23;3(16):e121144.

DeNicola, G.F., Martin, E.D., Chaikuad, A., Bassi, R., Clark, J., Martino, L., Verma, S., Sicard, P., Tata, R., Atkinson, R.A., *et al.* Mechanism and consequence of the autoactivation of p38alpha mitogen-activated protein kinase promoted by TAB1. Nat Struct Mol Biol. 2013 Oct;20(10):1182-90.

Dhawan, N.S., Scopton, A.P., and Dar, A.C. Small molecule stabilization of the KSR inactive state antagonizes oncogenic Ras signalling. Nature. 2016 Sep 1;537(7618):112-116.

Diskin, R., Engelberg, D., and Livnah, O. A novel lipid binding site formed by the MAP kinase insert in p38 alpha. J Mol Biol. 2008 Jan 4;375(1):70-9.

Diskin, R., Lebendiker, M., Engelberg, D., and Livnah, O. Structures of p38alpha active mutants reveal conformational changes in L16 loop that induce autophosphorylation and activation. J Mol Biol. 2007 Jan 5;365(1):66-76.

Dorn, G.W., 2nd, and Molkentin, J.D. Manipulating cardiac contractility in heart failure: data from mice and men. Circulation. 2004 Jan 20;109(2):150-8.

Du, C.S., Yang, R.F., Song, S.W., Wang, Y.P., Kang, J.H., Zhang, R., Su, D.F., and Xie, X. Magnesium Lithospermate B Protects Cardiomyocytes from Ischemic Injury Via Inhibition of TAB1-p38 Apoptosis Signaling. Front Pharmacol. 2010 Aug 24;1:111.

Emerling, B.M., Platanias, L.C., Black, E., Nebreda, A.R., Davis, R.J., and Chandel, N.S. Mitochondrial reactive oxygen species activation of p38 mitogen-activated protein kinase is required for hypoxia signaling. Mol Cell Biol. 2005 Jun;25(12):4853-62.

Emsley, P., Lohkamp, B., Scott, W.G., and Cowtan, K. Features and development of Coot. Acta Crystallogr D Biol Crystallogr. 2010 Apr;66(Pt 4):486-501.

Engel, F.B., Hsieh, P.C., Lee, R.T., and Keating, M.T. FGF1/p38 MAP kinase inhibitor therapy induces cardiomyocyte mitosis, reduces scarring, and rescues function after myocardial infarction. Proc Natl Acad Sci U S A. 2006 Oct 17;103(42):15546-51.

Engel, F.B., Schebesta, M., Duong, M.T., Lu, G., Ren, S., Madwed, J.B., Jiang, H., Wang, Y., and Keating, M.T. p38 MAP kinase inhibition enables proliferation of adult mammalian cardiomyocytes. Genes Dev. 2005 May 15;19(10):1175-87.

Engel, M., Hindie, V., Lopez-Garcia, L.A., Stroba, A., Schaeffer, F., Adrian, I., Imig, J., Idrissova, L., Nastainczyk, W., Zeuzem, S., *et al*. Allosteric activation of the protein kinase PDK1 with low molecular weight compounds. EMBO J. 2006 Nov 29;25(23):5469-80.

Espejo, M.S., Aiello, I., Sepulveda, M., Vila Petroff, M.G., Aiello, E.A., and De Giusti, V.C. The reduced myofilament responsiveness to calcium contributes to the negative force-frequency relationship in rat cardiomyocytes: role of reactive oxygen species and p-38 map kinase. Pflugers Arch. 2017 Dec;469(12):1663-1673.

Fedorov, O., Marsden, B., Pogacic, V., Rellos, P., Muller, S., Bullock, A.N., Schwaller, J., Sundstrom, M., and Knapp, S. A systematic interaction map of validated kinase inhibitors with Ser/Thr kinases. Proc Natl Acad Sci U S A. 2007 Dec 18;104(51):20523-8.

Fiedler, B., Feil, R., Hofmann, F., Willenbockel, C., Drexler, H., Smolenski, A., Lohmann, S.M., and Wollert, K.C. cGMP-dependent protein kinase type I inhibits TAB1-p38 mitogen-activated protein kinase apoptosis signaling in cardiac myocytes. J Biol Chem. 2006 Oct 27;281(43):32831-40.

Francis, D.M., Rozycki, B., Koveal, D., Hummer, G., Page, R., and Peti, W. Structural basis of p38alpha regulation by hematopoietic tyrosine phosphatase. Nat Chem Biol. 2011 Nov 6;7(12):916-24.

Ge, B., Gram, H., Di Padova, F., Huang, B., New, L., Ulevitch, R.J., Luo, Y., and Han, J. MAPKK-independent activation of p38alpha mediated by TAB1-dependent autophosphorylation of p38alpha. Science. 2002 Feb 15;295(5558):1291-4.

Ge, B., Xiong, X., Jing, Q., Mosley, J.L., Filose, A., Bian, D., Huang, S., and Han, J. TAB1beta (transforming growth factor-beta-activated protein kinase 1-binding protein 1beta), a novel splicing variant of TAB1 that interacts with p38alpha but not TAK1. J Biol Chem. 2003 Jan 24;278(4):2286-93.

Genovese, M.C. Inhibition of p38: has the fat lady sung? Arthritis Rheum. 2009 Feb;60(2):317-20.

Gibson, D.G., Young, L., Chuang, R.Y., Venter, J.C., Hutchison, C.A., 3rd, and Smith, H.O. Enzymatic assembly of DNA molecules up to several hundred kilobases. Nat Methods. 2009 May;6(5):343-5.

Gillespie, M.A., Le Grand, F., Scime, A., Kuang, S., von Maltzahn, J., Seale, V., Cuenda, A., Ranish, J.A., and Rudnicki, M.A. p38-{gamma}-dependent gene silencing restricts entry into the myogenic differentiation program. J Cell Biol. 2009 Dec 28;187(7):991-1005.

Gills, J.J., Castillo, S.S., Zhang, C., Petukhov, P.A., Memmott, R.M., Hollingshead, M., Warfel, N., Han, J., Kozikowski, A.P., and Dennis, P.A. Phosphatidylinositol ether lipid analogues that inhibit AKT also independently activate the stress kinase, p38alpha, through MKK3/6-independent and -dependent mechanisms. J Biol Chem. 2007 Sep 14;282(37):27020-27029.

Gomez-Gutierrez, P., Campos, P.M., Vega, M., and Perez, J.J. Identification of a Novel Inhibitory Allosteric Site in p38alpha. PLoS One. 2016 Nov 29;11(11):e0167379.

Grimsey, N.J., Aguilar, B., Smith, T.H., Le, P., Soohoo, A.L., Puthenveedu, M.A., Nizet, V., and Trejo, J. Ubiquitin plays an atypical role in GPCR-induced p38 MAP kinase activation on endosomes. J Cell Biol. 2015 Sep 28;210(7):1117-31.

Grimsey, N.J., Lin, Y., Narala, R., Rada, C.C., Mejia-Pena, H., and Trejo, J. G protein-coupled receptors activate p38 MAPK via a non-canonical TAB1-TAB2- and TAB1-TAB3-dependent pathway in endothelial cells. J Biol Chem. 2019 Apr 12;294(15):5867-5878.

Guo, R.M., Xu, W.M., Lin, J.C., Mo, L.Q., Hua, X.X., Chen, P.X., Wu, K., Zheng, D.D., and Feng, J.Q. Activation of the p38 MAPK/NF-kappaB pathway contributes to doxorubicin-induced inflammation and cytotoxicity in H9c2 cardiac cells. Mol Med Rep. 2013 Aug;8(2):603-8.

Guo, W., Liu, X., Li, J., Shen, Y., Zhou, Z., Wang, M., Xie, Y., Feng, X., Wang, L., and Wu, X. Prdx1 alleviates cardiomyocyte apoptosis through ROS-activated MAPK pathway during myocardial ischemia/reperfusion injury. Int J Biol Macromol. 2018 Jun;112:608-615.

Halgren, T.A. Identifying and characterizing binding sites and assessing druggability. J Chem Inf Model. 2009 Feb;49(2):377-89.

Hall, M.D., Yasgar, A., Peryea, T., Braisted, J.C., Jadhav, A., Simeonov, A., and Coussens, N.P. Fluorescence polarization assays in high-throughput screening and drug discovery: a review. Methods Appl

Fluoresc. 2016 Apr 28;4(2):022001.

Haller, V., Nahidino, P., Forster, M., and Laufer, S.A. An updated patent review of p38 MAP kinase inhibitors (2014-2019). Expert Opin Ther Pat. 2020 Jun;30(6):453-466.

Hammaker, D., and Firestein, G.S. "Go upstream, young man": lessons learned from the p38 saga. Ann Rheum Dis. 2010 Jan;69 (Suppl 1):i77-82.

Hanks, S.K., and Hunter, T. Protein kinases 6. The eukaryotic protein kinase superfamily: kinase (catalytic) domain structure and classification. FASEB J. 1995 May;9(8):576-96.

Hari, S.B., Merritt, E.A., and Maly, D.J. Conformation-selective ATP-competitive inhibitors control regulatory interactions and noncatalytic functions of mitogen-activated protein kinases. Chem Biol. 2014 May 22;21(5):628-35.

Hausenloy, D.J., and Yellon, D.M. Myocardial ischemia-reperfusion injury: a neglected therapeutic target. J Clin Invest. 2013 Jan;123(1):92-100.

He, X., Ni, D., Lu, S., and Zhang, J. Characteristics of Allosteric Proteins, Sites, and Modulators. J Clin Invest. 2013 Jan;123(1):92-100.

Herman, E.H., Lipshultz, S.E., Rifai, N., Zhang, J., Papoian, T., Yu, Z.X., Takeda, K., and Ferrans, V.J. (1998). Use of cardiac troponin T levels as an indicator of doxorubicin-induced cardiotoxicity. Cancer Res. 1998 Jan 15;58(2):195-7.

Hutsell, S.Q., Kimple, R.J., Siderovski, D.P., Willard, F.S., and Kimple, A.J. High-affinity immobilization of proteins using biotin- and GST-based coupling strategies. Methods Mol Biol. 2010;627:75-90.

Huynh, K., and Partch, C.L. Analysis of protein stability and ligand interactions by thermal shift assay. Curr Protoc Protein Sci. 2015 Feb 2;79:28.9.1-28.9.14.

Jacquet, S., Zarrinpashneh, E., Chavey, A., Ginion, A., Leclerc, I., Viollet, B., Rutter, G.A., Bertrand, L., and Marber, M.S. The relationship between p38 mitogen-activated protein kinase and AMP-activated protein kinase during myocardial ischemia. Cardiovasc Res. 2007 Dec 1;76(3):465-72.

Jiang, Y., Chen, C., Li, Z., Guo, W., Gegner, J.A., Lin, S., and Han, J. Characterization of the structure and function of a new mitogen-activated protein kinase (p38beta). J Biol Chem. 1996 Jul 26;271(30):17920-6.

Joosten, R.P., Long, F., Murshudov, G.N., and Perrakis, A. The PDB_REDO server for macromolecular structure model optimization. IUCrJ. 2014 May 30;1(Pt 4):213-20.

Jopling, C., Sune, G., Morera, C., and Izpisua Belmonte, J.C. p38alpha MAPK regulates myocardial regeneration in zebrafish. Cell Cycle. 2012 Mar 15;11(6):1195-201.

Juanhuix, J., Gil-Ortiz, F., Cuni, G., Colldelram, C., Nicolas, J., Lidon, J., Boter, E., Ruget, C., Ferrer, S., and Benach, J. Developments in optics and performance at BL13-XALOC, the macromolecular crystallography beamline at the ALBA synchrotron. J Synchrotron Radiat. 2014 Jul;21(Pt 4):679-89.

Kaikkonen, L., Magga, J., Ronkainen, V.P., Koivisto, E., Perjes, A., Chuprun, J.K., Vinge, L.E., Kilpio, T., Aro, J., Ulvila, J., *et al.* p38alpha regulates SERCA2a function. J Mol Cell Cardiol. 2014 Feb;67:86-93.

Kang, Y.J., Zhou, Z.X., Wang, G.W., Buridi, A., and Klein, J.B. Suppression by metallothionein of doxorubicin-induced cardiomyocyte apoptosis through inhibition of p38 mitogen-activated protein kinases. J Biol Chem. 2000 May 5;275(18):13690-8.

Karaman, M.W., Herrgard, S., Treiber, D.K., Gallant, P., Atteridge, C.E., Campbell, B.T., Chan, K.W., Ciceri, P., Davis, M.I., Edeen, P.T., *et al.* A quantitative analysis of kinase inhibitor selectivity. Nat Biotechnol. 2008 Jan;26(1):127-32.

Khiati, S., Dalla Rosa, I., Sourbier, C., Ma, X., Rao, V.A., Neckers, L.M., Zhang, H., and Pommier, Y. Mitochondrial topoisomerase I (top1mt) is a novel limiting factor of doxorubicin cardiotoxicity. Clin Cancer Res. 2014 Sep 15;20(18):4873-81.

Kim, L., Del Rio, L., Butcher, B.A., Mogensen, T.H., Paludan, S.R., Flavell, R.A., and Denkers, E.Y. p38 MAPK autophosphorylation drives macrophage IL-12 production during intracellular infection. J Immunol. 2005 Apr 1;174(7):4178-84.

Kornev, A.P., and Taylor, S.S. Dynamics-Driven Allostery in Protein Kinases. Trends Biochem Sci. 2015 Nov;40(11):628-647.

Krebs, E.G., and Fischer, E.H. The phosphorylase b to a converting enzyme of rabbit skeletal muscle. Biochim Biophys Acta. 1956 Apr;20(1):150-7.

Krebs, E.G., Graves, D.J., and Fischer, E.H. Factors affecting the activity of muscle phosphorylase b kinase. J Biol Chem. 1959; 234, 2867-2873.

Kumar, G.S., Clarkson, M.W., Kunze, M.B.A., Granata, D., Wand, A.J., Lindorff-Larsen, K., Page, R., and Peti, W. Dynamic activation and regulation of the mitogen-activated protein kinase p38. Proc Natl Acad Sci U S A 2018 May; 115 (18), 4655-4660.

Kumphune, S., Chattipakorn, S., and Chattipakorn, N. (2012). Role of p38 inhibition in cardiac ischemia/reperfusion injury. Eur J Clin Pharmacol. 2012 May;68(5), 513-524.

Kumphune, S., Surinkaew, S., Chattipakorn, S.C., and Chattipakorn, N. Inhibition of p38 MAPK activation protects cardiac mitochondria from ischemia/reperfusion injury. Pharm Biol. 2015; 53(12), 1831-1841.

Kuzmanic, A., Sutto, L., Saladino, G., Nebreda, A.R., Gervasio, F.L., and Orozco, M. Changes in the free-energy landscape of p38alpha MAP kinase through its canonical activation and binding events as studied by enhanced molecular dynamics simulations. Elife. 2017 Apr 26;6:e22175.

Kyoi, S., Otani, H., Matsuhisa, S., Akita, Y., Tatsumi, K., Enoki, C., Fujiwara, H., Imamura, H., Kamihata, H., and Iwasaka, T. Opposing effect of p38 MAP kinase and JNK inhibitors on the development of heart failure in the cardiomyopathic hamster. Cardiovasc Res. 2006 Mar 1;69(4):888-98.

Lanna, A., Henson, S.M., Escors, D., and Akbar, A.N. The kinase p38 activated by the metabolic regulator AMPK and scaffold TAB1 drives the senescence of human T cells. Nat Immunol. 2014 Oct;15(10):965-72.

Lanning, B.R., Whitby, L.R., Dix, M.M., Douhan, J., Gilbert, A.M., Hett, E.C., Johnson, T.O., Joslyn, C., Kath, J.C., Niessen, S., *et al.* A road map to evaluate the proteome-wide selectivity of covalent kinase inhibitors. Nat Chem Biol. 2014 Sep;10(9):760-767.

Le Guilloux, V., Schmidtke, P., and Tuffery, P. Fpocket: an open source platform for ligand pocket detection. BMC Bioinformatics. 2009 Jun 2;10:168.

Lee, J.C., Laydon, J.T., McDonnell, P.C., Gallagher, T.F., Kumar, S., Green, D., McNulty, D., Blumenthal, M.J., Heys, J.R., Landvatter, S.W., *et al.* A protein kinase involved in the regulation of inflammatory cytokine biosynthesis. Nature. 1994 Dec 22-29;372(6508):739-46.

Lee, S.J., Zhou, T., and Goldsmith, E.J. Crystallization of MAP kinases. Methods. 2006 Nov;40(3):224-33.

Leroux, A.E., and Biondi, R.M. Renaissance of Allostery to Disrupt Protein Kinase Interactions. Trends Biochem Sci. 2020 Jan;45(1):27-41.

Li, D., Shinagawa, K., Pang, L., Leung, T.K., Cardin, S., Wang, Z., and Nattel, S. Effects of angiotensin-converting enzyme inhibition on the development of the atrial fibrillation substrate in dogs with ventricular tachypacing-induced congestive heart failure. Circulation. 2001 Nov 20;104(21):2608-14.

Li, J., Miller, E.J., Ninomiya-Tsuji, J., Russell, R.R., 3rd, and Young, L.H. AMP-activated protein kinase activates p38 mitogen-activated protein kinase by increasing recruitment of p38 MAPK to TAB1 in the ischemic heart. Circ Res. 2005a Oct 28;97(9):872-9.

Li, M., Georgakopoulos, D., Lu, G., Hester, L., Kass, D.A., Hasday, J., and Wang, Y. p38 MAP kinase mediates inflammatory cytokine induction in cardiomyocytes and extracellular matrix remodeling in heart. Circulation. 2005b May 17;111(19):2494-502.

Li, X., Liu, M., Sun, R., Zeng, Y., Chen, S., and Zhang, P. Protective approaches against myocardial ischemia reperfusion injury. Exp Ther Med. 2016 Dec;12(6):3823-3829.

Liebschner, D., Afonine, P.V., Baker, M.L., Bunkoczi, G., Chen, V.B., Croll, T.I., Hintze, B., Hung, L.W., Jain, S., McCoy, A.J., *et al.* Macromolecular structure determination using X-rays, neutrons and electrons: recent developments in Phenix. Acta Crystallogr D Struct Biol. 2019 Oct 1;75(Pt 10):861-877.

Liu, X., Zhang, C.S., Lu, C., Lin, S.C., Wu, J.W., and Wang, Z.X. A conserved motif in JNK/p38-specific MAPK phosphatases as a determinant for JNK1 recognition and inactivation. Nat Commun. 2016 Mar 18;7:10879.

Livingstone, C., Patel, G., and Jones, N. ATF-2 contains a phosphorylation-dependent transcriptional activation domain. EMBO J. 1995 Apr 18;14(8):1785-97.

Lo, M.C., Aulabaugh, A., Jin, G., Cowling, R., Bard, J., Malamas, M., and Ellestad, G. Evaluation of fluorescence-based thermal shift assays for hit identification in drug discovery. Anal Biochem. 2004 Sep 1;332(1):153-9.

Lombard, C.K., Davis, A.L., Inukai, T., and Maly, D.J. Allosteric Modulation of JNK Docking Site Interactions with ATP-Competitive Inhibitors. Biochemistry. 2018 Oct 9;57(40):5897-5909.

Lopez-Garcia, L.A., Schulze, J.O., Frohner, W., Zhang, H., Suss, E., Weber, N., Navratil, J., Amon, S., Hindie, V., Zeuzem, S., *et al.* Allosteric regulation of protein kinase PKCzeta by the N-terminal C1 domain and small compounds to the PIF-pocket. Chem Biol. 2011 Nov 23;18(11):1463-73.

Lu, G., Kang, Y.J., Han, J., Herschman, H.R., Stefani, E., and Wang, Y. TAB-1 modulates intracellular localization of p38 MAP kinase and downstream signaling. J Biol Chem. 2006 Mar 3;281(9):6087-95.

Lu, H., Iuliano, J.N., and Tonge, P.J. Structure-kinetic relationships that control the residence time of drug-target complexes: insights from molecular structure and dynamics. Curr Opin Chem Biol. 2018 Jun;44:101-109.

Lu, H., and Tonge, P.J. Drug-target residence time: critical information for lead optimization. Curr Opin Chem Biol. 2010 Aug;14(4):467-74.

Ma, W., Wei, S., Zhang, B., and Li, W. Molecular Mechanisms of Cardiomyocyte Death in Drug-Induced Cardiotoxicity. Front Cell Dev Biol. 2020 Jun 3;8:434.

Maillet, A., Tan, K., Chai, X., Sadananda, S.N., Mehta, A., Ooi, J., Hayden, M.R., Pouladi, M.A., Ghosh, S., Shim, W., *et al.* Modeling Doxorubicin-Induced Cardiotoxicity in Human Pluripotent Stem Cell Derived-Cardiomyocytes. Sci Rep. 2016 May 4;6:25333.

Manning, G., Plowman, G.D., Hunter, T., and Sudarsanam, S. Evolution of protein kinase signaling from yeast to man. Trends Biochem Sci. 2002 Oct;27(10):514-20.

Martin, E.D., Bassi, R., and Marber, M.S. (2015). p38 MAPK in cardioprotection - are we there yet? Br J Pharmacol. 2015 Apr;172(8):2101-13.

Matesanz, N., Bernardo, E., Acin-Perez, R., Manieri, E., Perez-Sieira, S., Hernandez-Cosido, L., Montalvo-Romeral, V., Mora, A., Rodriguez, E., Leiva-Vega, L., *et al.* MKK6 controls T3-mediated browning of white adipose tissue. Nat Commun. 2017 Oct 11;8(1):856.

Meijles, D.N., Cull, J.J., Markou, T., Cooper, S.T.E., Haines, Z.H.R., Fuller, S.J., O'Gara, P., Sheppard, M.N., Harding, S.E., Sugden, P.H., *et al.* Redox Regulation of Cardiac ASK1 (Apoptosis Signal-Regulating Kinase 1) Controls p38-MAPK (Mitogen-Activated Protein Kinase) and Orchestrates Cardiac Remodeling to Hypertension. Hypertension. 2020 Oct;76(4):1208-1218.

Menick, D.R., Renaud, L., Buchholz, A., Muller, J.G., Zhou, H., Kappler, C.S., Kubalak, S.W., Conway, S.J., and Xu, L. Regulation of Ncx1 gene expression in the normal and hypertrophic heart. Ann N Y Acad Sci. 2007 Mar;1099:195-203.

Mishra, S., Guan, J., Plovie, E., Seldin, D.C., Connors, L.H., Merlini, G., Falk, R.H., MacRae, C.A., and Liao, R. Human amyloidogenic light chain proteins result in cardiac dysfunction, cell death, and early mortality in zebrafish. Am J Physiol Heart Circ Physiol. 2013 Jul 1;305(1):H95-103.

Mittelstadt, P.R., Yamaguchi, H., Appella, E., and Ashwell, J.D. T cell receptor-mediated activation of p38{alpha} by mono-phosphorylation of the activation loop results in altered substrate specificity. J Biol Chem. 2009 Jun 5;284(23):15469-74.

Moerke, N.J. Fluorescence Polarization (FP) Assays for Monitoring Peptide-Protein or Nucleic Acid-Protein Binding. Curr Protoc Chem Biol. 2009 Dec 1;1(1):1-15.

Molkentin, J.D., Bugg, D., Ghearing, N., Dorn, L.E., Kim, P., Sargent, M.A., Gunaje, J., Otsu, K., and Davis, J. Fibroblast-Specific Genetic Manipulation of p38 Mitogen-Activated Protein Kinase In Vivo Reveals Its Central Regulatory Role in Fibrosis. Circulation. 2017 Aug 8;136(6):549-561.

Mudgett, J.S., Ding, J., Guh-Siesel, L., Chartrain, N.A., Yang, L., Gopal, S., and Shen, M.M. Essential role for p38alpha mitogen-activated protein kinase in placental angiogenesis. Proc Natl Acad Sci U S A. 2000 Sep 12;97(19):10454-9.

Munoz, L., Ramsay, E.E., Manetsch, M., Ge, Q., Peifer, C., Laufer, S., and Ammit, A.J. Novel p38 MAPK inhibitor ML3403 has potent anti-inflammatory activity in airway smooth muscle. Eur J Pharmacol. 2010 Jun 10;635(1-3):212-8.

Murshudov, G.N., Skubak, P., Lebedev, A.A., Pannu, N.S., Steiner, R.A., Nicholls, R.A., Winn, M.D., Long, F., and Vagin, A.A. REFMAC5 for the refinement of macromolecular crystal structures. Acta Crystallogr D Biol Crystallogr. 2011 Apr;67(Pt 4):355-67.

Nichols, C., Ng, J., Keshu, A., Kelly, G., Conte, M.R., Marber, M.S., Fraternali, F., and De Nicola, G.F. Mining the PDB for Tractable Cases Where X-ray Crystallography Combined with Fragment Screens Can Be Used to Systematically Design Protein-Protein Inhibitors: Two Test Cases Illustrated by IL1beta-IL1R and p38alpha-TAB1 Complexes. J Med Chem. 2020 Jul 23;63(14):7559-7568.

Nielsen, G., and Schwalbe, H. NMR spectroscopic investigations of the activated p38alpha mitogen-activated protein kinase. Chembiochem. 2011 Nov 25;12(17):2599-607.

Nussinov, R., and Tsai, C.J. The different ways through which specificity works in orthosteric and allosteric drugs. Curr Pharm Des. 2012;18(9):1311-6.

Nussinov, R., Tsai, C.J., and Jang, H. Dynamic Protein Allosteric Regulation and Disease. Adv Exp Med Biol. 2019;1163:25-43.

Papalia, G.A., Giannetti, A.M., Arora, N., and Myszka, D.G. Thermodynamic characterization of pyrazole and azaindole derivatives binding to p38 mitogen-activated protein kinase using Biacore T100 technology and van't Hoff analysis. Anal Biochem. 2008 Dec 15;383(2):255-64.

Pargellis, C., Tong, L., Churchill, L., Cirillo, P.F., Gilmore, T., Graham, A.G., Grob, P.M., Hickey, E.R., Moss, N., Pav, S., *et al.* Inhibition of p38 MAP kinase by utilizing a novel allosteric binding site. Nat Struct Biol. 2002 Apr;9(4):268-72.

Pathak, S., Borodkin, V.S., Albarbarawi, O., Campbell, D.G., Ibrahim, A., and van Aalten, D.M. O-GlcNAcylation of TAB1 modulates TAK1-mediated cytokine release. EMBO J. 2012 Mar 21;31(6):1394-404.

Patnaik, A., Haluska, P., Tolcher, A.W., Erlichman, C., Papadopoulos, K.P., Lensing, J.L., Beeram, M., Molina, J.R., Rasco, D.W., Arcos, R.R., *et al.* A First-in-Human Phase I Study of the Oral p38 MAPK Inhibitor, Ralimetinib (LY2228820 Dimesylate), in Patients with Advanced Cancer. Clin Cancer Res. 2016 Mar 1;22(5):1095-102.

Pav, S., White, D.M., Rogers, S., Crane, K.M., Cywin, C.L., Davidson, W., Hopkins, J., Brown, M.L., Pargellis, C.A., and Tong, L. Crystallization and preliminary crystallographic analysis of recombinant human P38 MAP kinase. Protein Sci. 1997 Jan;6(1):242-5.

Peregrin, S., Jurado-Pueyo, M., Campos, P.M., Sanz-Moreno, V., Ruiz-Gomez, A., Crespo, P., Mayor, F., Jr., and Murga, C. Phosphorylation of p38 by GRK2 at the docking groove unveils a novel mechanism for inactivating p38MAPK. Curr Biol. 2006 Oct 24;16(20):2042-7.

Pervushin, K., Riek, R., Wider, G., and Wuthrich, K. Attenuated T2 relaxation by mutual cancellation of dipole-dipole coupling and chemical shift anisotropy indicates an avenue to NMR structures of very large biological macromolecules in solution. Proc Natl Acad Sci U S A. 1997 Nov 11;94(23):12366-71.

Pettersen, E.F., Goddard, T.D., Huang, C.C., Couch, G.S., Greenblatt, D.M., Meng, E.C., and Ferrin, T.E. UCSF Chimera--a visualization system for exploratory research and analysis. J Comput Chem. 2004 Oct;25(13):1605-12.

Pincus, D., Pandey, J.P., Feder, Z.A., Creixell, P., Resnekov, O., and Reynolds, K.A. Engineering allosteric regulation in protein kinases. Sci Signal. 2018 Nov 6;11(555):eaar3250.

Purser, S., Moore, P.R., Swallow, S., and Gouverneur, V. Fluorine in medicinal chemistry. Chem Soc Rev. 2008 Feb;37(2):320-30.

Raab, M., Sanhaji, M., Pietsch, L., Bequignon, I., Herbrand, A.K., Suss, E., Gande, S.L., Caspar, B., Kudlinzki, D., Saxena, K., *et al.* Modulation of the Allosteric Communication between the Polo-Box Domain and the Catalytic Domain in Plk1 by Small Compounds. ACS Chem Biol. 2018 Aug 17;13(8):1921-1931.

Richardson, L., Dixon, C.L., Aguilera-Aguirre, L., and Menon, R. Oxidative stress-induced TGF-beta/TAB1-mediated p38MAPK activation in human amnion epithelial cells. Biol Reprod. 2018 Nov 1;99(5):1100-1112.

Romero-Becerra, R., Santamans, A.M., Folgueira, C., and Sabio, G. p38 MAPK Pathway in the Heart: New Insights in Health and Disease. Int J Mol Sci. 2020 Oct 8;21(19):7412.

Roskoski, R., Jr. Classification of small molecule protein kinase inhibitors based upon the structures of their drug-enzyme complexes. Pharmacol Res. 2016 Jan;103:26-48.

Roskoski, R., Jr. Properties of FDA-approved small molecule protein kinase inhibitors. Pharmacol Res. 2019 Jun;144:19-50.

Roskoski, R., Jr. Properties of FDA-approved small molecule protein kinase inhibitors: A 2020 update. Pharmacol Res. 2020 Feb;152:104609.

Roux, P.P., and Blenis, J. ERK and p38 MAPK-activated protein kinases: a family of protein kinases with diverse biological functions. Microbiol Mol Biol Rev. 2004 Jun;68(2):320-44.

Ruan, Y., Dong, C., Patel, J., Duan, C., Wang, X., Wu, X., Cao, Y., Pu, L., Lu, D., Shen, T., *et al.* SIRT1 suppresses doxorubicin-induced cardiotoxicity by regulating the oxidative stress and p38MAPK pathways. Cell Physiol Biochem. 2015;35(3):1116-24.

Ruiz-Bonilla, V., Perdiguero, E., Gresh, L., Serrano, A.L., Zamora, M., Sousa-Victor, P., Jardi, M., Wagner, E.F., and Munoz-Canoves, P. Efficient adult skeletal muscle regeneration in mice deficient in p38beta, p38gamma and p38delta MAP kinases. Cell Cycle. 2008 Jul 15;7(14):2208-14.

Sakkinen, H., Aro, J., Kaikkonen, L., Ohukainen, P., Napankangas, J., Tokola, H., Ruskoaho, H., and Rysa, J. Mitogen-activated protein kinase p38 target regenerating islet-derived 3gamma expression is upregulated in cardiac inflammatory response in the rat heart. Physiol Rep. 2016 Oct;4(20):e12996.

Salameh, A., Krautblatter, S., Baessler, S., Karl, S., Rojas Gomez, D., Dhein, S., and Pfeiffer, D. Signal transduction and transcriptional control of cardiac connexin43 up-regulation after alpha 1-adrenoceptor stimulation. J Pharmacol Exp Ther. 2008 Jul;326(1):315-22.

Salvador, J.M., Mittelstadt, P.R., Belova, G.I., Fornace, A.J., Jr., and Ashwell, J.D. The autoimmune suppressor Gadd45alpha inhibits the T cell alternative p38 activation pathway. Nat Immunol. 2005b Apr;6(4):396-402.

Salvador, J.M., Mittelstadt, P.R., Guszczynski, T., Copeland, T.D., Yamaguchi, H., Appella, E., Fornace, A.J., Jr., and Ashwell, J.D. Alternative p38 activation pathway mediated by T cell receptor-proximal tyrosine kinases. Nat Immunol. 2005b Apr;6(4):390-5.

Saurin, A.T., Martin, J.L., Heads, R.J., Foley, C., Mockridge, J.W., Wright, M.J., Wang, Y., and Marber, M.S. The role of differential activation of p38-mitogen-activated protein kinase in preconditioned ventricular myocytes. FASEB J. 2000 Nov;14(14):2237-46.

Scharf, M., Neef, S., Freund, R., Geers-Knorr, C., Franz-Wachtel, M., Brandis, A., Krone, D., Schneider, H., Groos, S., Menon, M.B., *et al.* Mitogen-activated protein kinase-activated protein kinases 2 and 3 regulate SERCA2a expression and fiber type composition to modulate skeletal muscle and cardiomyocyte function. Mol Cell Biol. 2013 Jul;33(13):2586-602.

Schulze, J.O., Saladino, G., Busschots, K., Neimanis, S., Suss, E., Odadzic, D., Zeuzem, S., Hindie, V., Herbrand, A.K., Lisa, M.N., *et al.* Bidirectional Allosteric Communication between the ATP-Binding Site and the Regulatory PIF Pocket in PDK1 Protein Kinase. Cell Chem Biol. 2016 Oct 20;23(10):1193-1205.

Segura, A.M., Frazier, O.H., and Buja, L.M. Fibrosis and heart failure. Heart Fail Rev. 2014 Mar;19(2):173-85.

Selness, S.R., Devraj, R.V., Devadas, B., Walker, J.K., Boehm, T.L., Durley, R.C., Shieh, H., Xing, L., Rucker, P.V., Jerome, K.D., *et al.* Discovery of PH-797804, a highly selective and potent inhibitor of

p38 MAP kinase. Bioorg Med Chem Lett. 2011 Jul 1;21(13):4066-71.

Shah, N.G., Tulapurkar, M.E., Ramarathnam, A., Brophy, A., Martinez, R., 3rd, Hom, K., Hodges, T., Samadani, R., Singh, I.S., MacKerell, A.D., Jr., *et al.* Novel Noncatalytic Substrate-Selective p38alpha-Specific MAPK Inhibitors with Endothelial-Stabilizing and Anti-Inflammatory Activity. J Immunol. 2017 Apr 15;198(8):3296-3306.

Shah, P., and Westwell, A.D. The role of fluorine in medicinal chemistry. J Enzyme Inhib Med Chem. 2007 Oct;22(5):527-40.

Shi, J., Guan, J., Jiang, B., Brenner, D.A., Del Monte, F., Ward, J.E., Connors, L.H., Sawyer, D.B., Semigran, M.J., Macgillivray, T.E., *et al.* Amyloidogenic light chains induce cardiomyocyte contractile dysfunction and apoptosis via a non-canonical p38alpha MAPK pathway. Proc Natl Acad Sci U S A. 2010 Mar 2;107(9):4188-93.

Shibuya, H., Yamaguchi, K., Shirakabe, K., Tonegawa, A., Gotoh, Y., Ueno, N., Irie, K., Nishida, E., and Matsumoto, K. TAB1: an activator of the TAK1 MAPKKK in TGF-beta signal transduction. Science. 1996 May 24;272(5265):1179-82.

Song, N., Ma, J., Meng, X.W., Liu, H., Wang, H., Song, S.Y., Chen, Q.C., Liu, H.Y., Zhang, J., Peng, K., *et al.* Heat Shock Protein 70 Protects the Heart from Ischemia/Reperfusion Injury through Inhibition of p38 MAPK Signaling. Oxid Med Cell Longev. 2020 Apr 7;2020:3908641.

Sudo, T., Yagasaki, Y., Hama, H., Watanabe, N., and Osada, H. Exip, a new alternative splicing variant of p38 alpha, can induce an earlier onset of apoptosis in HeLa cells. Biochem Biophys Res Commun. 2002 Mar 8;291(4):838-43.

Surinkaew, S., Kumphune, S., Chattipakorn, S., and Chattipakorn, N. Inhibition of p38 MAPK during ischemia, but not reperfusion, effectively attenuates fatal arrhythmia in ischemia/reperfusion heart. J Cardiovasc Pharmacol. 2013 Feb;61(2):133-41.

Tanno, M., Bassi, R., Gorog, D.A., Saurin, A.T., Jiang, J., Heads, R.J., Martin, J.L., Davis, R.J., Flavell, R.A., and Marber, M.S. Diverse mechanisms of myocardial p38 mitogen-activated protein kinase activation: evidence for MKK-independent activation by a TAB1-associated mechanism contributing to injury during myocardial ischemia. Circ Res. 2003 Aug 8;93(3):254-61.

Tanoue, T., Adachi, M., Moriguchi, T., and Nishida, E. A conserved docking motif in MAP kinases common to substrates, activators and regulators. Nat Cell Biol. 2000 Feb;2(2):110-6.

Tanoue, T., and Nishida, E. Docking interactions in the mitogen-activated protein kinase cascades. Pharmacol Ther. 2002 Feb-Mar;93(2-3):193-202.

Taylor, S.S., Keshwani, M.M., Steichen, J.M., and Kornev, A.P. Evolution of the eukaryotic protein kinases as dynamic molecular switches. Philos Trans R Soc Lond B Biol Sci. 2012 Sep 19;367(1602):2517-28.

Taylor, S.S., and Kornev, A.P. Protein kinases: evolution of dynamic regulatory proteins. Trends Biochem Sci. 2011 Feb;36(2):65-77.

Thapa, D., Nichols, C., Bassi, R., Martin, E.D., Verma, S., Conte, M.R., De Santis, V., De Nicola, G.F., and Marber, M.S. TAB1-Induced Autoactivation of p38alpha Mitogen-Activated Protein Kinase Is Crucially Dependent on Threonine 185. Mol Cell Biol. 2018 Feb 12;38(5):e00409-17.

Theivanthiran, B., Kathania, M., Zeng, M., Anguiano, E., Basrur, V., Vandergriff, T., Pascual, V., Wei, W.Z., Massoumi, R., and Venuprasad, K. The E3 ubiquitin ligase Itch inhibits p38alpha signaling and skin inflammation through the ubiquitylation of Tab1. Sci Signal. 2015 Feb 24;8(365):ra22.

Thurmond, R.L., Wadsworth, S.A., Schafer, P.H., Zivin, R.A., and Siekierka, J.J. Kinetics of small molecule inhibitor binding to p38 kinase. Eur J Biochem. 2001 Nov;268(22):5747-54.

Tibaut, M., Mekis, D., and Petrovic, D. Pathophysiology of Myocardial Infarction and Acute Management Strategies. Cardiovasc Hematol Agents Med Chem. 2017;14(3):150-159.

Tonge, P.J. Drug-Target Kinetics in Drug Discovery. ACS Chem Neurosci. 2018 Jan 17;9(1):29-39.

Trempolec, N., Dave-Coll, N., and Nebreda, A.R. SnapShot: p38 MAPK substrates. Cell. 2013 Feb 14;152(4):924-924.e1.

Turnbull, W.B., and Daranas, A.H. On the value of c: can low affinity systems be studied by isothermal titration calorimetry? J Am Chem Soc. 2003 Dec 3;125(48):14859-66.

Vahebi, S., Ota, A., Li, M., Warren, C.M., de Tombe, P.P., Wang, Y., and Solaro, R.J. p38-MAPK induced dephosphorylation of alpha-tropomyosin is associated with depression of myocardial sarcomeric tension and ATPase activity. Circ Res. 2007 Feb 16;100(3):408-15.

Vasta, J.D., Corona, C.R., Wilkinson, J., Zimprich, C.A., Hartnett, J.R., Ingold, M.R., Zimmerman, K., Machleidt, T., Kirkland, T.A., Huwiler, K.G., *et al.* Quantitative, Wide-Spectrum Kinase Profiling in Live Cells for Assessing the Effect of Cellular ATP on Target Engagement. Cell Chem Biol. 2018 Feb 15;25(2):206-214.e11.

Vergote, I., Heitz, F., Buderath, P., Powell, M., Sehouli, J., Lee, C.M., Hamilton, A., Fiorica, J., Moore, K.N., Teneriello, M., *et al.* A randomized, double-blind, placebo-controlled phase 1b/2 study of ralimetinib, a p38 MAPK inhibitor, plus gemcitabine and carboplatin versus gemcitabine and carboplatin for women with recurrent platinum-sensitive ovarian cancer. Gynecol Oncol. 2020 Jan;156(1):23-31.

Vogtherr, M., Saxena, K., Hoelder, S., Grimme, S., Betz, M., Schieborr, U., Pescatore, B., Robin, M., Delarbre, L., Langer, T., *et al.* NMR characterization of kinase p38 dynamics in free and ligand-bound forms. Angew Chem Int Ed Engl. 2006 Jan 30;45(6):993-7.

Vonrhein, C., Flensburg, C., Keller, P., Sharff, A., Smart, O., Paciorek, W., Womack, T., and Bricogne, G. Data processing and analysis with the autoPROC toolbox. Acta Crystallogr D Biol Crystallogr. 2011 Apr;67(Pt 4):293-302.

Walsh, C.T., Garneau-Tsodikova, S., and Gatto, G.J., Jr. Protein posttranslational modifications: the chemistry of proteome diversifications. Chem Int Ed Engl. 2005 Dec 1;44(45):7342-72.

Wang, C.Y., Liu, H.J., Chen, H.J., Lin, Y.C., Wang, H.H., Hung, T.C., and Yeh, H.I. AGE-BSA down-regulates endothelial connexin43 gap junctions. BMC Cell Biol. 2011 May 16;12:19.

Wang, L., Perera, B.G., Hari, S.B., Bhhatarai, B., Backes, B.J., Seeliger, M.A., Schurer, S.C., Oakes, S.A., Papa, F.R., and Maly, D.J. Divergent allosteric control of the IRE1alpha endoribonuclease using kinase inhibitors. Nat Chem Biol. 2012 Dec;8(12):982-9.

Wang, M., Li, Z., Zhang, X., Xie, X., Zhang, Y., Wang, X., and Hou, Y. Rosuvastatin attenuates atrial structural remodelling in rats with myocardial infarction through the inhibition of the p38 MAPK signalling pathway. Heart Lung Circ. 2015 Apr;24(4):386-94.

Wang, Q., Feng, J., Wang, J., Zhang, X., Zhang, D., Zhu, T., Wang, W., Wang, X., Jin, J., Cao, J., *et al.* Disruption of TAB1/p38alpha interaction using a cell-permeable peptide limits myocardial ischemia/reperfusion injury. Mol Ther. 2013 Sep;21(9):1668-77.

Wang, X., Veeraraghavan, J., Liu, C.C., Cao, X., Qin, L., Kim, J.A., Tan, Y., Loo, S.K., Hu, Y., Lin, L., *et al.* Therapeutic Targeting of Nemo-like Kinase in Primary and Acquired Endocrine-resistant Breast Cancer. Clin Cancer Res. 2021 May 1;27(9):2648-2662.

Wang, Z., Canagarajah, B.J., Boehm, J.C., Kassisa, S., Cobb, M.H., Young, P.R., Abdel-Meguid, S., Adams, J.L., and Goldsmith, E.J. Structural basis of inhibitor selectivity in MAP kinases. Structure. 1998 Sep 15;6(9):1117-28.

Weston, C.R., Lambright, D.G., and Davis, R.J. Signal transduction. MAP kinase signaling specificity. Science. 2002 Jun 28;296(5577):2345-7.

Widmann, C., Gibson, S., Jarpe, M.B., and Johnson, G.L. Mitogen-activated protein kinase: conservation of a three-kinase module from yeast to human. Physiol Rev. 1999 Jan;79(1):143-80.

Wilson, B.A., Alam, M.S., Guszczynski, T., Jakob, M., Shenoy, S.R., Mitchell, C.A., Goncharova, E.I., Evans, J.R., Wipf, P., Liu, G., *et al.* Discovery and Characterization of a Biologically Active Non-ATP-Com-

petitive p38 MAP Kinase Inhibitor. J Biomol Screen. 2016 Mar;21(3):277-89.

Willemsen-Seegers, N., Uitdehaag, J.C.M., Prinsen, M.B.W., de Vetter, J.R.F., de Man, J., Sawa, M., Kawase, Y., Buijsman, R.C., and Zaman, G.J.R. Compound Selectivity and Target Residence Time of Kinase Inhibitors Studied with Surface Plasmon Resonance. J Mol Biol. 2017 Feb 17;429(4):574-586.

Winn, M.D., Ballard, C.C., Cowtan, K.D., Dodson, E.J., Emsley, P., Evans, P.R., Keegan, R.M., Krissinel, E.B., Leslie, A.G., McCoy, A., *et al.* Overview of the CCP4 suite and current developments. Acta Crystallogr D Biol Crystallogr. 2011 Apr;67(Pt 4):235-42.

Witek, P., Korga, A., Burdan, F., Ostrowska, M., Nosowska, B., Iwan, M., and Dudka, J. (2016). The effect of a number of H9C2 rat cardiomyocytes passage on repeatability of cytotoxicity study results. Cytotechnology. 2016 Dec;68(6):2407-2415.

Wold, L.E., Aberle, N.S., 2nd, and Ren, J. (2005). Doxorubicin induces cardiomyocyte dysfunction via a p38 MAP kinase-dependent oxidative stress mechanism. Cancer Detect Prev. 2005;29(3):294-9.

Wolf, A., Beuerlein, K., Eckart, C., Weiser, H., Dickkopf, B., Muller, H., Sakurai, H., and Kracht, M. Identification and functional characterization of novel phosphorylation sites in TAK1-binding protein (TAB) 1. PLoS One. 2011;6(12):e29256.

Wu, P., Clausen, M.H., and Nielsen, T.E. Allosteric small-molecule kinase inhibitors. Pharmacol Ther. 2015 Dec;156:59-68.

Yagasaki, Y., Sudo, T., and Osada, H. Exip, a splicing variant of p38alpha, participates in interleukin-1 receptor proximal complex and downregulates NF-kappaB pathway. FEBS Lett. 2004 Sep 24;575(1-3):136-40.

Yang, X., Yang, J., Hu, J., Li, X., Zhang, X., and Li, Z. Apigenin attenuates myocardial ischemia/reperfusion injury via the inactivation of p38 mitogenactivated protein kinase. Mol Med Rep. 2015 Nov;12(5):6873-8.

Yao, J., Ke, J., Zhou, Z., Tan, G., Yin, Y., Liu, M., Chen, J., and Wu, W. Combination of HGF and IGF-1 promotes connexin 43 expression and improves ventricular arrhythmia after myocardial infarction through activating the MAPK/ERK and MAPK/p38 signaling pathways in a rat model. Cardiovasc Diagn Ther. 2019 Aug;9(4):346-354.

Yokota, T., and Wang, Y. p38 MAP kinases in the heart. Gene. 2016 Jan 10;575(2 Pt 2):369-376.

Young, P.R., McLaughlin, M.M., Kumar, S., Kassis, S., Doyle, M.L., McNulty, D., Gallagher, T.F., Fisher, S., McDonnell, P.C., Carr, S.A., *et al.* Pyridinyl imidazole inhibitors of p38 mitogen-activated protein kinase bind in the ATP site. J Biol Chem. 1997 May 2;272(18):12116-21.

Zhang, S., Liu, X., Bawa-Khalfe, T., Lu, L.S., Lyu, Y.L., Liu, L.F., and Yeh, E.T. Identification of the molecular basis of doxorubicin-induced cardiotoxicity. Nat Med. 2012 Nov;18(11):1639-42.

Zhang, W., and Liu, H.T. MAPK signal pathways in the regulation of cell proliferation in mammalian cells. Cell Res. 2002 Mar;12(1):9-18.

Zhou, H., Zheng, M., Chen, J., Xie, C., Kolatkar, A.R., Zarubin, T., Ye, Z., Akella, R., Lin, S., Goldsmith, E.J., *et al.* Determinants that control the specific interactions between TAB1 and p38alpha. Mol Cell Biol. 2006 May;26(10):3824-34.

Zhu, D., Xing, Q., Cao, R., Zhao, D., and Zhong, W. Synthesis and p38 Inhibitory Activity of Some Novel Substituted N,N'-Diarylurea Derivatives. Molecules. 2016 May 23;21(5):677.

Zhu, S., Xu, T., Luo, Y., Zhang, Y., Xuan, H., Ma, Y., Pan, D., Li, D., and Zhu, H. Luteolin Enhances Sarcoplasmic Reticulum Ca2+-ATPase Activity through p38 MAPK Signaling thus Improving Rat Cardiac Function after Ischemia/Reperfusion. Cell Physiol Biochem. 2017;41(3):999-1010.